Fluid Structure Interaction and Hemodynamic Analysis of the Aortic Valve

Soroush Nobari

Department of Biomedical Engineering
McGill University

Montréal, Québec, Canada

April 2012

A thesis submitted to McGill University in partial fulfillment of the requirements for the degree of Doctor of Philosophy in Biomedical Engineering.

Abstract

Cardiovascular pathologies specifically valvular heart diseases remain the biggest cause of deaths worldwide with a mortality rate of 4% in industrialized countries and up to 42% in developing countries. Aortic valve and coronary arteries have in particular been the focus of many studies during the recent years. This is due to the prevalence of pathologies in these regions and the subsequent critical consequences. In certain pathological conditions such as aortic sclerosis, the micro-structure of the aortic root and the aortic valve leaflets are altered in response to stress resulting in changes in tissue thickness, stiffness or both. Such pathologies are thought to affect coronary blood flow which could be life threatening.

Numerical studies have greatly assisted in understanding the biomechanics of the aortic valve, its function as well as the impact of pathologies on cardiac tissue mechanics and local hemodynamic. The interaction between the blood and the cardiac tissue is critical in properly studying the response of the system to its physiological conditions. However, due to the inherent complexity of fluid-structure interaction modeling of aortic leaflets, there is a clear lack of a global representation of the aortic valve region which would aid in understanding the overall behaviour of this structure in pathological conditions. Recently, there have been clinical investigations that have observed simultaneous structural and hemodynamic variations in the aortic valve and coronary arteries due to regional pathologies.

The main objective of this work is to elucidate this observed and yet unexplained phenomenon where, a regional pathology could lead to global variations in the structure and hemodynamic of the aortic valve region as well as in the coronary arteries. Therefore this thesis concentrates on three aspects: physiological heart valve modeling, investigating coronary hemodynamic variables in presence of valvular pathologies, and the possible impact of coronary stenosis on valvular dynamics. This model can aid in explaining the underlying behaviour that leads to the observed inter-relation between the aortic valve and coronary flow. Moreover, within the clinical practice our model has the potential to serve as a possible diagnostic tool; as the cardiac surgeons and interventional cardiologists can benefit from the additional input provided by this model for choosing the time of surgical intervention in the diseased aortic valve region.

Résumé

Les pathologies cardiovasculaires, en particulier les maladies des valves cardiaques, restent toujours les causes prédominantes de mortalité, à un taux de 4% dans les pays développés et à 42% dans les pays en développement. La valve aortique et les artères coronariennes sont l'emphase de nombreux articles récents. Cela est surtout attribuable à l'occurrence élevée de ses maladies dans ces régions et les conséquences critiques qui suivent. Avec certaines pathologies cardiovasculaires, comme la sclérose aortique, les microstructures de la racine et des feuillets aortiques peuvent être modifié avec des contraintes résultantes des changements de l'épaisseur ou de l'élasticité du tissu, ou des deux. Ces pathologies sont reliées à l'altération du débit sanguin, ce qui peut être mortel.

Des études numériques ont assisté considérablement à la compréhension des biomécaniques de la fonctionnalité et des pathologies des feuillets, leur effet sur les tissus cardiaques et l'hémodynamie locale. Par contre, ces investigations ont plutôt analysé la structure des valves que les interactions entre le sang et le tissu cardiaque. Ce facteur simple mais sophistiqué est critique pour suffisamment étudier la réponse du système face aux conditions physiologiques. Par ailleurs, à cause de la complexité inhérente de l'analyse d'interaction fluide-structure des feuillets aortiques, il y a un manque évident d'une représentation globale de la région des valves aortiques, ce qui pourrait avancer la connaissance du comportement global de cette structure sous les conditions physiologiques.

L'objectif primaire de cette thèse est d'expliquer ce phénomène inconnu dans lequel une pathologie régionale conduit à des variations globales structurelles et hémodynamiques au niveau de la région aortique ainsi que sur les artères coronaires. Ces dernières ont été ajoutées dans le modèle global pour explorer la possibilité d'une interrelation entre ces structures et la valve aortique. Par conséquent, cette thèse est concernée par trois aspects en particulier : la modélisation physiologique de la valve cardiaque, l'investigation des variables hémodynamiques des coronaires par rapport aux pathologies valvulaire, et l'impact possible d'une sténose coronarienne sur la dynamique valvulaire. Ce modèle peut aider à explorer et confirmer le comportement de base de l'interaction entre la valve aortique et le débit coronarien. En plus, au point de vue de la pratique clinique, notre modèle a le potentiel d'être un outil diagnostique ; considérant que les chirurgiens cardiaques et les cardiologues interventionnels pourraient profiter des données additionnelles fournies par ce modèle pour mieux planifier le moment idéal pour l'intervention chirurgicale dans la région de la valve aortique pathologique.

Acknowledgments

I would like to thank my supervisors, Professor Rosaire Mongrain and Dr. Raymond Cartier, for their constant guidance, generous support and the independence provided to me during the course of the research involved in this thesis. This project would have never been accomplished without their trust and invaluable advices.

I would also like to thank my advisory committee members, Professor Richard Leask and Professor Satya Prakash for their useful insight and suggestions during the Ph.D. meetings. I would like to acknowledge the financial support from: Fonds québécois de la recherche sur la nature et les technologies fellowship, Natural Sciences and Engineering Research Council of Canada, Jeannette and Abram Victor Fellowship, Alma Mater and GREAT Student Travel Grant Award, and Biomedical department Principal Graduate Fellowship.

I am eternally grateful for the constant support and patience of my fiancée Isabelle throughout my doctoral degree and for being the most wonderful partner. I would also like to show my deepest gratitude to my loving parents Mostafa and Mahin for their incredible support, endless love and patience throughout my life and always believing in me despite the circumstances.

I was very fortunate to have worked within a research group composed of highly motivated, exceptional members. I would like to thank my friends and colleagues: Sacheen Bekah, Boby Chu, Juan Mejia, Ramsés Galaz Mendez, Ephrem Beaino, Reza Rabiei, Ali Ghoreishi and Marjan Molavi Zarandi for their unsparing collaboration and invaluable input throughout these years. I would especially like to thank Steven Reiter for the numerous discussions, his constant support and his encouragements that helped me at critical steps of my project. Administrative and technical support from staff in Mechanical and Biomedical Engineering offices and Montreal Heart Institute, especially from Pina Sorrini, Lina Vuch, Nancy Abate, Irene Cartier, Joyce Nault, Barbara Lapointe, Mary Fiorilli, Kevin Mitchell, François DiQuinzio, Gary Savard, and Michele Plante is greatly appreciated.

Contributions of the author

Journal Articles

S. Nobari, R. Mongrain, E. Gaillard, R. Leask, and R. Cartier, "Therapeutic Vascular Compliance Change May Cause Significant Variation in Coronary Perfusion: A Numerical Study," Computational and Mathematical Methods in Medicine, vol. 2012, Article ID 791686, 10 pages, 2012. doi:10.1155/2012/791686.

S. Nobari, R. Mongrain, R. Leask, R. Cartier. "Computation of regional hemodynamic variables using a global model of the aortic root", Submitted.

J. Trapeaux, D. Busseuil, Y. Shi, **S. Nobari**, D. Shustik, M. Mecteau, F. Poulin, M. Lebel, R. Mongrain, E. Rhéaume, J-C. Tardif. "ApoA-I mimetic peptide therapy improves aortic valve stenosis in $ApoE^{-/-}$ and $Wrn^{\Delta hel/\Delta hel}$ mice", Submitted.

Refereed Conference Papers

S. Nobari, R. Mongrain, R. Leask, R. Cartier. "Assessment of the Effect of Coronary Occlusion On Aortic Valve Dynamics Using A Global 3D FSI Model". ASME Summer Bioengineering Conference 2012, Fajardo, PR.

D. Busseuil, J. Trappeaux, Y. Shi, **S. Nobari**, D.Shustik, M. Mecteau, M. Lebel, R. Mongrain, E. Rheaume, J-C. Tardif, ÀpoA-I mimetic peptide infusion improve aortic valve stenosis in ApoE-/- and Wrn delta hel/delta hel mice". Europian Society of Cardiology 2012, Munich, Germany.

S. Nobari, R. Mongrain, R. Leask, R. Cartier. "Velocity Distribution Along the Coronary Arteries in a 3D Fluid Structure Interaction Model of the Aortic Valve". International Society of Biomechanics 2011, Brussels, Belgium.

S. Nobari, R. Mongrain, R. Leask, R. Cartier. "Effect of Aortic Distensibility on Coronary Flow: A 3D FSI Model of Aortic Valve With the Inclusion of Coronary Arteries ". ASME Summer Bioengineering Conference 2011, Farmington, PA.

S. Nobari, R. Mongrain, R. Leask, R. Cartier. "Development of a 3D FSI Model of the Aortic Root Incorporating the Coronary Structure". ASME Summer Bioengineering Conference 2010, Naples, FL.

S. Nobari, R. Mongrain, R. Leask, R. Cartier. "A 3D FSI Model of the Aortic Valve Including the Coronary Structure – Impact of Ostia Position on Coronary Flow". Canadian Cardiovascular Congress 2010, Montreal, QC.

S. Nobari, R. Mongrain, R. Leask, R. Cartier. "Incorporating Coronary Structures in a 3D Model of the Aortic Root - Effect of Valvular Pathologies on Coronary Flow". Interdisciplinary Graduate Student Research Symposium 2010, Montreal, QC.

S. Nobari, R. Mongrain, I. Campbel, R. Leask, R. Cartier. "Derivation of Surrogate Variables To Assess Pathological Conditions Using A 3D Model Of The Aortic Valve". ASME Summer Bioengineering Conference 2009, Lake Tahoe, CA.

S. Nobari, R. Mongrain, R. Leask, R. Cartier. "Implementing Engineering Metrics to Assess Pathologies of the Aortic Valve Region – a Numerical Study". Interdisciplinary Graduate Student Research Symposium 2009, Montreal, QC.

Rationale

We realize that there is a lack of a global representation of the aortic valve region which would aid in a better understanding of the overall behaviour of this structure due to pathological conditions. Recently, there have been clinical investigations that have observed simultaneous structural and hemodynamic variations in the aortic valve and coronary arteries due to regional pathologies. Where these clinical studies fall short is the explanation of the observed behaviour.

Hypothesis

Our hypothesis is that mechanical properties of the aortic valve (i.e. elastic modulus and tissue thickness) are the main source behind this observed hemodynamic variation and play an important role in the perfusion of blood into the coronary arteries, during diastole.

Objectives

The main objective of this thesis is then to bring an understanding to this unexplained phenomenon where, a regional pathology could lead to global variations in the structure and hemodynamic of the aortic valve region as well as the coronary arteries. Biomechanical representation of the aortic valve can assist in explaining the underlying interactions leading to such global variations. Ultimately, within the clinical practice such a model has the potential to serve as a possible diagnostic and surgical planning tool; as the cardiac surgeons and interventional cardiologists can benefit from the additional input provided by this model for choosing the time of surgical intervention in the diseased aortic valve region. Therefore in order to address our hypothesis, several objectives were defined:

- Creating a global and biomechanical model of the aortic valve with the inclusion of the coronary arteries.
- Investigating the impact of aortic pathologies such as aortic sclerosis on flow, velocity and shear stress distribution in coronary arteries.
- Investigating the mutual impact that coronary pathologies might have on valvular dynamics by introducing a stenosis in the coronary structure.
- Relating clinical indices which are accessible to the clinicians to biomechanical variables extracted from our results such as flow and stress

Table of contents

Abstract i

Résumé ii

Acknowledgments iii

Contributions of the author iv

Chapter 1 : Introduction 1

1.1 Clinical background 1

1.1.1 The heart and the circulatory system 1

1.1.2 Aortic valve 4

1.1.2.a Morphology of the aortic valve 4

1.1.2.b Function of the aortic valve 7

1.1.2.c Pathologies of the aortic valve 9

1.1.2.d Treatment of the aortic valve 11

1.1.3 Coronary arteries 16

1.1.3.a Physiology of coronary arteries 16

1.1.3.b Pathologies of the coronary arteries 17

1.1.3.c Coronary artery disease diagnosis 19

1.1.3.d Coronary artery disease treatment 21

1.2 Engineering background 23

1.2.1 Numerical methods 23

1.2.1.a Implicit solution method 25

1.2.1.b Explicit solution method 26

1.2.2 Fluid structure interaction 27

1.2.3 Various fluid-structure interaction methods 29

1.2.4 Arbitrary Lagrangian-Eulerian method 31

1.2.5 Overview of LS-DYNA 34
1.2.5.a Hydrocode modeling 35
1.2.5.b The operator split formulation 35
1.2.5.c Lagrangian-Eulerian coupling 37
1.2.6 A brief history of aortic valve simulations 39
Chapter 2 : Computational model 45
2.1 The normal aortic model 45
2.1.1 The geometry 45
2.1.2 Finite element model 48
2.1.2.a The structural/Lagrangian domain 48
2.1.2.b The Fluid/ALE domain 49
2.2 Global model of the aortic valve: Addition of coronary artery structures 51
2.2.1 Coronary artery geometry 52
2.2.2 Finite element model 53
2.2.2.a The structural/Lagrangian domain 53
2.2.2.b The Fluid/ALE domain 53
2.2.2.b.1 An overview of TrueGrid 56
2.2.2.b.2 Eulerian mesh creation using TrueGrid 58
2.3 Pathological global model of the aortic valve: Inclusion of coronary stenosis 67
2.4 Material property models 70
2.4.1 Vasculature material models 70
2.4.2 Blood material model 71
2.4.3 Boundary conditions 72
2.4.3.a The structural domain 72
2.4.3.b The fluid domain 73

Chapter 3 : Results of the aortic valve simulations 77
3.1 The normal base model of the aortic valve 77
3.1.1 The solid medium 77
3.1.1.a Leaflet morphologies and dynamics 77
3.1.1.b Leaflet stresses 80
3.1.2 The fluid medium 82
3.2 Global model of the aortic valve 89
3.2.1 The solid domain 89
3.2.2 Fluid domain 95
3.3 Pathological global model 103
Chapter 4 : Discussion and conclusion 107
4.1 Original outcomes 107
4.2 Discussion 108
4.3 Conclusion 113
4.4 Limitations and future work 113

List of Figures

Figure 1.1: The circulatory system in human body [adapted from Baileybio (downloaded Jan 2012)]. 2
Figure 1.2: Schematic representation of heart anatomy including its chambers and valves [adapted from CHOP (downloaded Jan 2012)]. 3
Figure 1.3: The heart valves viewed from above. The atria are removed to expose the mitral and tricuspid valves [adapted from Arthurs clip arts (downloaded Jan 2012)]. 3
Figure 1.4: (a) Schematic drawing of the aortic valve and its components and (b) longitudinal cross section of the left ventricle exposing the aortic valve, ascending aorta and left atrium [2]. . 5
Figure 1.5: Different structural layers of aortic cusps including fibrosa, spongiosa, ventricularis. [adapted from cardiothoracic surgery of USC (downloaded January 2012)]. 5
Figure 1.6: Top view of open and closed positions of aortic valve 6
Figure 1.7: Heart valves during (a) systole and (b) diastole [by F. Netter from CICMD (downloaded Jan 2012)], and the diagram of one cardiac cycle [by Destiny Qx from Wikipedia (downloaded Jan 2012)]. 8
Figure 1.8: Severely stenotic (a) tricuspid and (b) bicuspid aortic valve [by Peter Anderson from Wikipedia (downloaded Jan 2012)]. 9
Figure 1.9: (a) Schematic drawing and (b) Doppler image of blood leakage into the left ventricle due to aortic regurgitation [adapted from heart valve surgery (downloaded Jan 2012)]. Image (c) shows a severe aortic insufficiency causing a permanent opening of the leaflets [from Kadiol (downloaded Jan 2012)]. 11
Figure 1.10: (a) Ball and cage, (b) mono tilting [by Mirko Junge, downloaded Jan 2012), and (c) double tilting mechanical valve [adapted from gknmhospital (downloaded Jan2012)], and (d) a bio-prosthetic aortic valve. Implantation of (e) a bio-prosthetic valve versus (f) a mechanical valve [14]. 12
Figure 1.11: Comparison between Bentall, remodeling and re-implantation techniques [17]. 14
Figure 1.12: Step by step demonstration of the re-implantation (David's) procedure [18]. 15
Figure 1.13: (a) Incisions cut into the Dacron graft to accommodate for the remodeling surgery and (b) an example of the finished procedure [19]. 16
Figure 1.14: Anterior view of the coronary arteries and their downstream branching. [from medical atlas (downloaded Feb 2012)]. 17

Figure 1.15: (a) Initiation, progression, and complication of human coronary atherosclerotic plaque [26] (b) and its effect on blood flow [from OMNImedicalcenter, (downloaded 2012)]. Image (c) represents a typical eccentric atherosclerotic plaque [from brownmed [downloaded Feb 2012)]. 18
Figure 1.16: Sample images of (a) angiography, (b) CTA (from bocardiology), (c) MRA [28], (d) IVUS [29], and (e) echocardiography procedure [30]. 20
Figure 1.17: Schematic drawing of (a) a coronary bypass graft and (b) balloon angioplasty (PTCA) [by N. Paraskevas (downloaded Feb 2012)]. (c) Angiography images of before and after stent deployment in proximal RCA[35]. 22
Figure 1.18: A schematic drawing of (a) a sample FSI mesh and how (b) ALE method and (c) a non-conforming method deal with the structural deformation. 30
Figure 1.19: Schematic drawing representing the deformation and translation of Lagrangian vs Eulerian vs ALE meshes. 36
Figure 1.20: A drawing representing the penalty base coupling between Lagrangian and ALE material 38
Figure 2.1: Parametric representation of the aortic valve model 46
Figure 2.2: (a) axial, and (b) side view of the aortic valve model 47
Figure 2.3: Side view of aortic valve CAD models representing different heights of ostia location due to possible congenital disease or surgical procedures 47
Figure 2.4: Different views of the final structural mesh from (a) top view, (b) cut view, and (c) exploded view. 48
Figure 2.5: (a) an exploded view of the fluid domain, and (b) the final FSI model the aortic valve showing the submerged structural domain in the fluid domain 50
Figure 2.6: Geometric model of the (a) left and (b) right coronary arteries 52
Figure 2.7: (a) side, (b) top, and (c) isometric view of the CAD representation of the aortic valve model including the coronary structures. 52
Figure 2.8: Isometric view of the final FE model of the aortic valve 53
Figure 2.9: Reduction of fluid domain mesh by eliminating unnecessary elements surrounding the coronary arteries. 54
Figure 2.10: Separation of the fluid domain geometry in order to allow for mapping of 2D elements. 55

Figure 2.11: The geometry created to define boundaries for interior and exterior meshes of the fluid domain, relative to the structural mesh. 59
Figure 2.12: Images of (a) initial block creation, and (b) its projection to the aortic wall geometry and (c) the corresponding block in the computational domain. The mesh refinement required for spherical adaptors of coronary artery meshes is shown in (d) hide view and (e) wire view and (f) the refined block mesh in the computational environment. 60
Figure 2.13: (a) Fill view, (b) wire view, and (c) computational block of the Interior mesh of the aortic root. 61
Figure 2.14: Initial block of the internal portion of the right coronary fluid mesh in (a) PHE and (b) CE and (c) its projection to the coronary artery structure after (d) block elimination in CE to accommodate for butterfly mesh. Final fluid mesh of the (e) right and (f) left coronary arteries and their male spherical projection that fits into the female receptor of the aortic root and (g) their merge to the aortic root. 63
Figure 2.15: The initial projection of the main fluid block in the (a) PHE and (b) CE. This projection is followed by (c) the projection of the two side voids onto the coronary exterior surface and (d) necessary refinement of the indices in CE. (e) A close up of the fluid mesh better reveals the projection procedure while (f) shows the merging of the main fluid mesh and the previously defined parts. 64
Figure 2.16: (a) the right coronary exterior block in PHE prior to (b) projection onto the surface of coronary exterior. The final mesh of the (c) right and (d) left coronary exterior. 65
Figure 2.17: (a) The addition of coronary exterior to the aortic root; and (b) main fluid mesh. (c)The final mesh of the Eulerian domain after merging its individual parts. 66
Figure 2.18: Side/front view representation of the geometric models of the coronary stenosis and their respective percentage of area stenosis (taken from [99]) 68
Figure 2.19: The longitudinal reference line used to position the geometric coronary stenosis. . 68
Figure 2.20: Finite element mesh of the aortic root with the inclusion of coronary stenosis and their respective percentages. 69
Figure 2.21: Physiological pressures at (a) the ventricular inlet and aortic outlet, and (b) left and right coronary outlets. The aortic pressure has been deducted from the ventricular and the two coronary pressure curves in our model. 74
Figure 3.1: The computed opening and closing patterns of the leaflets, seen from the aorta..... 78

Figure 3.2: Schematic representation of clinical parameters of valvular dynamics: *ab* = rapid valve opening; *bc* = slow systolic closure; *cd* = rapid valve closing; *SCD* = slow closing displacement (edited from [129]) 79
Figure 3.3: (a) Stress distribution on the aortic leaflet during systole and (b) illustration of the selected elements where the von Mises stresses are calculated. Image (c) represents the circular patterns observed in the stress distribution on the leaflets. 81
Figure 3.4: Locations at which velocity values were measured 83
Figure 3.5: Velocity curves during a cardiac cycle at (a) sinotubular junction and commissure and (b) left coronary ostium and (c) right coronary ostium 83
Figure 3.6: Behaviour of coronary peak velocity as a function of varying (a) aortic wall stiffness and 85
Figure 3.7: The impact of coronary ostia location on Coronary flow 88
Figure 3.8: Leaflet dynamics comparison between normal, severe aortic wall thickening and leaflet stiffening 92
Figure 3.9: Schematic drawing of the impact of aortic root distensibility on leaflet free margins [157] 93
Figure 3.10: Comparison of leaflet tip circumferential displacement between the healthy and pathological cases. 94
Figure 3.11: Diastolic recirculation zones (circled with dashed line) captured in the global model of the aortic valve 96
Figure 3.12: Aortic velocity and coronary flow measurements in the healthy model 96
Figure 3.13: Cross sections at which velocity profile are calculated along the coronary arteries and the corresponding numbering system used for identification 97
Figure 3.14: Comparison of velocity profiles along the left and right coronary arteries between normal and aortic leaflet stiffening at the corresponding cross section (CS). 98
Figure 3.15: Comparison of velocity profiles along the left and right coronary arteries between normal and aortic wall stiffening at the corresponding cross section (CS). 99
Figure 3.16: Shear stress variation at the selected cross sections for wall stiffness in a) left coronary, b) right coronary, and leaflet stiffness in c) left coronary, d) right coronary 101
Figure 3.17: Coronary flow variations due to pathological cases of cardiac tissue a) thickening and b) stiffening 102

Figure 3.18: Comparison of commissural expansion measurements between different percentages of occluded coronary models and the normal global model. 104
Figure 3.19: Comparison of individual leaflet tip displacement of the aortic valve in normal and pathological coronary arteries. 105

List of Tables

Table 1-1: Comparison between our model and recent numerical models of the aortic valve region 43
Table 2-1: Normalized values of height and diameter at certain key locations obtained from previous studies to create the aortic valve model. 46
Table 3-1: Comparison between FSI and echocardiography leaflet dynamics..... 80
Table 3-2: Comparison of the maximum stress (MPa) during the cardiac cycle in selected locations represented in Figure 3.3 (b) between our model and the model by Gnyaneshwar et al. 82
Table 3-3: Rapid valve opening and closing velocities and times for the healthy model, pathological models and their corresponding average values from echocardiography 90

Chapter 1 : Introduction

In this chapter, an introductory background will be presented on the clinical aspect of the aortic valve and coronary arteries morphology, physiology and functionality. The most prevalent pathologies of these regions as well as their corresponding surgical treatments will be discussed. The motivation/goal of this thesis is firmly rooted within the clinical problems presented in this section and since engineering is intertwined to the understanding of these issues and providing the necessary solution for them, this section is later followed by the engineering background. In the engineering background, different numerical methods used in modeling of the aortic valve will be presented and compared with one another. Moreover, the methodology used in this thesis will be discussed in details while a brief history of recent similar research will be included to locate the work included in this thesis relative to other research in this area.

1.1 Clinical background

1.1.1 The heart and the circulatory system

The main components of the human cardiovascular system are the heart, blood, and blood vasculature. The purpose of this complicated system in the human body is to transport oxygen and other nutrients such as amino acids, gases, hormones, blood cells, etc. to and from cells in the body, maintaining a proper body temperature, and an array of other actions. The cardiovascular system can be divided into two circulations: the pulmonary and the systemic circulation. A schematic representing these two circulations is shown in Figure 1.1. The pulmonary circulation is a loop through which the blood becomes oxygenated; and the systemic circulation, is the portion of the cardiovascular system which transports oxygenated blood away from the heart, to the rest of the body, and returns oxygen-depleted blood back to the heart.

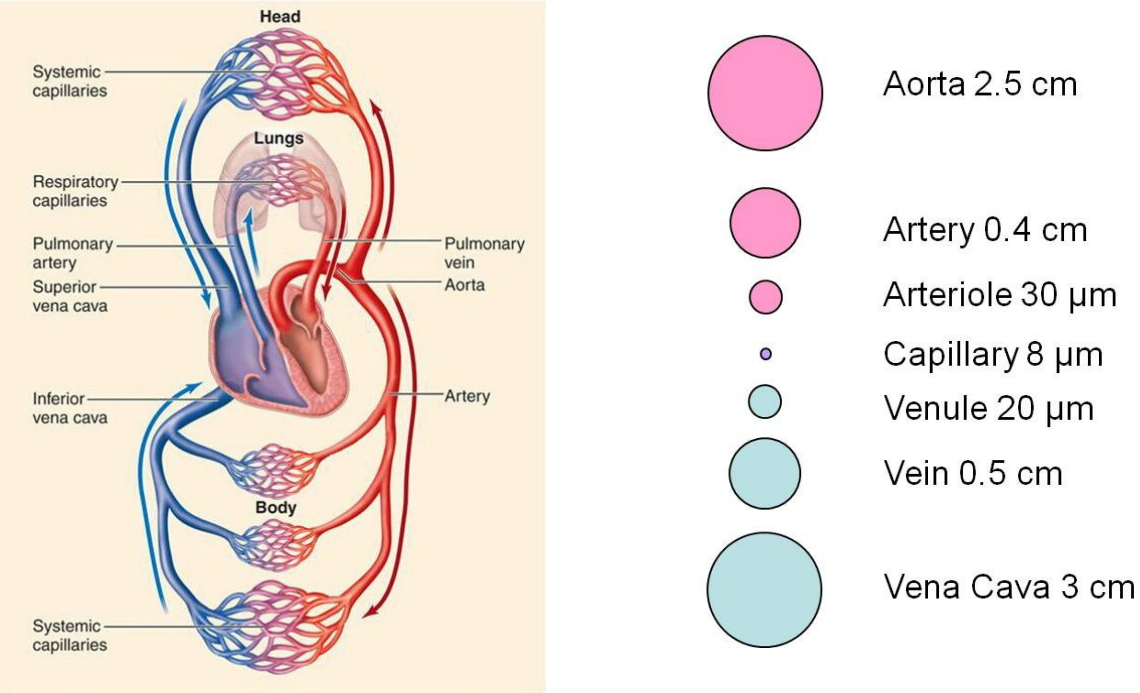

Figure 1.1: The circulatory system in human body [adapted from Baileybio (downloaded Jan 2012)].

Systemic circulation is, length-wise, much longer than pulmonary circulation, transporting blood to every cell in the body. However, one should not overlook the circulatory system which provides blood supply to the heart and its muscles: the coronary circulation. Any change in this system will affect the heart directly, potentially leading to serious pathologies and even death.

The heart pumps oxygenated blood to different organs of the body and deoxygenated blood to the lungs. The heart is comprised of four chambers: two atria (on top) and two ventricles (at the bottom). Each atrium and ventricle forms one side of the heart creating the left and right divisions of the heart. Each side either contributes to the systemic or pulmonary circulation. The blood that is returned to the right atrium is deoxygenated and passes into the right ventricle to be pumped through the pulmonary artery and eventually to the lungs for re-oxygenation and removal of carbon dioxide. The left atrium receives newly oxygenated blood from the lungs as well as the pulmonary vein which is passed into the strong left ventricle to be pumped through the aorta, to the different organs of the body as shown in Figure 1.2.

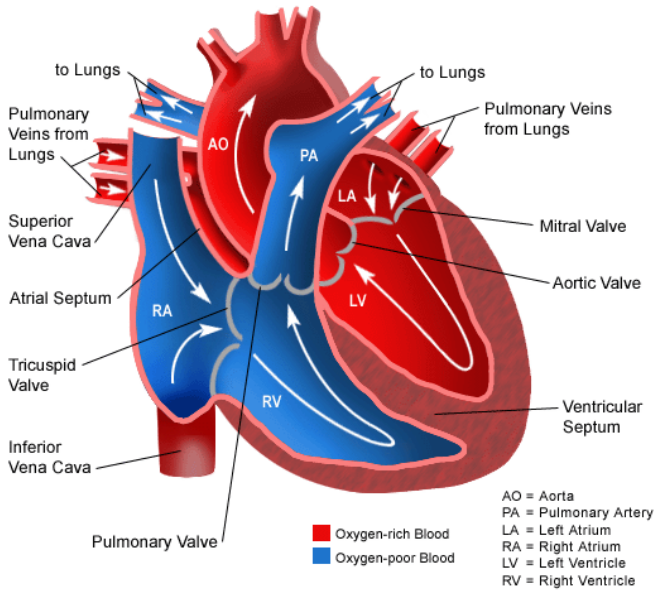

Figure 1.2: Schematic representation of heart anatomy including its chambers and valves [adapted from CHOP (downloaded Jan 2012)].

In order to allow for proper direction of flow in the circulatory system, a unidirectional valve is located at the inlet and outlet of each ventricle. These valves and their proximity to each other are represented in Figure 1.3 below. The aortic valve is one of these four valves which direct the blood flow through different chambers of the heart. It is situated at the outlet of the left ventricle just prior to the ascending aorta.

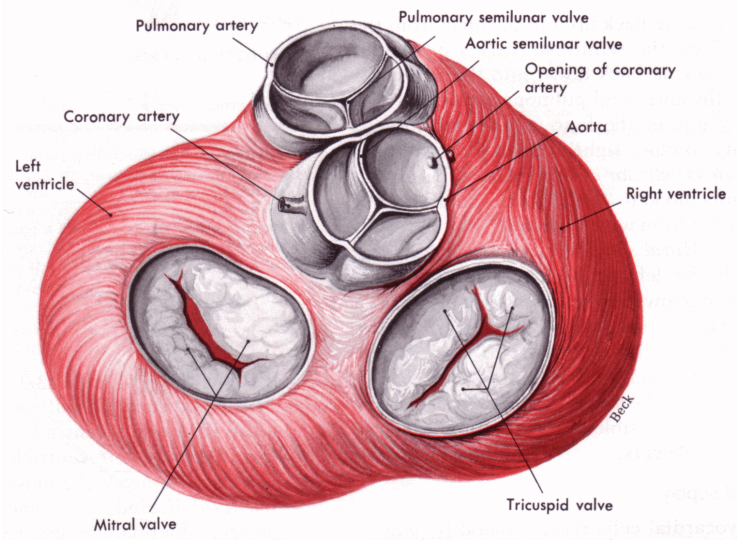

Figure 1.3: The heart valves viewed from above. The atria are removed to expose the mitral and tricuspid valves [adapted from Arthurs clip arts (downloaded Jan 2012)].

The aortic valve is a passive structure which allows blood to flow from the left ventricle into the aorta, and prevents its back-flow into the ventricle. Aortic valve pathology is the most frequent amongst heart valve diseases and has a more direct impact on health status which puts a significant importance on the functionality of this valve [1].

1.1.2 Aortic valve

1.1.2.a Morphology of the aortic valve

Aortic valve refers to the connecting region between the left ventricle and the ascending aorta. The natural valve consists of three highly flexible leaflets (also called cusps) and the aortic root. This root is the supporting structure for the three leaflets and contains three bulging structures referred to as the sinuses of Valsalva. Two of these sinuses have an outlet called the ostium from which the coronary arteries, that feed the heart muscles, initiate. The third sinus is referred to as the non-coronary sinus. The anatomical geometry of the leaflets has an important role in the functioning of the aortic valve as presented in Figure 1.4. Each cusp is attached to the sinus portion of the aortic root via an attachment line which forms a "U" shape. The top portions of this line are referred to as the commissures. Each commissure is shared between the adjacent leaflets at the level of sinotubular junction (STJ). Neighboring commissures are connected to one another through the free edge of each leaflet also called the coaptation area since during valve closure these free edges come in contact with each other and create the necessary closure of this valve. The middle section of this free edge, the tip of the leaflet, is a thicker structure named the nodulus of Arantius which is lower in height compared to the commissures and aids in valve closure.

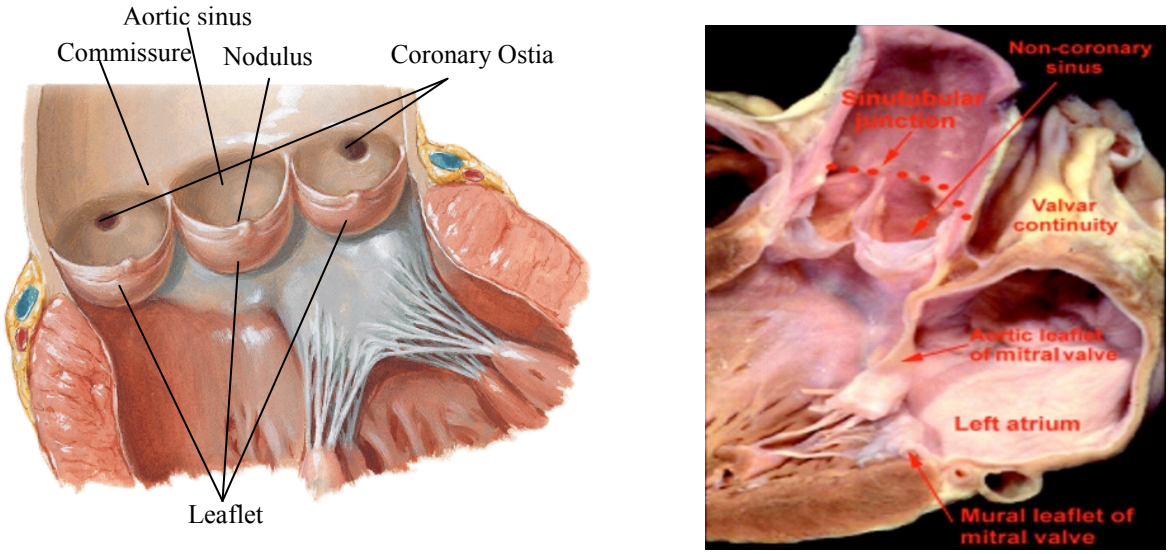

(a) (b)

Figure 1.4: (a) Schematic drawing of the aortic valve and its components and (b) longitudinal cross section of the left ventricle exposing the aortic valve, ascending aorta and left atrium [2].

The remaining, non-coapting surface area of the leaflet is in the shape of a belly and is actually the load bearing portion. The reason behind this load bearing capacity lies in the natural composition and structure of the leaflets. Three differently architectured layers comprise the leaflets (shown in Figure 1.5) which provide its extraordinary capability of undergoing very large deformations under physiological loads in every heart beat. These layers are mainly composed of elastin and collagen fibers. However, the relative amount, ratio and orientation of these components vary in each individual layer, creating different mechanical characteristics [3-5].

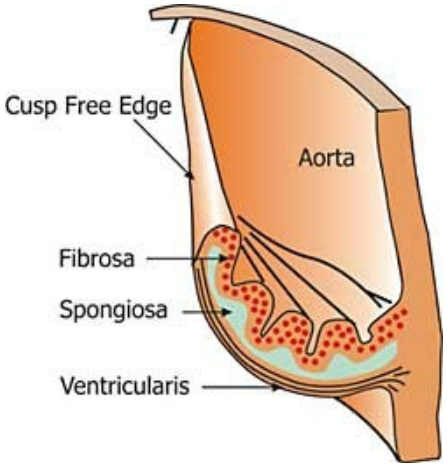

Figure 1.5: Different structural layers of aortic cusps including fibrosa, spongiosa, ventricularis. [adapted from cardiothoracic surgery of USC (downloaded January 2012)].

The layer closest to the ascending aorta towards the outflow is called “fibrosa” which mostly contains circumferentially aligned collagen fibers. This layer is the most load-bearing layer of the leaflet and prevents it from excessive stretching [6, 7]. The middle layer, the spongiosa, consists of a rich amount of proteoglycans and also an array of collagen fibers without a specific trend in their orientation. This layer aids in shock dissipation during valve closure due to the existence of proteoglycans and their ability to absorb water and swell. The ventricularis, the layer facing the ventricle and the inflow, is primarily composed of radially aligned elastin fibers which allows for a much greater extensibility in this direction [3-5]. This anisotropic behavior is more obvious in the fibrosa and ventricularis layers compared to spongiosa due to the more uniform orientation of elastin and collagen fibers. However the overall mechanical property of the leaflet is the combination of these individual layers. In the circumferential direction, the mechanical behavior exhibits the properties of collagen bundles, whilst in the radial direction the elastin mesh is the predominant factor. Even though the percentage of elastin fibers is less than the collagen fibers, their existence and their function in the leaflets should not be neglected nor underestimated. Elastins are present through the entire thickness of the leaflets and act as energy storing springs while they are being stretched. This energy is then released (used) to aid in bringing back the leaflets to their original position and geometry. The natural open and closed position of the aortic valve is represented in Figure 1.6.

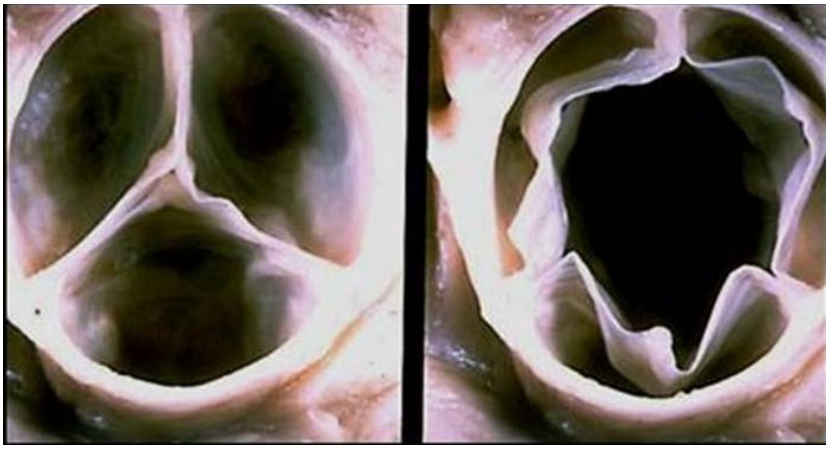

Figure 1.6: Top view of open and closed positions of aortic valve

[by Michael Hoaglin uploaded Sep 27, 2009].

The anatomy of the aortic valve is quite difficult to describe. Throughout the years different values have been reported and measured at different sections of the valve. These values are dependent on the age, sex, health condition and other parameters of the patient it was measured from. Average values from various measurements are used in general to describe the overall anatomy of this structure.

1.1.2.b Function of the aortic valve

Aortic valve as one of the four valves in the heart chamber plays an important role during the cardiac cycle. It allows for a unidirectional flow from the left ventricle towards the ascending aorta in the cardiac cycle. This cycle can be divided into two phases: The systolic and the diastolic interval. During diastole the left ventricle fills with blood from the atria. This blood is then ejected during systole into the aorta due to an isovolumic contraction of the left ventricle. This period is then followed by an isovolumic relaxation of the ventricle during which the valve stays closed.

The aortic valve is considered to be a passive valve in that its opening and closing are solely driven by the pressure difference/gradient between the ascending aorta and the ventricle. This difference during diastole induces large deformations and torsions on the leaflets. Leaflet coaptation plays an important role in inhibiting leaflet prolapse due to the aforementioned large deformation and hence backflow into the ventricle.

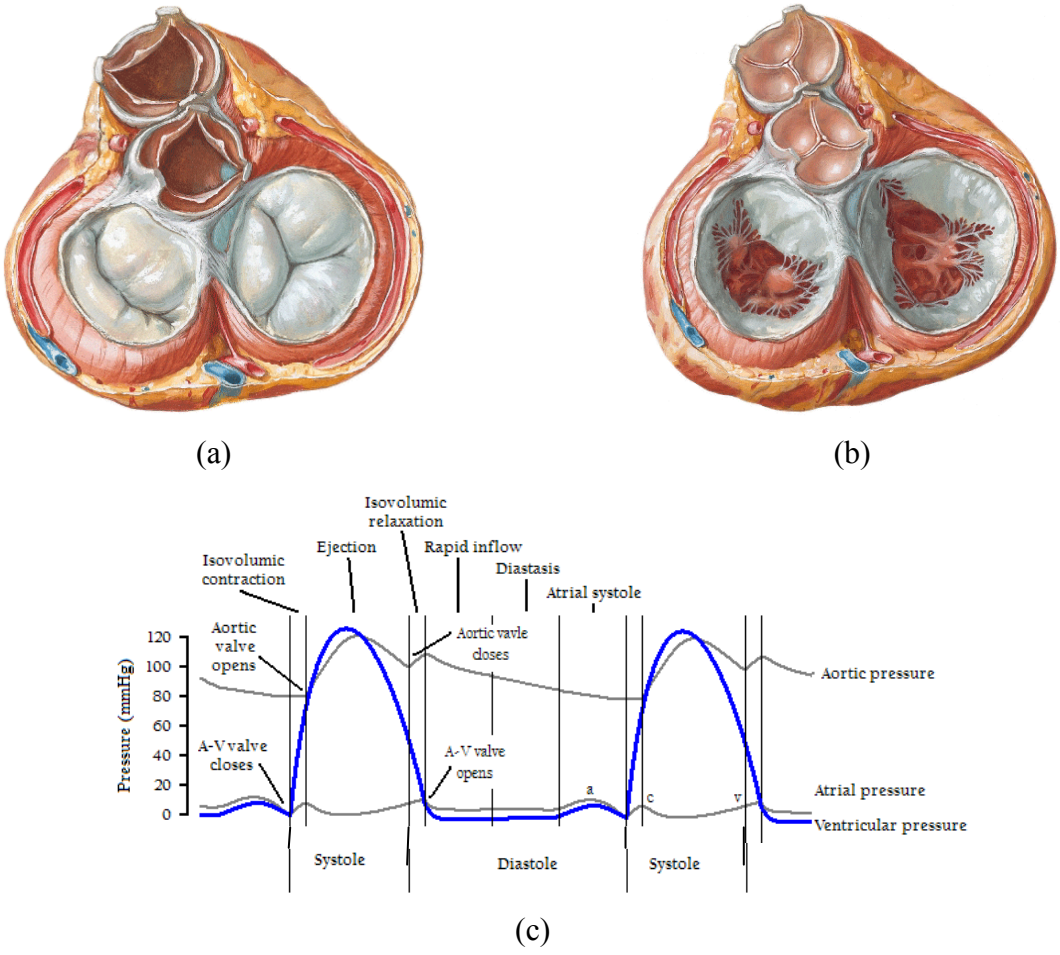

Figure 1.7: Heart valves during (a) systole and (b) diastole [by F. Netter from CICMD (downloaded Jan 2012)], and the diagram of one cardiac cycle [by Destiny Qx from Wikipedia (downloaded Jan 2012)].

The dynamics of a normal aortic valve during one cardiac cycle can be divided into: a rapid opening followed by a slow closing phase during systole; and a closed phase during diastole [8]. The slow closing phase is induced by the deceleration of the blood flow through the valve. Small vortices are generated in the sinus pouches, which are thought to initiate and aid in valve closure. Interestingly, even though at peak flow during systole values of the Reynolds number (ratio of inertial forces to viscous forces) reach up to 4500, only in the case of a diseased valve the flow might become turbulent. Otherwise a laminar flow is prevalent [9].

1.1.2.c Pathologies of the aortic valve

There are several pathologies that could impact the aortic valve. However most of these pathologies can be categorized as stenotic or insufficient cases or both simultaneously. In the case of a stenotic valve the cardiac tissue, mostly the leaflets, become thicker and stiffer as shown in Figure 1.8.

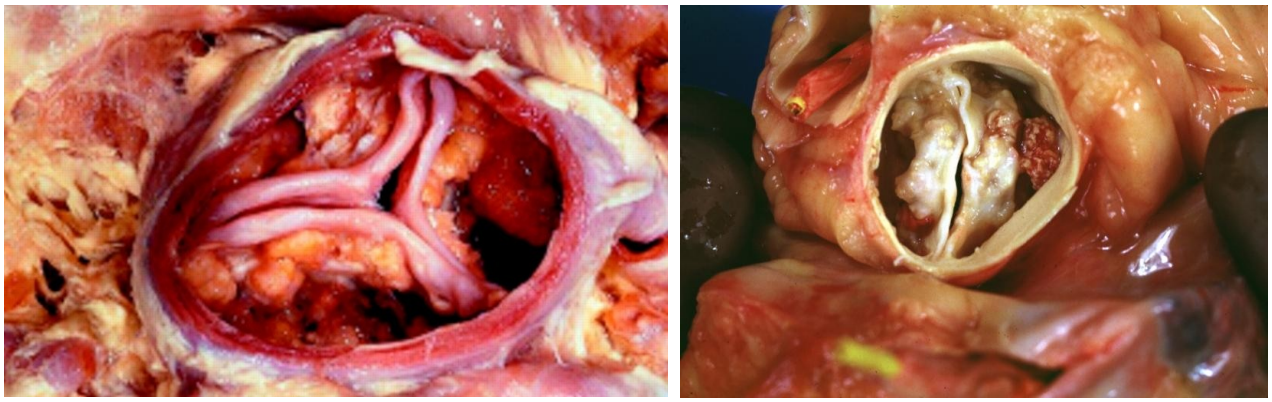

(a) (b)

Figure 1.8: Severely stenotic (a) tricuspid and (b) bicuspid aortic valve [by Peter Anderson from Wikipedia (downloaded Jan 2012)].

One of the visual means by which aortic stenosis is diagnosed is by observing the maximum opening area of the leaflet tips at a cross section normal to the blood flow, commonly referred to as "geometric orifice area" (GOA) or "aortic valve area" (AVA). There is also the area under which the jet of the flow exits the valve which is called "effective orifice area" (EOA). Aortic stenosis leads to a reduced effective/geometric orifice area compared to a healthy valve and will also cause a reduction in blood flow passing through the valve. The cardiovascular system will try to compensate for this problem by pumping more blood into the aorta. This is normally achieved by one of the two following means: either an increase in the heart rate (number of times the ventricle would contract), or an increase in the pump's power (the ventricle's muscular contractile power). An increase/decrease in the heart rate is a normal phenomenon that we unconsciously deal with in everyday tasks we undertake. However, a constant increase in heart rate due to pathology puts a lot of stress on the cardiac system, especially when the stage of the disease is quite severe and could lead to consecutive diseases such as arrhythmia and shortness of breath during exercise. The frequent causes for aortic

stenosis are calcification and fibrosis of the leaflet tissues [10, 11]. The severity of aortic stenosis is normally determined by means of Echocardiography with simultaneous velocity measurements from Doppler to evaluate its severity. A normal valve has an average aortic valve area ranging between 3 – 4 cm^2, while this value is reduced for the moderate and severe cases to 1 - 1.5 cm^2 and less than 1 cm^2, respectively.

Insufficient valves on the other hand are scenarios in which, the coaptation area of the leaflets are compromised and the leaflets do not create a proper seal, specifically during diastole, in their closed position. This will affect their performance as a unidirectional valve and will allow back flow into the left ventricle as shown in Figure 1.9. To compensate for the reduced blood flow, the ventricular volume and wall thickness gradually increase until they fail to sustain with the extra workload. Aortic insufficiency is normally observed to occur either by itself or in combination with aortic stenosis. One of the main reasons behind aortic insufficiency is known to be aortic root enlargement, where the root diameter exceeds healthy and acceptable diameters as well as rheumatic heart disease and congenital pathologies such as bicuspid valves and Marfan syndrome [12, 13]. In order to indicate and quantify left ventricular end-systolic and end-diastolic dimensions, ejection fraction, aortic regurgitation orifice and volume, echocardiography and cardiovascular magnetic resonance are used. These pathologies are tolerated by the cardiac system to some extent without noticeable impact and compromise to the individual's health.

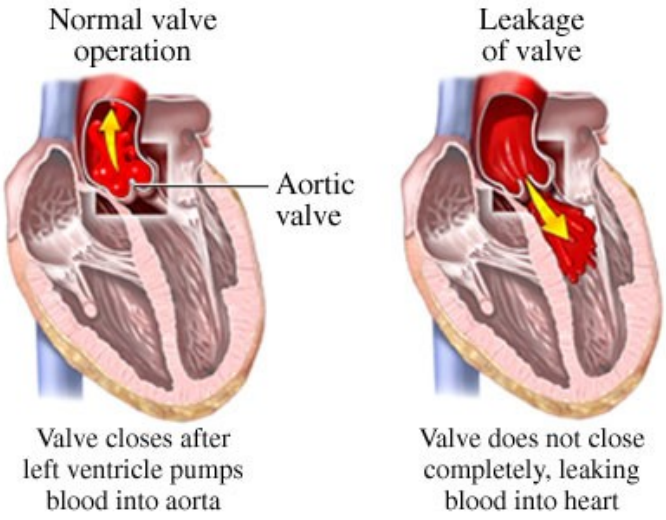

(a)

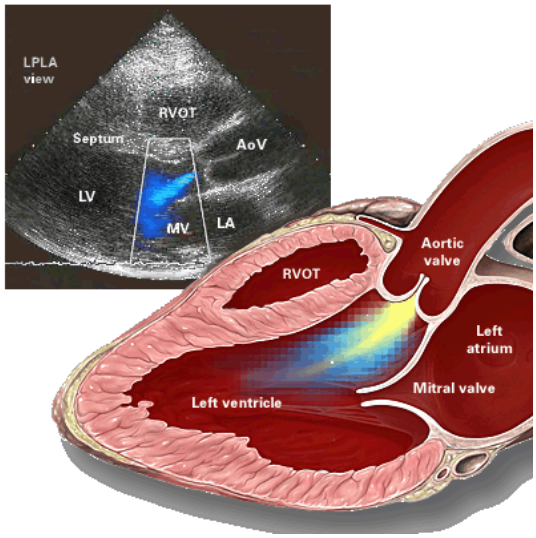

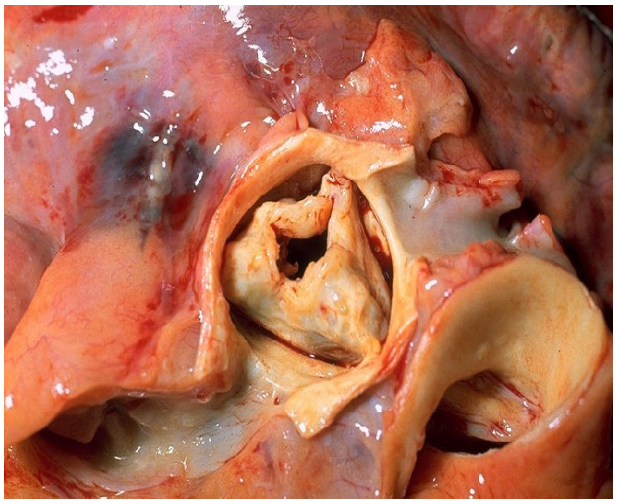

(b) (c)

Figure 1.9: (a) Schematic drawing and (b) Doppler image of blood leakage into the left ventricle due to aortic regurgitation [adapted from heart valve surgery (downloaded Jan 2012)]. Image (c) shows a severe aortic insufficiency causing a permanent opening of the leaflets [from Kadiol (downloaded Jan 2012)].

1.1.2.d Treatment of the aortic valve

Pathologies of the aortic valve either involve the leaflets, the aortic root or both. Unfortunately despite all the ongoing research that has been carried out, there is not yet a solution to these diseases that would permanently rejuvenate and preserve the natural functionality of this region. An immense effort however has been put in place to minimize the

consequent alterations due to any type of treatment performed on aortic valve. There are several factors that need to be considered prior to deciding the type of treatment such as: the age and gender of the patient, the state of the surrounding structures and the severity of the disease.

In the case of a pathological leaflet depending on the severity of the case, three options are available: mechanical or bio-prosthetic valves and reconstructive surgery as shown in Figure 1.10.

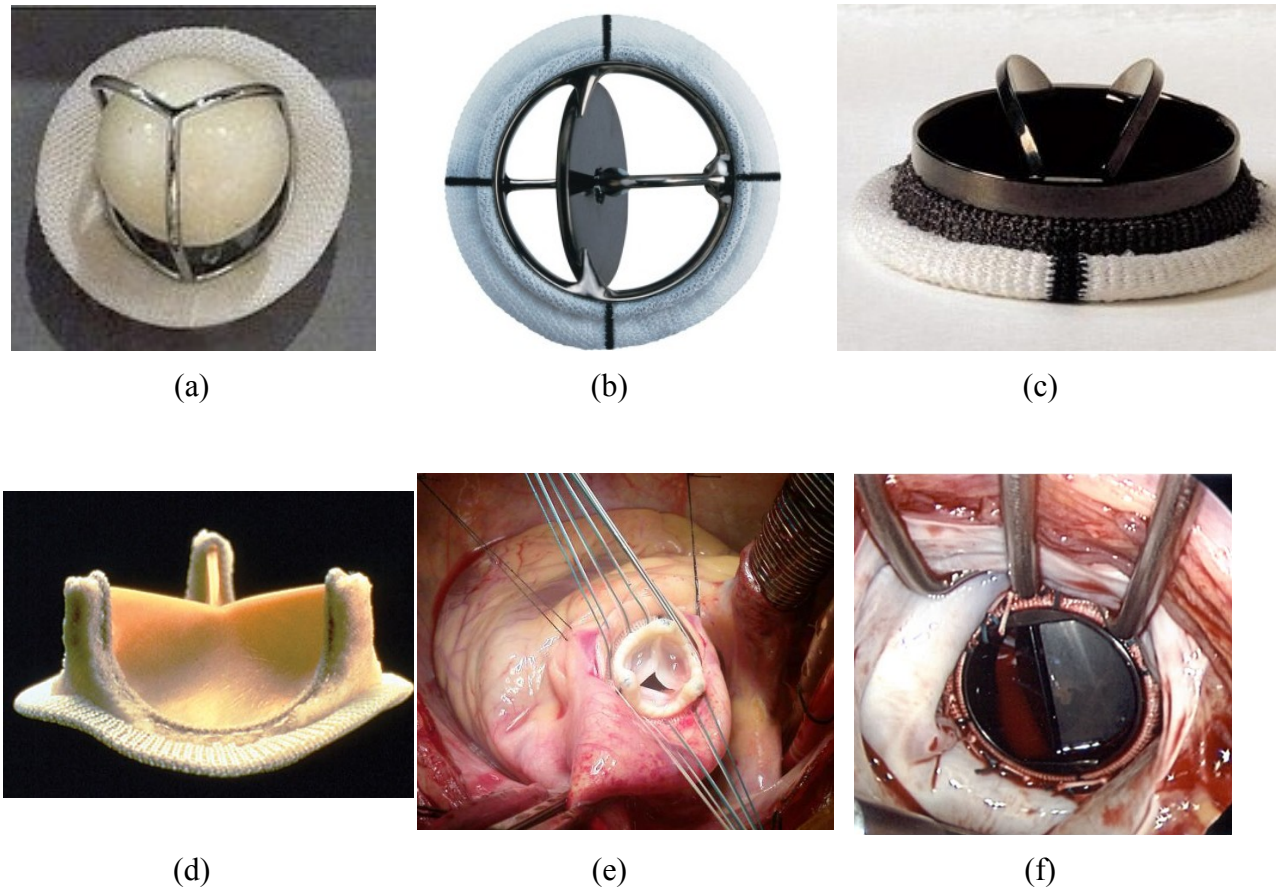

(a) (b) (c)

(d) (e) (f)

Figure 1.10: (a) Ball and cage, (b) mono tilting [by Mirko Junge, downloaded Jan 2012), and (c) double tilting mechanical valve [adapted from gknmhospital (downloaded Jan2012)], and (d) a bio-prosthetic aortic valve. Implantation of (e) a bio-prosthetic valve versus (f) a mechanical valve [14].

Reconstructive surgery usually applies solely to insufficient valves since, for a wide variety of valve dysfunctions such as rheumatic disease and moderate to severe calcification and stenosis, surgical repairs such as valvuloplasty or calcium removal are neither effective nor durable and hence are not practiced regularly by surgeons. Instead, a more dramatic approach is necessary which involves removal of the leaflets and replacing them with a prosthetic valve. The

efficiency, life expectancy and hemodynamic variations compared to the natural valve differ significantly between mechanical and bio-prosthetic valves. Mechanical valves are more durable and rigid and therefore tend to be more suitable for younger patients with longer life expectancy.

However, this same property reduces their capability in reproducing the physiological hemodynamics. Their rigid structure causes damage to blood cells requiring life-long administration of anti-coagulants to prevent thromboembolic complications. Mechanical valves have been used for many years and as a consequence different designs have been proposed throughout the years two of which are more frequently used: the mono tilting and the double tilting disc. A cumulative risk for hemorrhage and thrombosis associated with mechanical valves inspired the development of bio-prosthetic valves. Such valves are typically made from either bovine or porcine tissue, treated with gluteraldehyde. This treatment preserves the tissue, and reduces tissue rejection [15, 16]. Despite the fact that this procedure causes the tissue to lose some of its flexibility, bio-prosthetic valves still have a lower rate of complications as well as thromboembolism. However, most fall short due to calcification, tissue degeneration and perforation caused by mechanical stress.

If the entire aortic valve is pathological, the leaflets and the aortic root will be replaced by bio-/prosthetics and a Dacron graft (i.e. Bentall Procedure). However, in scenarios where the aortic leaflets seem to be in healthy condition and only the surrounding tissue is pathological, in order to inflict the least amount of anatomical and physiological variation, only the diseased tissue will be replaced. Based on the assessment of the patient, there are several procedures that the surgeon could choose from. Some of the common procedures include: re-implantation and remodeling. A schematic drawing showing a side by side comparison between these techniques is presented in Figure 1.11.

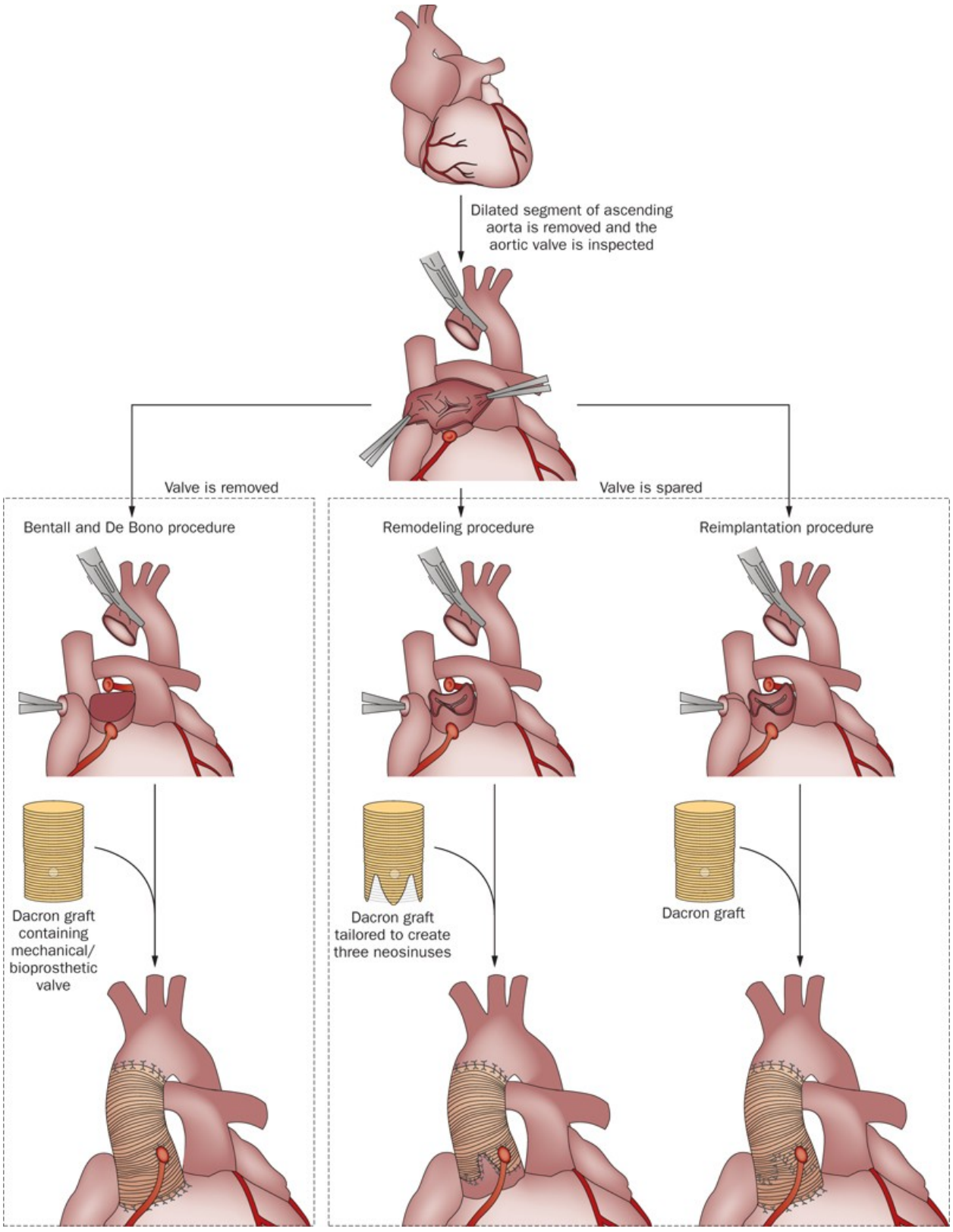

Figure 1.11: Comparison between Bentall, remodeling and re-implantation techniques [17].

In the re-implantation technique, known as David procedure, the native leaflets will be sutured (re-implanted) into the straight Dacron graft which replaces the aortic root; and the two coronaries will be sutured to the two openings created on the graft. This procedure is presented in Figure 1.12 below.

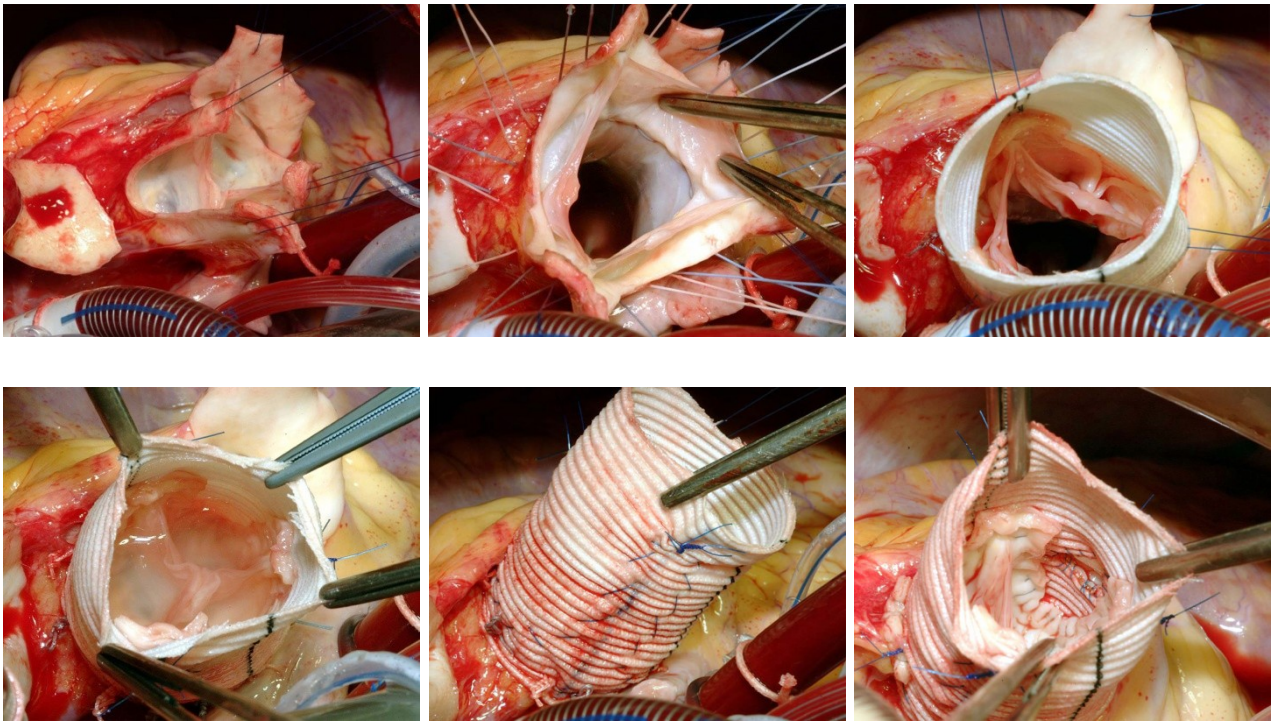

Figure 1.12: Step by step demonstration of the re-implantation (David's) procedure [18].

The remodeling surgery (known as Yacoub/David II procedure) is similar in concept but it preserves and mimics the anatomy of the aortic root more closely. It uses a scalloped design to create a new aortic root out of Dacron. This scalloped shape can be achieved by either cutting the graft into three pieces or by tailoring a four piece art (including the three Dacron sinuses and the cylindrical tube) and suturing them to the matching aortic root as shown in Figure 1.13. In more moderate cases of valvular disease, the root can be narrowed by means of commissuroplasty. Sutures will be placed on the aortic root to reduce aortic valve area and the associated regurgitation. In paediatric surgery, more sophisticated approaches might be taken such as leaflet shortening, suturing the free edges or the cusp-sinus line of attachment.

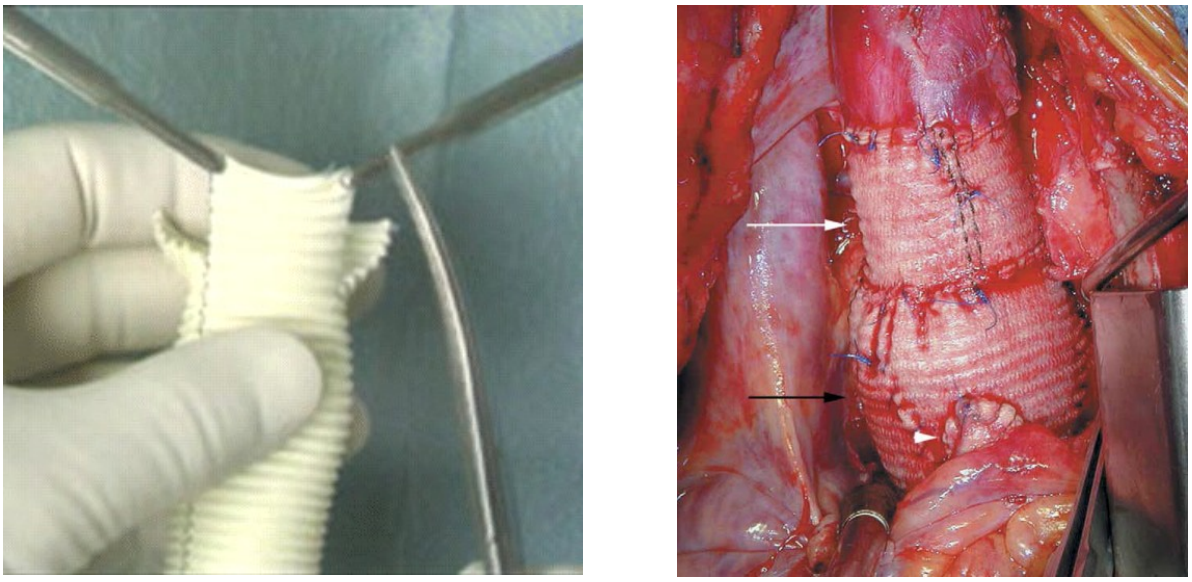

(a) (b)

Figure 1.13: (a) Incisions cut into the Dacron graft to accommodate for the remodeling surgery and (b) an example of the finished procedure [19].

1.1.3 Coronary arteries

1.1.3.a Physiology of coronary arteries

Coronary arteries are the vessels that supply the myocardium with blood. Their anatomical location on the sinus of Valsalva, from which they initiate, is referred to as ostium. The left coronary artery originates from the left aortic sinus, while the right coronary artery originates from the right aortic sinus, both just above the aortic cusps. These vessels have a highly curved geometry right out of the two ostia. The left coronary artery further divides into two branches: the left anterior descending (LAD) and the left circumflex branch (LCX). Figure 1.14 shows these arteries in an anterior view of the heart.

The myocardium blood supply can generally be divided into groups: ones that run deep into the heart muscles called the subendocardial, and the ones that run mostly at the surface of the myocardium referred to as epicardial. During systole due to contraction of the ventricular myocardium, the subendocardial vessels are compressed and therefore the blood flow in the subendocardium reduces significantly if not completely. There is still some perfusion through the epicardial arteries. However most of the coronary perfusion occurs during the diastolic phase in which the ventricular muscles relax.

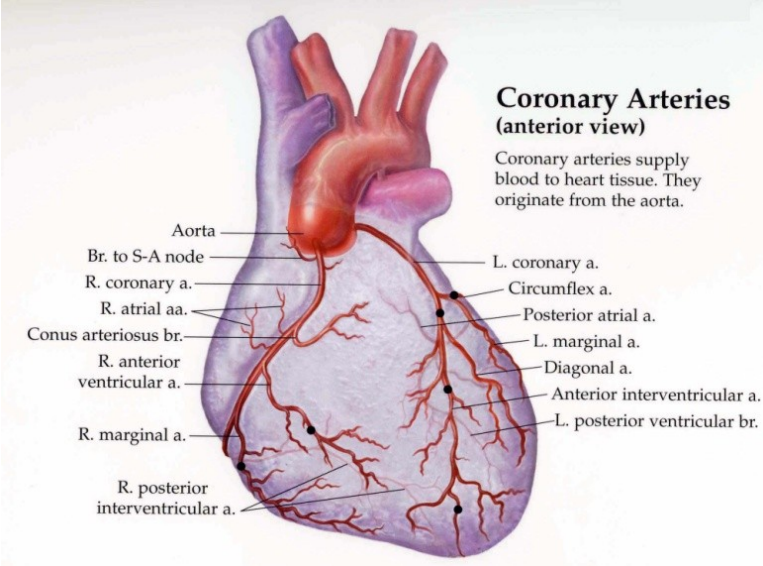

Figure 1.14: Anterior view of the coronary arteries and their downstream branching. [from medical atlas (downloaded Feb 2012)].

There are several factors that aid in the perfusion of blood into the coronary arteries: the ventricular pressure, compliance of the aortic root, auto-regulation (the intrinsic ability to maintain a constant blood flow despite changes in perfusion pressure), duration of diastole and downstream resistance of the subendocardial arteries. Any change in these factors would affect the blood flow into these arteries, however as mentioned, autoregulation would compensate for minor variations.

1.1.3.b Pathologies of the coronary arteries

Coronary artery disease (CAD) or myocardial infarction is caused by the atherosclerosis process which is thickening and calcification of the arterial wall. This is due to the accumulation of cholesterol and macrophages [20] beneath the endothelial cells which later transform into an atherosclerotic plaque [21]. There are several well-known risk factors associated with coronary artery disease. Some of the factors include heavy smoking, high levels of alcohol consumption, unhealthy diet, lack of physical activity, diabetes, hypercholesterolemia, hypertension and genetic factors. The increasing accumulation of atherosclerotic lesions (plaque creation) leads into the enlargement of the arterial wall, a remodeling response from the tissue. This is the main reason why atherosclerosis is a clinically silent disease and cannot be detected at the preliminary stages. It is possible for large atherosclerotic lesions to accumulate for years without a noticeable

impact on blood flow or symptoms [22]. Often times CAD gets diagnosed after a 50-75 percent occlusion incidence in the arteries [23]. Figure 1.15 represents the progression of atherosclerosis and its possible outcomes in the coronary arteries. There are also major factors affecting the hemodynamics of these arteries which can be broadly categorized into: vessel geometry, arterial compliance, inlet flow conditions, velocity profile along the vessel (low or oscillatory wall shear stress) [20, 24] and branching of the arteries [25].

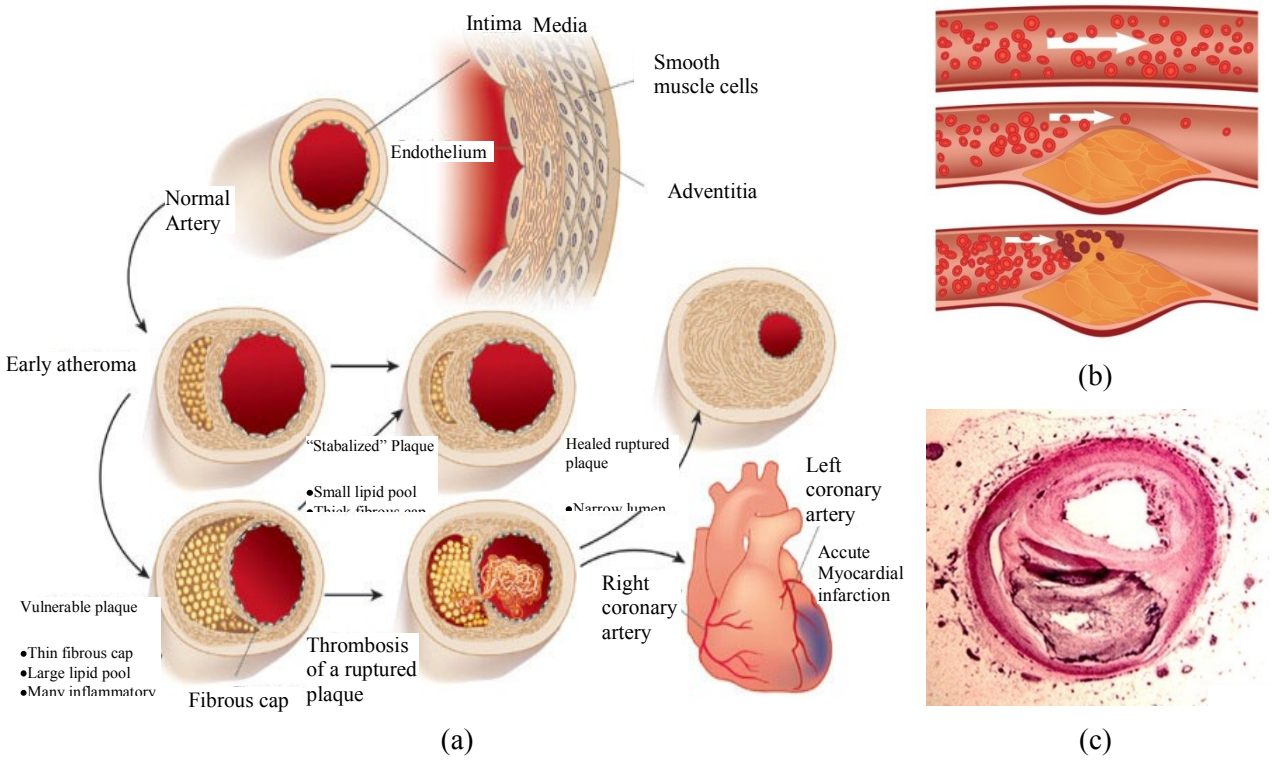

Figure 1.15: (a) Initiation, progression, and complication of human coronary atherosclerotic plaque [26] (b) and its effect on blood flow [from OMNImedicalcenter, (downloaded 2012)]. Image (c) represents a typical eccentric atherosclerotic plaque [from brownmed [downloaded Feb 2012)].

There are two common outcomes associated with this pathology depending if the formed plaque is stable or vulnerable. In the case of a stable plaque, the continuous accumulation of lesion causes a reduction in vessel diameter (stenosis) and blood flow, resulting in symptoms such as reversible ischemia during physical activity (angina). In the case of a vulnerable plaque however, the fibrous cap can rupture causing the exposure of sub-endothelial collagen and lipid. This may result in thrombosis which blocks the artery, and significantly or completely stops the blood supply to myocardium [22]. The thrombus could also travel downstream of the blood flow

towards smaller vessels and cause a blockage at that level, leading to stroke, ulcers and kidney malfunction [27].

1.1.3.c Coronary artery disease diagnosis

Several procedures are available to the cardiologist for diagnosis and assessment of coronary artery diseases ranging from invasive and accurate procedures to non-invasive and less accurate. The decision on which methodology to use is made on a patient specific basis. The common invasive methodologies include imaging and visual observation of either the flow pattern or the geometry of the coronary arteries such as angiography and echocardiograms. Less invasive methods usually employ the natural functionality of the cardiac system and an electrocardiogram (ECG) monitor to determine the existence and severity of the disease.

Coronary angiography is a routine procedure and involves insertion of a catheter into either the groin or the arm of the patient which is then manoeuvred through the vasculature and up to the coronaries. Once the catheter is in place, a contrast agent (dye) is released and X-ray images are taken which depict the pathway of blood flow through the artery and any sign of occlusion as shown in Figure 1.16 (a). Depending on the angle of view, the occlusion may or may not get visualized correctly. However, with the newer imaging techniques such as magnetic resonance angiography (MRA) and computed tomography angiography (CTA) and intravascular ultrasound (IVUS) this uncertainty has been alleviated. In CTA, X-ray beams are emitted from different angles reproducing a precise anatomical description of the vessel condition with the disadvantage of exposure to large amounts of radiation [Figure 1.16 (b)]. On the other hand, MRA does not involve radiation but is more suitable for larger vessels [Figure 1.16 (c)]. IVUS is another technique which is particularly popular when it comes to coronary angiography. It is another imaging technique in which a special catheter with an ultrasound probe at the distal end is used to visualize the vessel structure [Figure 1.16 (d)]. These methods are very accurate but expensive and invasive. Figure 1.16 represents sample images of these methodologies used to diagnose coronary stenosis.

Echocardiogram is another routine method of CAD detection. Also known as cardiac ultrasound, it uses ultrasound techniques to image two-dimensional slices of the cardiac tissue. While this system cannot represent the blood flowing through the heart, it can provide valuable

data related to cardiac abnormalities [Figure 1.16 (e)]. An echocardiogram is capable of producing accurate assessment of blood velocity and cardiac tissue (cusps) at any arbitrary point using pulsed or continuous wave Doppler ultrasound. This allows assessment of cardiac valve area and function, valvular regurgitation and cardiac output as well as ejection fraction.

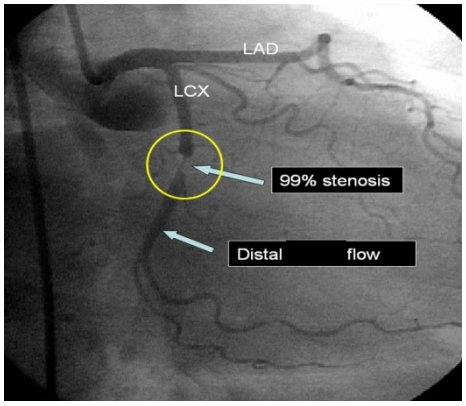

(a)

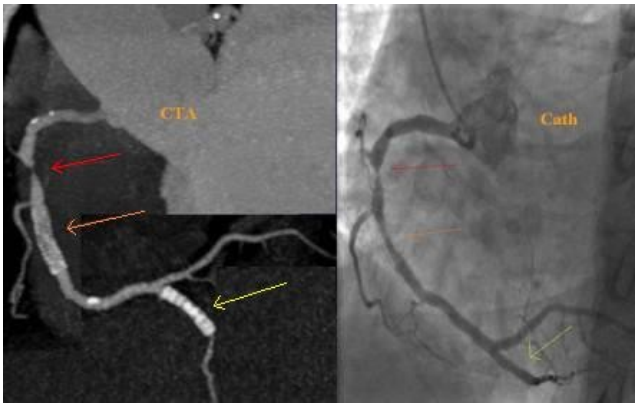

(b)

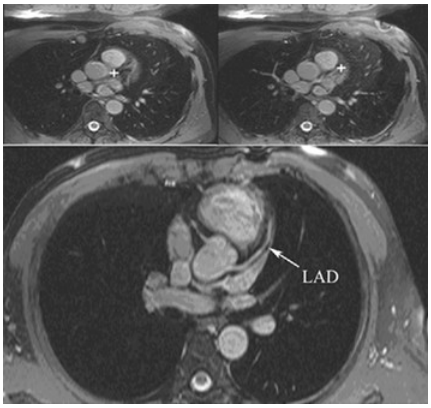

(c)

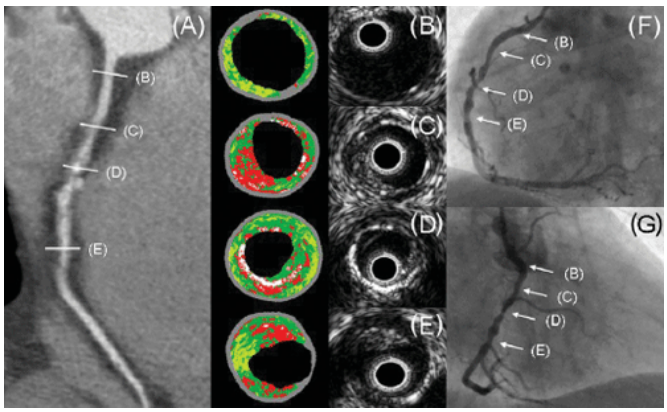

(d)

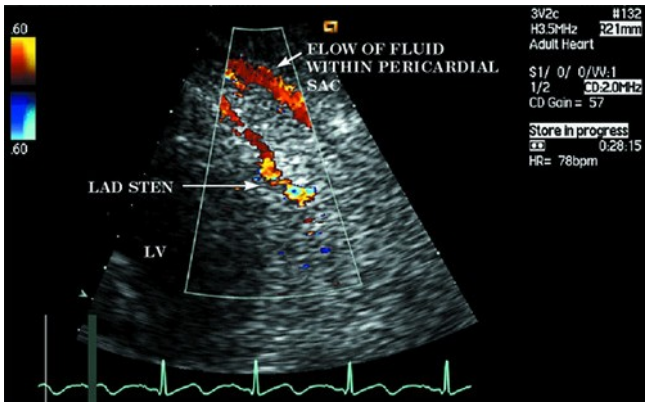

(e)

Figure 1.16: Sample images of (a) angiography, (b) CTA (from bocardiology), (c) MRA [28], (d) IVUS [29], and (e) echocardiography procedure [30].

In the past few years however, fractional flow reserve (FFR) has become quite popular in determining the severity of coronary artery disease. The assessment of when a lesion is actually problematic or correction surgery might be necessary is not clear cut. FFR is a technique used in coronary catheterization to measure pressure differences across a stenosis to determine the possibility that the occlusion would cause ischemia. Fractional flow reserve is defined as the pressure distal to a stenosis relative to the pressure proximal to the stenosis. This is another method for comparison of blood flow in the presence of stenosis to a hypothetical absence of stenosis. FFR is measured using a transducer on the tip of a guidewire to measure pressure, temperature and flow to determine the severity of the occlusion. A cut-off point of 0.75 to 0.80 is used as a clinical marker and lower values of FFR is an indication of a significant lesion. It has been shown that a FFR of < 0.75 in patients with stable angina is associated with inducible myocardial ischemia [31, 32]. Fractional flow reserve is measured during hyperemia (maximum blood flow) which can clinically be induced by injecting drugs such as adenosine. This method has certain advantages over the previous techniques mentioned above and allows a functional evaluation of the narrowing. It also accounts for collateral flow which might mitigate the existing stenosis. However, FFR is still an invasive procedure and less drastic alternatives exist which can provide the physician with preliminary data necessary for assessment of the pathological state. One of these methods is exercise testing (cardiac stress testing) in which physical exercise such as walks on treadmills or cycling on stationary bikes are used to increase the cardiac workload. Blood flow restrictions to cardiac muscle will become more pronounced on the ECG recording. This method is less accurate compared to the other methods but is a good preliminary alternative to the other expensive and invasive methods.

1.1.3.d Coronary artery disease treatment

Following a myocardial infarction, thrombolytic therapy (injection of a clot dissolving medication into the artery) helps restart blood flow to the heart and prevents a heart attack that could potentially be deadly. Administration of thrombolytic therapy within the first hour after symptoms occur would be most beneficial [33].

Angioplasty, an invasive interventional procedure involves insertion of a catheter into the vasculature and leading it to the occluded section of the diseased artery. The balloon at the tip of the catheter is then inflated to alienate the occlusion and the plaque towards the arterial wall and

reduce the narrowing caused in the artery. This procedure helps in the re-establishment of flow in the vessel [34]. In order to reduce the restenosis rate associated with balloon angioplasty, stents were affixed to the balloon-tipped catheter. Stents are wire mesh mechanical structures that are left in place after ballooning to prevent the lesions from expanding and causing a restenosis. Coronary artery bypass is another common procedure used in patients with myocardial infarction. As the name of this operation states, a bypass graft connects the proximal and distal portions of the blocked part of the coronary artery to restore the blood supply to the heart muscle.

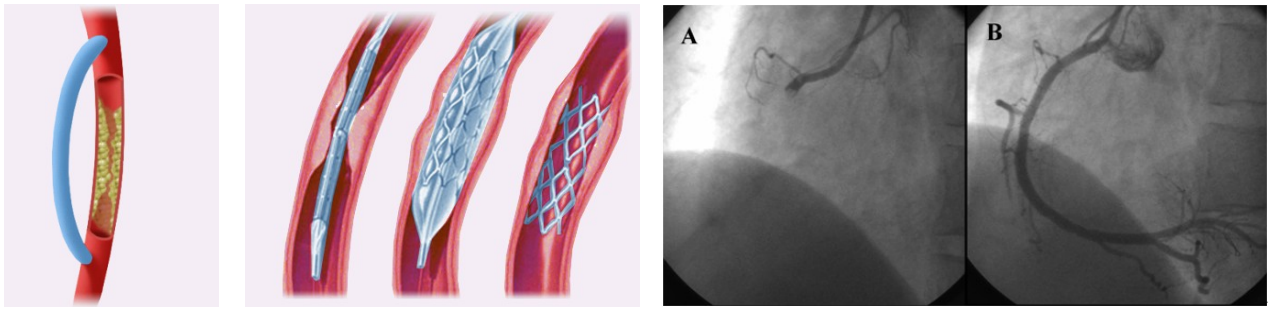

(a) (b) (c)

Figure 1.17: Schematic drawing of (a) a coronary bypass graft and (b) balloon angioplasty (PTCA) [by N. Paraskevas (downloaded Feb 2012)]. (c) Angiography images of before and after stent deployment in proximal RCA[35].

Similar to how FFR is used to assess the severity of CAD, Coronary flow reserve (CFR) is used to measure the efficacy of the above treatments. CFR is defined as the capacity of the coronary circulation to dilate following an increase in myocardial metabolic demands and can be expressed by the difference between the maximum blood flow during exercise and the flow during rest. Coronary flow reserve can be measured through a variety of methods such as Doppler echocardiography and positron emission tomography (PET).

1.2 Engineering background

Aortic valve simulation has become the focus of many investigations during the recent years. Depending on the goal of these studies different approaches, methodologies and software have been employed to achieve the results and overcome the obstacles in modeling this complex anatomy. The following sections will explain some of the most relevant numerical methods available for modeling the aortic valve region. The basis for the selection of methodologies and software used in this work will also be explored and compared to similar research that has been conducted by other groups.

1.2.1 Numerical methods

Engineering problems in general, are mathematical models of physical situations in the form of differential equations with corresponding initial and/or boundary conditions. The differential equations are derived from the application of fundamental principles and theories to a system as a means of conservation of mass, force or energy of the entire control volume. The parameters defining any engineering problem can be subdivided into two sets: 1. the parameters that define the natural behaviour of the given system such as material properties (elastic modulus, viscosity) and geometrical features (thickness, cross section area, second moment of area); and 2. the parameters affecting this natural behaviour such as external forces, pressure gradient and flow rate. Where possible, for simple problems, an exact solution can be achieved using analytical solutions. However, for many practical problems which are confronted on a daily basis, obtaining an exact solution is not possible. This is normally due to the complex nature of the system, its governing equations and boundary conditions. In order to solve such complications, numerical analysis is used which provides an approximate solution to the problem contrary to the exact solution obtained by analytical methods. There are two common types of numerical solutions: (1) finite element methods (FEM) and (2) finite difference methods (FDM). Finite difference methods are easy to comprehend and are more suitable for simple problems with isotropic material properties. In this methodology, the derivatives of the differential equations are replaced by difference equations. On the contrary, the finite element method uses the integral formulation to create a set of simultaneous algebraic equations. The basic concept in the physical FEM is the discretization of the mathematical model into many smaller, non-overlapping components of simple geometry called *finite elements* or *elements* for short. These

elements are inter-connected through a set of points referred to as *nodes*. The unknown function is calculated at these nodes in terms of a finite number of degrees of freedom (DOF). The complete solution to the mathematical model is then generated by assembling the individual solutions from all the elements of the discrete model.

In general, a numerical analysis consists of three steps: the pre-processing step, the solution and the post-processing step. The pre-processing step consists of: (1) dividing the problem/geometry into smaller and more manageable elements and nodes, (2) considering a continuous (shape) function for the elements used to represent their behaviour, (3) applying boundary and/or initial conditions. This step usually requires a great amount of human effort, time and accuracy to ensure proper problem definition and also to guarantee meaningful results. Next, a set of linear or nonlinear algebraic equations are simultaneously solved by means of numerical analysis. This is generally achieved by using an individually developed or commercially available numerical code. Nodal results such as displacement values are obtained and used in the post-processing step to reveal other valuable information such as velocities, principle and maximum stress and strains and the location at which they occur.

Methods used to solve finite element equations can generally be classified as either implicit or explicit. Both methods involve a numerical time integration scheme to solve for the unknown displacement solution, which is the basis for calculating resulting strains and stresses. However, the fundamental differences between the two methods make them case specific and care should be taken when choosing the preferred method of analysis and the corresponding FE package. The implicit approach is useful in problems where time dependency of the solution is not an important factor such as static, quasi-static and structural analysis. Explicit solutions on the other hand are most widely used in solving high deformation, time dependent problems. In an implicit method, the displacement is not a function of time and therefore the velocities and accelerations (time derivatives of displacement) become zero and the mass and damping factors can be neglected. On the contrary, the explicit method is a function of time which means velocity and acceleration as well as the mass and damping need to be considered in this scheme.

1.2.1.a Implicit solution method

The word 'implicit' in an implicit solution refers to the scheme by which the state of a finite element model is updated from time t_n to t_{n+1} in a time step of dt where t_n is the time at the beginning of each time step and t_{n+1} is the time at the end of each time step. An implicit method refers to the fact that the state of the model at time t_{n+1} is actually based on the information at time t_{n+1}. An implicit approach to a set of finite element equations involves iteration until a convergence criterion is satisfied for each time step increment. There are a range of solution procedures used by implicit FE solvers. The most common methods however, are a form of the Newton–Raphson method as well as Newark's method. In these methods the goal is to find the solution to an equation of the type:

$$\{F\} = [K].\{U\} \tag{1-1}$$

where $\{F\}$ is the total load matrix, $\{U\}$ is the overall displacement matrix and $[K]$ is called the stiffness matrix. Equation (1-1) is a classic representation of the relation between external forces and the displacement in a spring. This formulation is applied to all individual segments (elements) of the entire model and once assembled equation (1-1) represents an overall relation between the forces (boundary conditions) applied to the model and the resulting displacement. In order to solve for this eventual displacement we can rewrite the above equation in the following form,

$$\{U\} = [K]^{-1}.\{F\} \tag{1-2}$$

In order to solve for the displacement matrix, the stiffness matrix $[K]$ needs to be inverted. This is one of the fundamental differences between implicit and explicit solution. This is a computationally expensive operation, however the iterative nature of this method ensures that a relatively large time step can be used while achieving an accurate solution [36]. This accuracy is dictated by a convergence criterion which must be met during the solution and should be less than a certain threshold value. Most of the commercial software such as ANSYS, Nastran and Abaqus utilize an implicit method, especially for structural analysis. In the case of non-linear problems, a modified version of the Newton method is used as an alternative. However, very large deformation problems such as crash analysis and leaflet motion can result in millions of degrees of freedom, increasing the size of stiffness matrix and resulting in longer

computational time required for its inversion. This is the idea behind an alternative method (explicit solution) which does not require the inversion of the stiffness matrix.

1.2.1.b Explicit solution method

Unlike an implicit solution, the explicit method solves the state of the model at time t_{n+1} based on information available at time t_n. Derivatives of the displacement matrix (velocity and acceleration) at a particular point during a time step are considered to be constant. These values are the base line for calculations of velocity and acceleration in the next time step. The main purpose and application of the explicit method is to solve dynamic problems involving large deformations, a weak point for the implicit solutions.

In an explicit method, central difference time integration (CDTI) is used to calculate unknown variables at desired nodal points. In general, the dynamic equation that needs to be solved in an explicit solution is of the form:

$$[M]\{\ddot{U}\} + [C]\{\dot{U}\} + [K]\{U\} = \{F\} \tag{1-3}$$

Assuming known values for velocity and displacement at time t_{n-1} we can rewrite equation (1-3) as:

$$[M]\{\ddot{U}\} = \{F\} \tag{1-4}$$

And from there, acceleration matrix for time t_n would be calculated as:

$$\{\ddot{U}\} = [M]^{-1}\{F\} \tag{1-5}$$

Using the central difference time integration, velocities at time $t_{n+1/2}$ are derived:

$$\dot{U}_{n+\frac{1}{2}} = \dot{U}_{n-\frac{1}{2}} + \ddot{U}\Delta t_n \tag{1-6}$$

And from there, displacements at t_{n+1} which is the next time step can be evaluated:

$$U_{n+1} = U_n + \dot{U}_{n+\frac{1}{2}}\Delta t_{n+1/2} \tag{1-7}$$

Using the value of displacement at time t_{n+1}, the structural geometry is updated to its new location and the solution progresses to the next time step. As it can be seen in equation (1-5), in order to solve for the acceleration matrix, an inversion of the lumped mass matrix is required as opposed to that of the global stiffness matrix in the implicit methods. Since this matrix is a

diagonal matrix, its inversion is not computationally expensive and is very direct [37, 38].

However, unlike the implicit solution method, which is unconditionally stable for large time steps, the explicit scheme is stable only if the time step size is smaller than the critical time step size for the structure being simulated. This critical time step size is related to the largest natural circular frequency of the system ω_{max} and corresponds to a very small value [equation (1-8)]. This very small time step size requirement for stability thereby makes explicit solutions useful only for very short transient problems [39].

$$\Delta t_{critical} = {}^{2}/_{\omega_{max}} \tag{1-8}$$

For a shell structure this equation can be written as:

$$\Delta t_{critical} = {}^{L_c}/_{c} \tag{1-9}$$

where L_c represents the characteristic length of an element and c is the speed of sound traveling through that element. The speed at which sound travels depends on the material properties of the model and can be calculated as:

$$c = \sqrt{\frac{E}{\rho\,(1-\vartheta^2)}} \tag{1-10}$$

Where E is the Young's elastic modulus, ρ is the density and ν is the Poisson's ratio of the material. Equations (1-9) and (1-10) simply state that in order for an explicit solution to be stable, the maximum time step should be smaller than the time it would take a sound wave to travel through the smallest element of the model with a characteristic length of Lc.

1.2.2 Fluid structure interaction

In general, numerical simulations can be divided into three main categories: (1) structural analysis, (2) computational fluid dynamics and (3) fluid structure interaction. Each of these methods has its particular application and focus. Depending on the media that is being studied the implemented methodology will vary. Structural analysis is widely used to comprehend and predict the response and behaviour of a (solid) system to loads exerted on it during the life of the structure. The purpose of a structural analysis is to ensure the adequacy of the design in terms of

material properties; stress distribution; strength and buckling; fatigue and fracture; geometry and design optimization. The most common methodology used in a structural analysis is the Lagrangian method, in which the elements of the model deform under loading and therefore the material within them deforms accordingly. This means that the spatial domain (the elements) and the material domain move as one entity which is best suited for structural applications. There are countless number of applications for structural analysis in research and industry such as: automotive, aerospace, composites, civil and mechanical engineering, biomedical prosthetics and etc.

Computational fluid dynamics (CFD) is also widely used to study gas and hydrodynamics. Traditional flow analysis and design is restricted and limited in accuracy when solving and visualizing recent complicated problems and geometries. This is particularly true and more obvious in cases which are three dimensional and involve turbulence, and/or heat and mass transfer. Detailed velocity profiles, pressure gradients, temperature variations and bulk flow are few of the common field variables that can be calculated using computational fluid dynamics. Aerospace; automotive; civil, chemical and mechanical engineering; semiconductor industry; turbomachinery; steel and glass industry; and architecture are some of the areas where CFD analysis is applied. The large deformations associated with fluid movement, renders a Lagrangian method to be an unsuitable formulation for fluid dynamic analysis. Hence, the Eulerian method is commonly practiced to solve CFD problems. In this methodology, the physical mesh does not deform and instead, the material flows through this (spatial) mesh in an advection step. However, since the volume of material stored in each element varies at different time steps, these volume fractions need to be monitored and saved during the analysis [40]. This approach is proper when dealing with a geometrically fixed fluid domain however; difficulties arise when the fluid domain changes shape or when moving interfaces are present inside the domain. Typical examples of such situations are flow inside flexible tubes, vibration of a beam in the air, heart valves or a flapping flag.

In both CFD and structural analysis only one media is modeled and studied and there is no interaction between the model and its surroundings. This does not pose an issue in the case of a fluid which is in contact with a rigid structure. However when solving for a situation in which the surrounding structure is flexible and can be influenced by the fluid dynamics, neglecting the

interaction between the two media can create misleading and unrealistic results. The force exerted on the structure due to geometrical variations or pressure increase/decrease in the fluid will act as an internal/external force on the structure and lead to local displacements. This displacement in terms means a change in cross section, flow and velocity profiles along the model. Depending on the model, material properties and the amount of interface between the two media, this interaction might be neglected and either the fluid or the structure can be modeled. In more delicate situations and for more accuracy however; a third type of analysis; fluid structure interaction (FSI); is necessary to account for this interaction. Modeling the valvular structure and the moving fluid volume simultaneously is not a trivial task. In the next section, different methods which are most related to the work performed in this thesis will be discussed.

1.2.3 Various fluid-structure interaction methods

Throughout the years different techniques have been proposed for managing the interfaces of an elastic and/or moving structure embedded in a fluid such as aortic cusps. The thin leaflets undergo drastic deformations and rotational degrees of freedom within the cardiac cycle. Such large movements of the solid structure within the fluid domain introduce challenges in the Lagrangian and Eulerian formulation applications. One of the most well-known methods used in fluid structure interaction analysis is the Arbitrary Lagrangian Eulerian method (ALE). In this method the fluid and solid meshes are generally created such that mesh nodes are shared at the interface. These shared nodes are moved in a Lagrangian manner with respect to their frame of reference and their convection is accounted for by the ALE method [41, 42] as described in section 1.2.4. Having shared nodes at the interface has its advantages and disadvantages of course. The advantages include low computational cost, easy implementation and accurate results. However, since the fluid nodes follow the deformation of the structure at the interface, large translations and rotations of the solid tend to cause distortions in the fluid mesh. This affects the accuracy of the solution close to the interface which is undesirable in, for example, leaflet shear stress calculations. A solution to this problem is remeshing of the entire fluid domain or the section closest to the interface to increase mesh quality. This process of mesh generation is computationally very expensive and occurs multiple times during a computation.

As an alternative to the remeshing solution, non-conforming methods have been used in which the fluid and the solid mesh need not coincide with one another. Figure 1.18 shows a

drawing in which a sample fluid-structure interaction mesh of such sort is represented. The white elements are representative of the fluid while the blue square is a solid element. An undeformed, initial state is shown in Figure 1.18 (a), while (b) and (c) show the deformed state in an ALE and nonconforming method, respectively. In the ALE method, the surrounding fluid elements are deformed to accommodate for the structural deformation which could lead to very ill-shaped elements when dealing with large deformations. Conversely, in the non conforming formulation the need for element coaptation is eliminated which facilitates mesh creations and problems associated to large deformations.

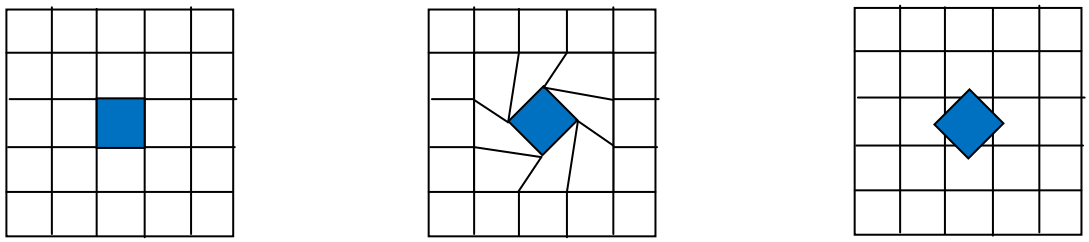

Figure 1.18: A schematic drawing of (a) a sample FSI mesh and how (b) ALE method and (c) a non-conforming method deal with the structural deformation.

Early attempts at coupling the fluid and the solid domain were accomplished by using "immersed boundary method", which was proposed by Peskin [43, 44], and an "influence coefficient" technique [45]. The immersed boundary method was based on the finite difference methodology in which the solid domain is submerged in the fluid domain without the need for a conforming mesh. In the immersed boundary condition, the coupling of the solid and fluid domains is carried out by means of an elastic law and local forces. These local forces have become the fundamental principle behind many non-conforming based FSI methodologies. The main goal of introducing these forces is to apply kinematic constraints to ensure that the nodal velocities of the solid boundary are coupled to the velocity of the fluid at that point through interpolation. However, due to the increasing interest in finite element analysis, an alternative method closely related to the immersed boundary condition, called the fictitious domain (FD) has been developed [46]. Therefore the main difference between the two methods lies in the manner in which the local forces are imposed. In the fictitious domain a Lagrange multiplier is used to constrain the solid and fluid interface. Due to the finite element nature of this method, the

Lagrange multiplier, which represents the local forces, is applied in a "distributed manner" using an integral formulation in its weak form. The kinematic constraints applied in this fully coupled method are very similar to that of the immersed boundary method:

$$\int_{\gamma} \vec{\lambda} . \left(\overrightarrow{v_f} - \overrightarrow{v_s}\right) d\gamma \tag{1-11}$$

where $\vec{\lambda}$ represents the body force exerted on the fluid and structure interface "γ" and "f" and "s" denote fluid and structural domains, respectively. The suitable application of this method for thin structures was first introduced by Baaijens [47]. This method has effectively been used in simulation of heart valves throughout the years [48, 49].

However due to the interpolation required near the solid interface to account for the fluid-solid interaction, the accuracy of the solution at this location is compromised. In many applications this issue might be negligible and solutions very close to this interface may not be required. Since this is a similar issue with ALE methods (due to mesh distortion) as well, a secondary alternative solution was proposed by Van Loon et al. [50]. This method is a combination of the fictitious domain and the ALE method and takes advantage of the non-conforming mesh requirements of the fictitious domain while an additional ALE step allows a local adaptive meshing of the fluid domain [51]. This adaptive meshing algorithm either allows for elements addition near the interface or element deformation to increase the local accuracy and mesh quality.

1.2.4 Arbitrary Lagrangian-Eulerian method

The most commonly implemented method in fluid-structure interaction analysis is the arbitrary Lagrangian-Eulerian (ALE). There are many different forms of ALE procedures such as: Operator split, unsplit finite element, finite difference advection method, interface tracking, momentum advection, coupled finite element calculation, remapping and rezoning and mixture theory. These procedures are all different in terms of the governing equations, describing the motion of the fluid domain, and also how the domain configuration is managed. The fundamentals however, are similar despite the methodology used. This includes the coordinate reference systems introduced in an ALE methodology which provide this procedure with its capabilities in dealing with large deformations. There are generally three independent coordinate

systems in an ALE formulation which aid in identification of nodes (points) in the continuum: the spatial reference (SR), the material reference (MR) and the computational reference (CR). The spatial reference is fixed and represents the Eulerian aspect of the ALE formulation while the material reference deforms with the material according to a Lagrangian formulation. The computational reference is an additional reference to the traditional Lagrangian and Eulerian references which can move arbitrarily in the continuum. The material and the spatial references describe the field quantities in the governing equations of the structural and fluid domain, respectively. However, these quantities for an ALE formulation are described in the computational reference and therefore the material and computational references need to be associated with one another. This relation can be achieved by calculating the time derivative of the change in the sample state variable (physical quantity) $\Psi\ (\vec{x}, t)$ at point N (with respect to the material reference) in the material and computational references. The change in the state variable is assumed to occur in an infinitesimally small time step of Δt.

The time derivative of state variable $\Psi\ (\vec{x}, t)$ in the material reference can be written as:

$$D\Psi/Dt = \lim_{\Delta t \to 0} 1/\Delta t\,[\ \Psi(\vec{x} + d\vec{x}, t + \Delta t) - \Psi(\vec{x}, t)] \tag{1-12}$$

$$D\Psi/Dt = \lim_{\Delta t \to 0} 1/\Delta t\,[\ \Psi(\vec{x} + d\vec{x}, t + \Delta t) - \Psi(\vec{x}, t) - \Psi(\vec{x}, t + \Delta t) + \Psi(\vec{x}, t + \Delta t)] \tag{1-13}$$

Replacing "$\Psi(\vec{x} + d\vec{x}, t + \Delta t) - \Psi(\vec{x}, t + \Delta t)$" by "$d\vec{x} \,.\, (\nabla \Psi)$" will give:

$$D\Psi/Dt = \lim_{\Delta t \to 0} 1/\Delta t\,[\ d\vec{x} \,.\, (\nabla \Psi) + \Psi(\vec{x}, t + \Delta t) - \Psi(\vec{x}, t)] \tag{1-14}$$

$$D\Psi/Dt = \vec{\vartheta} \,.\, (\nabla \Psi) + \partial\Psi/\partial t\Big|_{\vec{x}} \tag{1-15}$$

where ν is the velocity of point N with respect to the material reference. Interpretation of equation (1-15) would simply be: the variation of a state variable for a given point N, is the local variation plus the convective term (which accounts for the relative displacement between the material and computational reference). A similar equation can be derived for the time derivative of the state variable with respect to the computational domain:

$$D\Psi/Dt = (\vec{\vartheta} - \vec{\omega}).(\nabla\Psi) + \partial\Psi/\partial t\Big|_{\vec{u}} \quad (1\text{-}16)$$

where ω represents the relative velocity between the material and the computational references; and u is the position of point N with respect to the computational reference.

In the same manner, the ALE differential form of the conservation equations for mass, momentum and energy are derived form their Eulerian forms:

$$\frac{D\rho}{Dt} = \rho\vec{\nabla}.\vec{\vartheta} \quad \text{Mass} \quad (1\text{-}17)$$

$$\rho\frac{D\vartheta}{Dt} = \vec{\nabla}.\sigma + \rho\vec{b} \quad \text{Momentum} \quad (1\text{-}18)$$

$$\rho\frac{DE}{Dt} = \vec{\nabla}.\left(\sigma.\vec{\vartheta}\right) + \vec{\vartheta}.\rho\vec{b} \quad \text{Total energy} \quad (1\text{-}19)$$

$$\rho\frac{De}{Dt} = \sigma : 1/2(\nabla\vartheta + \nabla^T\vartheta) \quad \text{Internal energy} \quad (1\text{-}20)$$

where ρ is the density, σ is the Cauchy stress tensor, ν denotes the material velocity vector, E is the specific total energy, b is the specific body force and e represents the specific internal energy. Note that $\sigma : 1/2(\nabla\vartheta + \nabla^T\vartheta)$ represents the Frobenius inner product of the Cauchy stress tensor and the strain rate tensor.

By substituting equation (1-16) into the above equations, the ALE form of the conservation equations is obtained:

$$\frac{\partial\rho}{\partial t} + (v - \omega).\nabla\rho = \rho\vec{\nabla}.\vec{\vartheta} \quad \text{Mass} \quad (1\text{-}21)$$

$$\rho\frac{\partial\vartheta}{\partial t} + \rho\,(v - \omega).\nabla\vartheta = \vec{\nabla}.\sigma + \rho\vec{b} \quad \text{Momentum} \quad (1\text{-}22)$$

$$\rho\frac{\partial E}{\partial t} + (v - \omega).\nabla\mathrm{E} = \vec{\nabla}.\left(\sigma.\vec{\vartheta}\right) + \vec{\vartheta}.\rho\vec{b} \quad \text{total energy} \quad (1\text{-}23)$$

$$\rho\frac{\partial e}{\partial t} + (v - \omega).\nabla e = \sigma : 1/2(\nabla\vartheta + \nabla^T\vartheta) \quad \text{Internal energy} \quad (1\text{-}24)$$

which can basically be derived by replacing the material velocity ν, by the convective velocity (ν - ω).

In the case of an incompressible material where ρ is considered to be constant, equation (1-21) will result in:

$$\nabla . \vartheta = 0 \tag{1-25}$$

Also, substituting the Cauchy stress tensor in the momentum equation (1-22) by the constitutive equation defined as:

$$\sigma = -p\, I + 2\eta\, D \tag{1-26}$$

will result in the Navier-Stokes formulation of ALE method:

$$\rho \frac{\partial \vartheta}{\partial t} + \rho\,(v - \omega).\nabla\vartheta = -\vec{\nabla}\, p + \vec{\nabla}.\, 2\eta\, D + \rho\vec{b} \tag{1-27}$$

This means that the Eulerian and the ALE form of the Navier–Stokes equation are equivalent (assuming ω to be zero), except for the fact that $\frac{\partial \vartheta}{\partial t}$ is defined in respect to the computational reference.

1.2.5 Overview of LS-DYNA

Commercial finite element analysis (FEA) software, capable of fluid structure interaction, have been implemented by researchers utilizing the aforementioned numerical methods [52-57]. LS-DYNA (LSTC, Livermore, CA, USA) is one of the most commonly used software for FSI simulations. It is an explicit software which employs the ALE method to couple the fluid and the solid domains and also to perform fluid mesh refinement near the structure due to large deformations and distorted topology. LS-DYNA belongs to a class of hydrocodes which use an "operator split" approach to solve the governing equations of the Lagrangian and Eulerian domains. This method is discussed in section 1.2.5.b.

1.2.5.a Hydrocode modeling

Hydrocodes are computational tools for modeling the behaviour of a continuous domain. Due to restricted memory allocations of a computer, hydrocodes can analyze the desired domain only by dividing it into smaller and more manageable sections called elements; a process known as discretization. Assembly of all the elements together defines a "mesh" which approximates the geometry of the model. This approximation approaches the exact representation as the discretization level increases and the elements sizes become finer. Hydrocodes in general rely on three principles to define the amount of forces applied to the elements at each time step: Newton's laws of motion, the equation of state and the constitutive laws. Newtonian laws represent the principles of conservation of mass, momentum and energy while the equation of state relates pressure to the density and internal energy [$p = f(\rho, I)$] and the constitutive model relates the stress to strain and internal energy. In the case of complex problems and geometries numerous equations must be solved simultaneously to calculate the desired field variables (physical quantities) involved. Numerical simulations are therefore the sole method of refuge which could solve for so many parameters required in the solution. As such, hydrocodes are frequently applied to problems that involve large deformations, large stretches, and turbulent flow as well as problems that deal with element inversion or creation of new surfaces. In all these cases, a new mesh needs to be created to replace the distorted topology and the old solution needs to be "mapped" or "advected" to the new mesh. These advection algorithms are generally second order and are used to calculate material transport between elements [58].

In the remainder of this section, the operator split method will be discussed due to its popularity, its use in LS-DYNA and also the fact that it has been used in the work presented in this thesis. The main reason for the popularity of this method relies on the simplicity to achieve second order accuracy in explicit solution by centering the solution variables.

1.2.5.b The operator split formulation

Operator splitting is a suitable method for transforming complex problems into a series of less complicated problems. One such application is the separation of the Lagrangian and Eulerian parts of an ALE calculation. As mentioned before, the mesh used in Eulerian formulation is fixed in the spatial reference. Eulerian formulations trace for element deformation due to the

Lagrangian deformation as well as material transport through out the mesh. One approach employed by Eulerian codes to achieve this, is by separating these terms in two steps. First, a Lagrangian step is performed in which the mesh distorts with the material. Second, the solution from this distorted mesh is mapped back onto the computational reference, which moves arbitrary in space and is independent of the material and spatial references. This step is usually referred to as the "advection", "remap", or "Eulerian" step. These steps are schematically represented for a Lagrangian, Eulerian and ALE formulation in Figure 1.19 below.

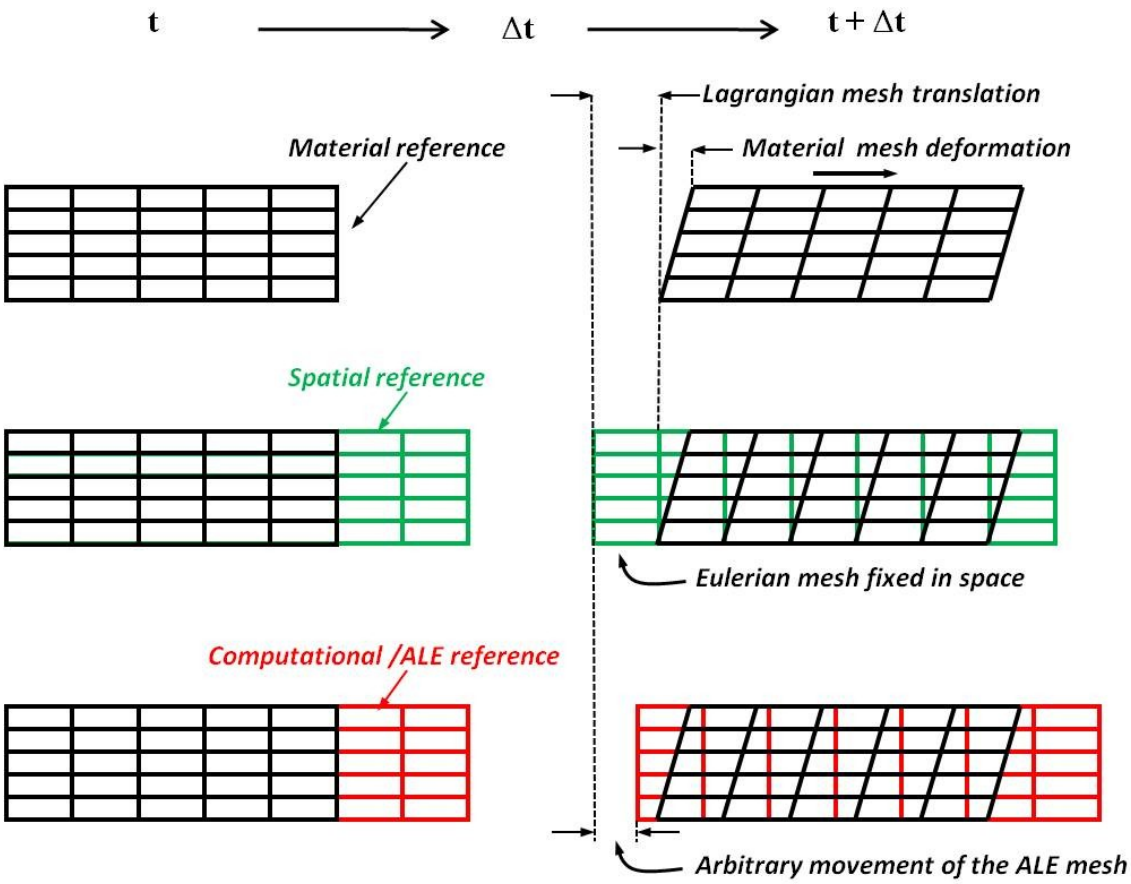

Figure 1.19: Schematic drawing representing the deformation and translation of Lagrangian vs Eulerian vs ALE meshes.

Note that the difference between the Eulerian and the ALE formulation is the arbitrary movement of the background mesh and hence the different amount of material being transferred between elements. The operator split method can be illustrated using the equilibrium equations for the Lagrangian phase presented in equations (1-18) and (1-19). In the advection or transport

phase, the transportation of mass, momentum and energy across element boundaries are computed using the transport equations:

$$\frac{\partial \Psi}{\partial t} + (\vec{v} - \vec{\omega}).\nabla(\Psi) = 0$$
$$\Psi(\vec{x}, 0) = \Psi_0(x) \tag{1-28}$$

The steps performed in the advection algorithm of an operator splitting ALE calculation are as follows:

- A Lagrangian step is performed to advance the solution
- This solution is remapped onto the new ALE mesh in an advection step using the following subsets
  - Mesh smoothing algorithms are used to create a more relaxed mesh.
  - The element-centered variables are mapped and transported.
  - The node-centered momentum are mapped and transported.

As it can be observed from Figure 1.19, both Eulerian and ALE formulations can contain more that one material in a single element on the contrary to Lagrangian elements which always contain one material within them. Such elements are referred to as "multi material" elements and due to the complexities associated with handling multiple materials, they are computationally expensive. Therefore, the "single material" formulation of such elements are used in "simplified ALE" codes which in most cases provide little advantage over the purely Lagrangian elements.

1.2.5.c Lagrangian-Eulerian coupling

Any numerical simulation which involves more than one media requires specific algorithms to cope with the intersecting region where these media come in contact with one another. If two Lagrangian media overlap and collide with each other it is referred to as "contact". However, if a Lagrangian media collides with an Eulerian/ALE media, the definition of their interaction is referred to as "coupling". Generally in a FSI problem, the structure is immersed in the fluid domain and as time progresses in the simulation the material interface

location changes. In order to track this interface in elements, the Young's method is used in which the material layout is described solely by the volume fraction of the fluid material in the element. This method is described in detail in [59].

At any given time step, nodal force calculation is the main part of the explicit time integration process. These forces are computed at the structural and fluid nodes as well as nodes situated at the interface area. The nodes at the interface play an important role in definition of the coupling algorithm and can be divided in two categories: The "slave nodes", belonging to the structural domain and the "master nodes" which belong to the fluid domain. The code constantly searches for a penetration along the interface by calculating the relative velocity ($v_s - v_f$) at each time step using the central difference scheme:

$$\vec{d}^{n+1} = \vec{d}^{n} + \left(\vec{v}_s^{\,n+\frac{1}{2}} - \vec{v}_f^{\,n+\frac{1}{2}}\right).\Delta t \tag{1-29}$$

where d is the penetration depth representing the amount by which the coupling constraint is violated as described in Figure 1.20.

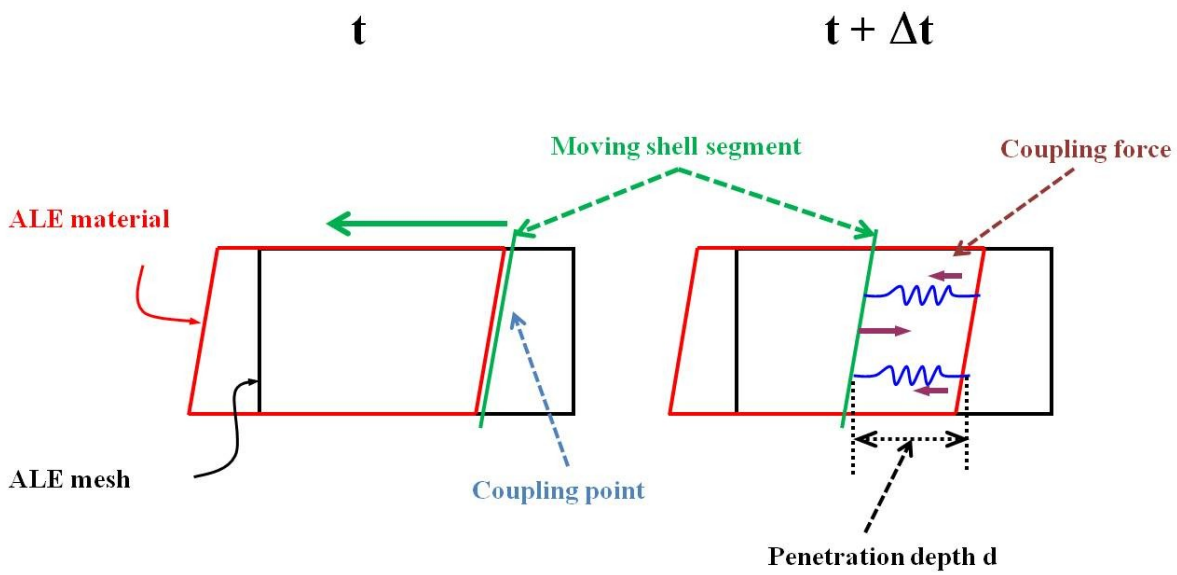

Figure 1.20: A drawing representing the penalty base coupling between Lagrangian and ALE material

The slave node is a Lagrangian mesh node, whereas the master node is not necessarily an Eulerian mesh node. Due to the non-conforming nature of ALE approach in LS-DYNA this node

can be considered to be a fluid particle within a fluid element. Its mass and velocity can be interpolated from the fluid element nodes using element shape functions [60].

The coupling force acts only if $\vec{n}_s \,.\, \vec{d}^n < 0$ which is representative of a penetration. $\vec{n}_s$ is the average normal of all the structural elements connected to the discussed structural node. The coupling method used in LS-DYNA is referred to as a "penalty base" approach which roots in the fact that the coupling force is proportionally related to the penetration depth. This is achieved by means of a stiffness coefficient similar to the fundamental spring stiffness (F = K . X). This force can be directly applied to the Lagrangian node, however for the ALE domain this force is distributed to the fluid nodes based on element shape functions [61].

1.2.6 A brief history of aortic valve simulations

Two common challenges are associated with modeling valvular biomechanics: (1) dealing with the large deformations associated with the leaflets dynamics and (2) the ability of the model to provide proper contact between moving structural components of the FSI model. The latter is critical in terms of leaflet coaptation and avoiding backflow scenarios. The evolution of heart valve simulations has followed a path similar to the general advancements in the FSI domain. The initial efforts to model the interaction of the fluid and solid were made using immersed boundary methods [62]. Chew et al. [63] were one of the pioneers of FSI in the aortic valve modeling. They created a three dimensional model of a bioprosthetic porcine valve with non-linear material properties and also included the collagen fibers. Almost a year after, De Hart implemented a user-defined fictitious domain approach to create a 2D model of the aortic valve [48] which was later expanded to a three dimensional study [49]. In these studies, the root structure was coupled to the fluid using an ALE approach, while the leaflets were treated using FD method. Even though results from these simulations were qualitatively and quantitatively comparable to previous experimental and numerical studies; due to reduced accuracy near the leaflets inherent to fictitious domain methodology, leaflet contact (coaptation) was not properly achieved. One sixth of the geometry was modeled and low Reynolds numbers were used at the inlet to avoid instability. Utilizing the same three dimensional model, specific variations to geometry and material properties of the valve were explored. At first, a fiber-reinforced model of the leaflets was investigated [64] and results of the model in terms of stresses and dynamic

behaviour were analysed. Inclusion of collagen fiber distribution was the next step in the research done by this group which revealed variations in the stress values experienced by the leaflets [65].

Nicosia et al. [52] conveyed a study of an asymmetric aortic valve using the commercial software LS-DYNA. Linear elastic material properties were used for the aortic root while leaflets were modeled as non-linear. Transvalvular pressure difference, difference between ventricular pressure and aortic pressure, were applied at the inlet of their model, which varied through the cardiac cycle. This pressure however had to be scaled down to avoid element distortion. The opening phase of the valve was modeled by Howard et al. [66] in an explicit dynamics analysis. Different pressure patterns which varied linearly were imposed on base, sinus and leaflet of the model. Gnyaneshwar et al. [67] and Sripathi et al. [68] quantified stress and displacements over the cardiac cycle using transvalvular pressure on the leaflet surfaces. The pressure curves used by Sripathi were more physiological and less linear compared to the one used by Gnyaneshwar.

In general, the boundary condition applied at the inlet of the valve is pressure. Carmody et al. [53] however, used the inflow data obtained from a secondary model of the ventricle to implement a fluid-structure interaction model of the aortic valve. This model was used to mimic the physiological contractions and relaxations of the ventricle and obtain the resulting velocity profiles at the ventricular outlet and use it as the inlet of aortic model. The advantage of this approach is that it avoids the common assumption of parabolic inlet velocity profiles. The results revealed that the pressure gradient across the valve is rotationally symmetric and the flow exiting the ventricle is mainly axial. It was shown that the use of spatially uniform pressure as the inlet condition is acceptable but needs to be temporally variable to represent the physiological variations during a cardiac cycle. A multiscale FSI model of the aortic valve was developed by Weinberg [69] which implemented non-linear, anisotropic material properties. Cellular, tissue and organ levels were investigated to shed some light on the anisotropic strains experienced by the leaflets during a cardiac cycle. The same model was later used to investigate and compare bicuspid and tricuspid valves using transvalvular pressure as the boundary condition at the aortic inlet level [55]. Labrosse et al. and Beller et al. focused more on the clinical aspect of the research and assessed the role of aortic root motion in natural operation of the valve [70-72]. On the same path, Katayama investigated the role of sinus of Valsalva in the dynamic behaviour of

the aortic valve. Aortic valves with and without the sinuses were modeled in a FSI simulation and the results suggested a more rapid and a longer opening time in the model without the sinuses [73]. Weinberg et al. later used the same model described before to study the impact of aging and calcification on leaflet dynamics using LS-DYNA [54]. Increased shell thickness and stiffness was used to simulate the aging and the calcification process.

In order to illustrate how three dimensional heart valve simulations can aid in assessing the degree of stenosis, Van loon investigated a variety of shapes and stiffness distributions of aortic leaflets in an FSI analysis [74]. The fictitious domain method was used for the leaflet-blood interactions using the SEPRAN package. Leaflets were considered to be Neo-Hookean and clinically relevant scenarios such as leaflet fusion or calcification, and variable stroke volumes were implemented. Since this study was in its early stage of development, no clinical conclusions were drawn and the results were solely used to demonstrate the capabilities of FSI models to assess aortic stenosis. Kim et al. [75, 76] on the other hand developed a method that predicts coronary flow and pressure of three-dimensional epicardial coronary arteries. For each coronary outlet, a lumped parameter coronary vascular bed model has been assigned to represent the impedance of the downstream coronary vascular networks. This FSI model of the aortic root however, neither includes the aortic leaflets nor the sinus structure which does not allow them to investigate pathologies of this region as a global entity. Excluding the natural leaflets of the aortic valve also eliminates the complexity and challenges associated with modeling their large deformation during a cardiac cycle in an FSI study.

In this work we have developed three models of the aortic valve region based on the earlier versions developed by our group [56, 57, 77]. These are all three dimensional and fluid-structure interaction models. The first model, which serves as the base for the following two models, is the “normal aortic model” in which the two coronary ostia have been included. The goal of such a model is to integrate the flow in the coronary ostia in the previously developed FSI model by our group, to investigate the effect of pathologies on coronary perfusion. In some pathological conditions such as diabetes [78, 79], hyperglycemia, hyperinsulinemia, and impaired glucose tolerance [80, 81], the microstructure of the aortic root and the aortic valve leaflets is altered resulting in changes in tissue thickness, stiffness, or both [82, 83]. This leads to pathological conditions explained in Chapter 1, such as aortic stiffening and calcific aortic

stenosis. Aging of the aortic valve (AV) which is characterized by cuspal thickening [84] and loss of extensibility[85], can also lead to progressive changes in AV function. These pathologies are thought to affect coronary blood flow [86, 87]. Reduced aortic distensibility results in a decrease of diastolic backflow that aids coronary perfusion, disturbing thus the oxygen demand/supply balance of the myocardium [88]. Inclusion of the coronary ostia will allow us to obtain hemodynamic variables related to coronary arteries such as perfusion level in normal as well as pathological cases. Such a model enables us to link prophylactic treatments such as smoking cessation, exercise, or diet to variations in coronary perfusion.

The "normal aortic valve model" however, exclusively allows studying coronary flow and not the effect that these pathologies could have downstream in the coronary arteries on velocity distribution or shear stress. A more global model which includes the coronary structures could better aid in investigating and further understanding the underlying behavior leading to coronary artery disease. Therefore in order to explore this inter-relation, as a next step, a "global model of the aortic valve" was created. Since degenerative diseases of cardiac tissue causes thickening and stiffening of this vasculature [89], the impact of different degrees of aortic sclerosis on the coronary hemodynamics was investigated using a variety of thicknesses and stiffnesses for the cardiac tissue. This would not be possible with the previously established FSI models of the aortic valve which do not incorporate the coronary artery structures. Finally, the third model of the aortic valve investigated in this thesis involves exploring the possible mutual effect that coronary and aortic pathologies might impose on each other. This notion of global pathology has been examined by incorporating and introducing different degrees of stenosis into the coronary arteries in a "pathological global model of the aortic valve". Possible variations in valvular dynamics, stress distribution or commissural expansion would indicate such mutual impact and would point towards a more rapid progression and a more global pathology.

In order to better clarify the stand point of the work presented in this thesis relative to the most recent numerical modeling work performed by other research groups, Table 3-2 has been presented below which shows a brief comparison between these studies and our work. It can be observed at a glance that our model is the only global, real three dimensional model of the aortic valve region which includes the natural leaflets, sinuses of Valsalva and coronary arteries (including their geometric features such as curvature).

Table 1-1: Comparison between our model and recent numerical models of the aortic valve region

Inclusions / Teams	FSI	Real 3D	Sinus Structures	Natural Leaflets	Coronary Arteries	Pathology Investigation	Non-linear Material Properties	Multi-layer Tissue	Global Model
Nobari et al.	✓	✓	✓	✓	✓	✓			✓
Van Loon	✓	✓	✓	✓		✓			
Kim et al.	✓	✓			✓	✓			
Weinberg et al.	✓	✓	✓	✓		✓	✓	✓	
Carmody et al.	✓	✓	✓	✓			✓		
DeHart et al.	✓		✓	✓			✓		

The numerical models of the groups presented in Table 1-1 for comparison purposes are all considered to be of great value and abide by the highest standards of recent fluid-structure interaction simulations of the aortic valve. They are also the most similar to the work presented in this thesis. Therefore, works performed by other research groups that is either structural or CFD has not been mentioned here since they do not follow the same methodology and do not deal with similar convergence issues and instabilities associated with FSI models of the aortic valve. All of these groups have incorporated real three dimensional geometries except for the work by DeHart et al. in which only one sixth of the geometry was modeled. However, the geometry used in this work is based not only on previously published work but also from imaging techniques such as MRI and CT scan. The aortic root, sinuses of Valsalva, the natural leaflets and the aortic wall have been included in the geometries of these works except for the work performed by Kim et. al. in which the sinuses and the leaflets have not been included. The inclusion of the leaflets is of great importance and one of the most challenging portions of modeling this delicate region. The large deformation associated with the leaflets during the systolic and diastolic phases introduces a challenging task of overcoming instability and convergence issues as well as having to deal with proper contact definition between the cusps during the closing phase of these anatomical features. Even though Kim et al. have not included these structures in their work, they have instead modeled a detailed branching of the coronary arteries in their work. Therefore, our global model and the work by Kim et al. are the only ones which have included the coronary arteries in their aortic valve model.

On the other hand, Weinberg et al. are the only group, which have implemented the three different layers of leaflet structure into their study while considering non-linear material properties for the tissue. The non-linearity of the cardiac tissue has been explored by Carmody and DeHart as well, but has been replaced by linear material models by other groups including this work. This is due to the immense increase in the computation time and instabilities introduced in the model by considering this non-linearity. This has been further discussed in the next chapter as well as in the limitations section.

Due to clinical interest, pathologies have been investigated in the more recent studies to explore their impact on hemodynamics and dynamics of the cardiac tissue. However, the model presented in this thesis is different from all these recent works in the sense that the inclusion of the coronary arteries introduces the notion of "globality" into the model. While the work by Kim et al. takes advantage of very detailed and complex boundary condition application and a larger portion of the coronary arteries, the exclusion of the aortic leaflets and sinuses does not allow them to explore the possible link between the coronary arteries and the aortic leaflets. The introduction of the notion of "globality" into the model is of great importance since it allows investigating the impact of *regional* pathologies on the *global* anatomy, as compared to a small section of the cardiovascular system. Our model is different from all the other works presented here, since it enables us to investigate the possibility of an inter-relation between the aortic valve and the nearby structures as a *"global entity"*.

Chapter 2 : Computational model

The process of creating a numerical model, despite the solution method used, can generally be subdivided into four individual steps:

- Creation of a computer aided design (CAD) representation of the structure.
- Finite element mesh discretization
- Assigning material properties
- Applying the corresponding boundary conditions (pressure, velocity, load, contact and coupling ...).

The following sections of this chapter include detailed explanations regarding the necessary steps in the creation of the FSI model of the aortic valve studied in this thesis, the addition of the coronary arteries as well as coronary stenosis.

2.1 The normal aortic model

2.1.1 The geometry

The geometric model of the cardiac structures was created using a parametric representation of the aortic root. Having a parametric model allows for future modifications that are generally less time consuming and more automated. Our model was created by using circular cross sections at different heights along the axis of the aortic valve. Each of these circles corresponds to a certain key location in the aortic valve including: the annulus, sinus of Valsalva, commissures, sinotubular junction, and the ascending aorta. However, the heights at which these key locations are situated and their corresponding diameters vary depending on many parameters amongst which some of the most obvious are: health condition, age, gender, height and weight. Therefore, average values need to be used to recreate an average anatomy of the structure. The values used in our research are all normalized to the diameter of the aortic root annulus as a reference value which is considered to be 23 mm [90]. These values were obtained from previous ex-vivo measurement performed by several research groups and are presented in Table 2-1 below.

Table 2-1: Normalized values of height and diameter at certain key locations obtained from previous studies to create the aortic valve model.

Research Group	Year	D_{sinus}	H_{sinus}	$D_{commiss}$	$H_{commiss}$	$H_{coaptation}$	D_{STJ}	H_{STJ}	D_{aorta}	H_{aorta}
Lozsadi et al.	1969	1.26		0.86	0.78		1.00	0.87		
Sands et al.	1969	1.12								
Reid et al.	1970				0.67					
Mercer et al.	1973	1.70					0.75	1.01		
Swanson et al.	1974	1.46		1.07	0.71		1.00	0.88		
Thubrikar	1990	1.49		0.89	0.77			0.91		
Mercer et al.	1992			1.17			1.10			
Kunzelman et al.	1994		0.40			0.54	0.81	1.20	0.91	2.00
Choo et al.	1999						1.03	0.98		
Berdajs et al.	2002			0.90			0.95	0.83		
Our Model		**1.41**	**0.40**	**0.96**	**0.73**	**0.54**	**0.95**	**0.95**	**0.91**	**2.00**

The CAD representation of our aortic root model was initiated by modeling one third of the structure and then mirroring it across its two planes of symmetry. Using the average values for heights and diameters, the aortic wall was constructed but did not include the sinuses. The sinus and leaflet structures, obtained from 3D digitization, were later added to this initial aortic wall to create the final 3D model of the aortic root [57, 77]. Pro/Engineer 2006 CAD software was used to perform all geometry creation tasks.

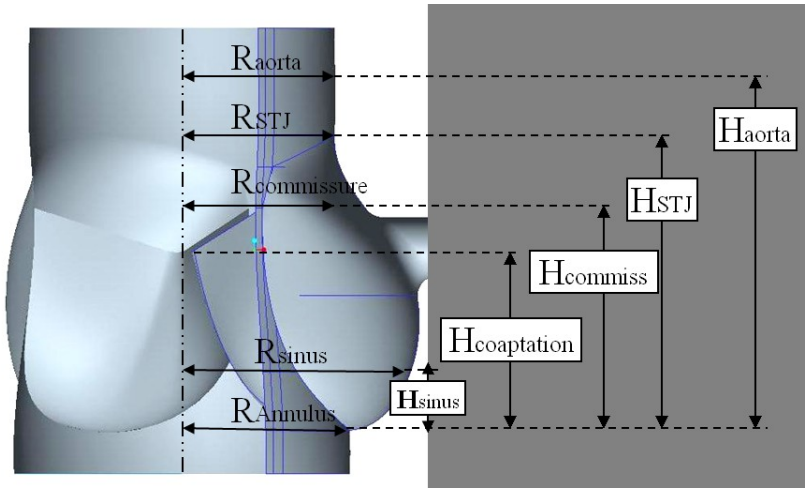

Figure 2.1: Parametric representation of the aortic valve model

Figure 2.1 above shows the parametric model of the aortic valve created using the values from Table 2-1 at the corresponding key locations while Figure 2.2 below shows different views of the CAD file created using Pro/Engineer.

(a) (b)

Figure 2.2: (a) axial, and (b) side view of the aortic valve model

The coronary ostia were located on two of the sinuses with a diameter of 3 mm while the center of the outlet orifice was placed at the commissural level [90]. In some surgical procedures however, such as the remodelling or the re-implantation procedures, coronary arteries will be removed from the sinuses. As explained in chapter 1, these arteries need to be sutured back onto the Dacron graft through an opening created by the surgeon. Since one of the objectives of this work revolves around the clinical applications of this model, different heights of ostia were modeled as shown in Figure 2.3. This allows studying the possible impact that ostia positioning might have on local hemodynamic such as flow due to congenital diseases or surgical procedures.

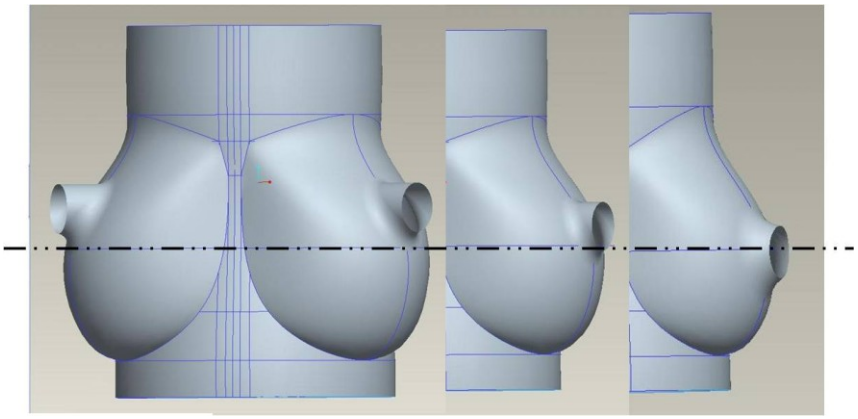

Figure 2.3: Side view of aortic valve CAD models representing different heights of ostia location due to possible congenital disease or surgical procedures

2.1.2 Finite element model

The first step after creating the geometry is to import it into a preprocessing software to divide it into separate parts, or in our case surfaces, in order to create a proper mesh. Hypermesh from Altair Hyperworks was used to perform all the meshing procedures. The CAD geometry was imported into this software using an IGES format and a tolerance of 0.001 mm. Hypermesh was used due to its capability for creating high quality mesh, its compatibility to import and export various file extensions and its wide collection of element formulations.

Due to the FSI nature of this study the mesh creation involves two steps:

- Creating a structural mesh representative of the cardiac tissue
- Creating a fluid mesh representing the blood

The details regarding element selection and mesh creation in these two steps will be discussed in the following sections.

2.1.2.a The structural/Lagrangian domain

The geometry of the aortic valve was divided into three sections for simplifying material property and boundary condition specification as well as achieving a high quality mesh. There is no discontinuity between these parts and the connecting nodes are shared between the two adjacent parts.

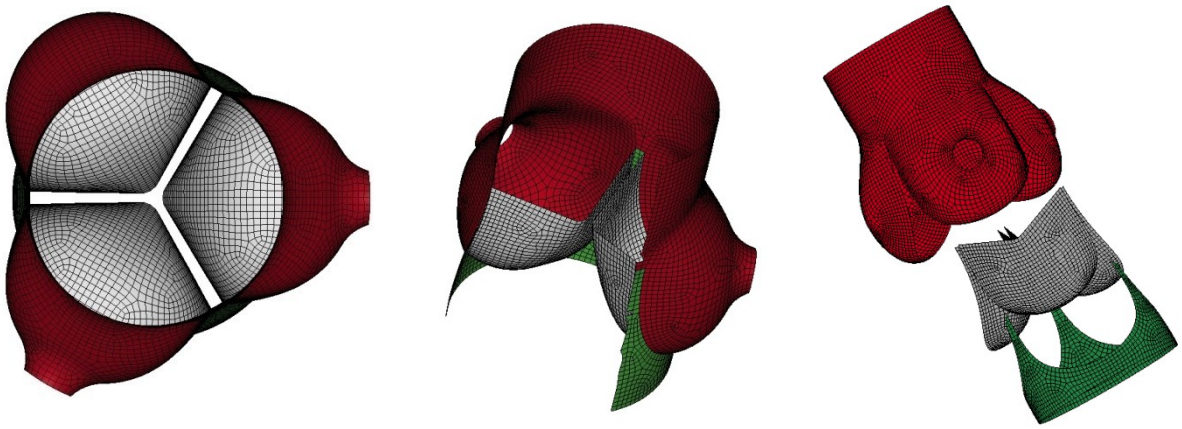

(a) (b) (c)

Figure 2.4: Different views of the final structural mesh from (a) top view, (b) cut view, and (c) exploded view.

The structural domain consists of thin shell elements. These elements were chosen over solid elements due to their superior capability to model bending as well as accounting for in plane and normal loads. Effort was made to assure having quadrilateral elements in the entire structural domain due to their Belytschko-Tsay formulation used by LS-DYNA. These elements are well suited for modeling large deformations and have 12 degrees of freedom at each node: translations, accelerations, and velocities in the nodal x, y, and z directions and rotations about the nodal x, y, and z-axes. The elements of the structural domain cannot be too fine similar to what is common practice in structural analysis. This is related to the limitations associated with the FSI calculations. A certain ratio needs to be maintained between the structural and fluid elements in order to achieve convergence and reduce computational costs. In a complex simulation such as this model, computational times increase tremendously with an increase in the number of elements in a non-linear fashion. However, in order to achieve the minimum allowable element size and to assure convergence, mesh independency tests were undertaken and it was observed that 12,653 quadrilateral shell elements is adequate for comprising the structural domain.

2.1.2.b The Fluid/ALE domain

Similar to the structural domain, the fluid domain consists of several parts including: an inlet (the ventricular outlet), the main fluid, and the outlet (inlet into the aorta). These parts are also, created solely to aid in boundary condition application and do not have any inconsistency amongst them. Figure 2.5 (a) shows an exploded view of the fluid domain, while Figure 2.5 (b) shows the overall fluid structure interaction model. As it can be seen, the structural domain is completely submerged in the ALE domain which is common practice in FSI modeling of the aortic valve [53-55, 57, 69, 91]. The portion inside of the structural domain represents the blood flowing through the aortic valve, while the portion outside accounts for the pericardial fluid surrounding the structure.

Solid hexahedron elements were used to model the fluid domain with a “1-point ALE multi material” formulation in the LS-DYNA environment. These elements are well suited for the applicable constitutive equations of the ALE formulation and can accommodate multiple

materials in one element. In the re-meshing step of the ALE formulation however, the deformed elements at the interface are replaced with tetrahedrons. This increases the local mesh quality while maintaining the overall accuracy of the solution at that time step. Even though a low percentage of tetrahedron elements could be used in the ALE domain, in order to avoid convergence problems, only hexahedron elements were used.

(a) (b)

Figure 2.5: (a) an exploded view of the fluid domain, and (b) the final FSI model the aortic valve showing the submerged structural domain in the fluid domain

The fluid medium consists of 26,743 hexahedron elements, which was found to be an adequate mesh density after doing mesh refinements and mesh independency tests by increasing node numbers up to twice their initial value. The percent differences in obtained results from the different mesh densities using a point-to-point Euclidean norm were less than 2.78%.

2.2 Global model of the aortic valve: Addition of coronary artery structures

Throughout the years there has been countless number of studies performed on either the aortic valve or the coronary structures. Studies of the aortic valve generally involve but are not limited to: prosthetic designs such as mechanical/bio-prosthetic valves, investigating different surgical procedures as well as the impact of material properties and/or pathologies. These studies as mentioned in Section 1.2 have evolved from 2D structural analysis to 3D fluid structure interaction models which can closely simulate the local dynamic and hemodynamic behaviors of this region. Similar pattern of improvement can be observed in numerical studies involving the coronary structures. Some of the most common investigations in this area involve studying: stent design and material property optimization, plaque buildup and rupture, surgical treatment procedures, drug delivery and impact of pathologies such as coronary stenosis or atherosclerosis on flow patterns.

However, there are very few studies that have incorporated both of these neighboring structures into one numerical model [92-96]. Conveyed studies in this area either have neglected modeling the natural valve structure, resorted to a simplified geometry of aortic valve and coronary structures or simply ignored the interaction between the fluid and the structural domain. De Tullio et al. have recently modeled prosthetic valves inside a simplified geometry of the sinuses using FSI simulations [92, 94, 95]. Verhey et al. studied the impact of coronary artery outlet angle variation in artificial aortic root prosthesis in a CFD simulations [93], however they have not included the leaflets in the model. Garcia et el. developed a mathematical model of the aortic valve[96], while Gaillard et al. used an in-vitro version of the same model to study the impact of stenosis on coronary flow reserve [97].

Therefore there is an obvious need for a global fluid structure interaction model of the aortic valve that houses the natural cusps and also includes the coronary artery structure to investigate the natural behaviour of this region. Creating such complex model however, is a very demanding and complicated task. This is due to the large deformations that the leaflets undergo during a cardiac cycle and the associated coupling and contact complications explained in Section 1.2. The expansion of the fluid mesh is also a daunting task and since the structural domain is submerged in the fluid mesh, this expansion is correlated to an exponential increase in

the required computational time. The next section in this chapter is dedicated to the inclusion of the coronary arteries in our 3D FSI model of the aortic valve.

2.2.1 Coronary artery geometry

The CAD representation of the coronary arteries was based on aortic computer tomography (CT) scan images provided by Montreal heart institute. 3D-DOCTOR software was used to create a wireframe representation of the arteries while Pro/Engineer was used as the CAD generator software by importing this wireframe structure and performing "lofting" and "smoothing" operations. The natural tapering of the coronary arteries was removed by maintaining a constant cross section of 3 mm along the physiological curvature of these structures obtained from MRI. The tissue thickness was considered to be 0.5 mm for both of these arteries. This simplification was made to avoid future convergence problems due to element ratio mismatch between the fluid and the structure. Figure 2.6 shows the CAD representation of these arteries before the applied simplifications in their geometry.

(a) (b)

Figure 2.6: Geometric model of the (a) left and (b) right coronary arteries

These structures were later added to the aortic valve model created in section 2.1.1. A connecting surface was created in between the protruding portion of the ostia and the coronaries to compensate for the geometrical difference in their cross sections as shown in Figure 2.7.

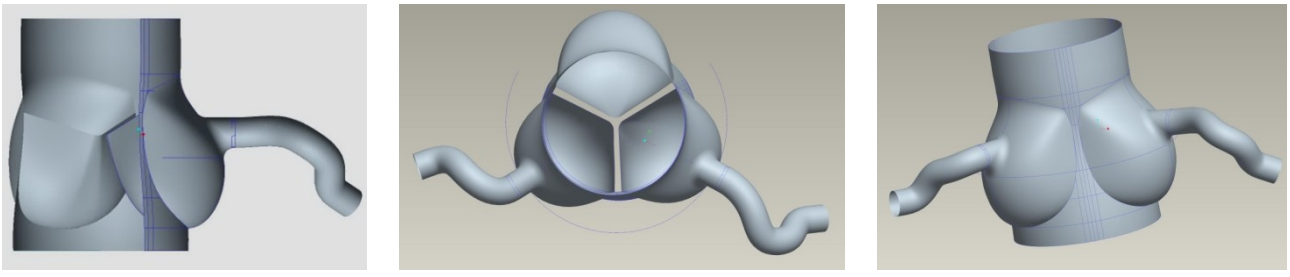

(a) (b) (c)

Figure 2.7: (a) side, (b) top, and (c) isometric view of the CAD representation of the aortic valve model including the coronary structures.

2.2.2 Finite element model

2.2.2.a The structural/Lagrangian domain

Element creation procedure for the structural domain is similar to that of the aortic valve explained in section 2.1.2.a. The only noteworthy difference is the mesh refinement performed on the coronary structures. This is due to the smaller geometry of these arteries in comparison to the aortic root. The final mesh of the structure is represented in Figure 2.8.

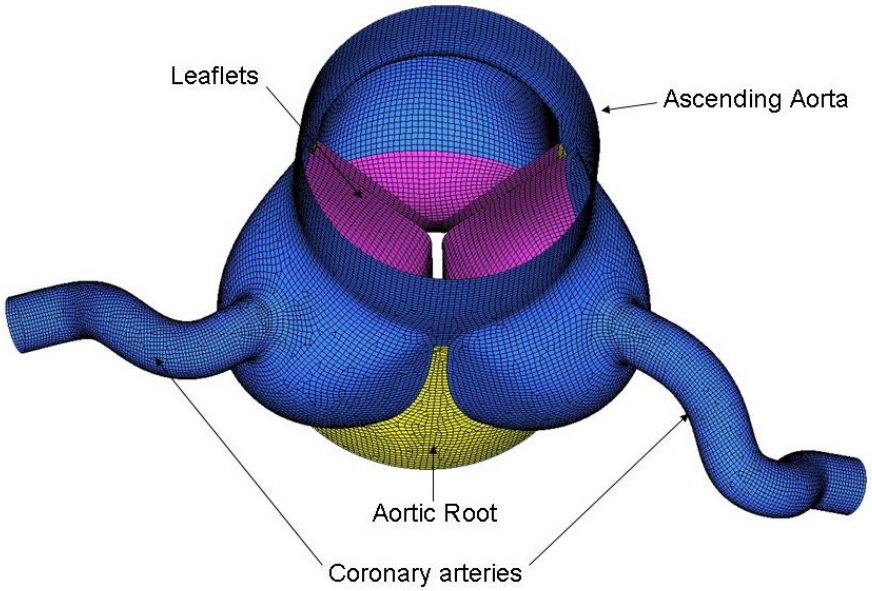

Figure 2.8: Isometric view of the final FE model of the aortic valve

2.2.2.b The Fluid/ALE domain

Contrary to the structural mesh, the ALE mesh generation for the fluid domain presented us with a highly demanding challenge. Certain requirements need to be simultaneously met and satisfied in order to achieve proper element creation. Expansion of the previously developed ALE domain seems to be the logical choice that requires the least amount of modification. However, there are several problems that arise from such expansion. The surfaces of the coronary outlets and the cylindrical surface of the surrounding main fluid (CSSF) would be situated on a different plane in the XYZ reference of frame. This problem could simply be overcome by trimming the coronary artery surfaces by the CSSF and applying the boundary conditions using vectors normal to the original coronary outlet surfaces. However there remain

two significant problems associated with this approach: first, by expanding the fluid domain, the computational cost increases significantly and the computational time required for a single simulation would vary in the range of 1 - 2 weeks. The second problem is linked to the elements near the coronary outlets and how they are created in perspective of the fluid domain. The mesh of the fluid domain can be created in two ways: first, by simply expanding the existing main fluid mesh towards the CSSF. This approach does not pose an issue for the mesh surrounding the leaflets since they are in the center of the main fluid. However it will certainly affect the elements as they get closer to the CSSF due to an increase in their size and aspect ratio and eventually becoming ill-shaped and unproportional. The second approach would be to create a finer 2D mesh at the bottom/top surface of the main cylinder and "extruding" it in the direction of the aortic valve axis to achieve a better mesh quality near the coronary structures. This approach however would increase the time necessary for the calculations to an average of 6-8 weeks for a single simulation which is not reasonable due to the large number of simulations necessary for our research. The simplest solution to this problem would be to eliminate the unnecessary elements in the expanded fluid mesh to reduce computational costs as shown in Figure 2.9.

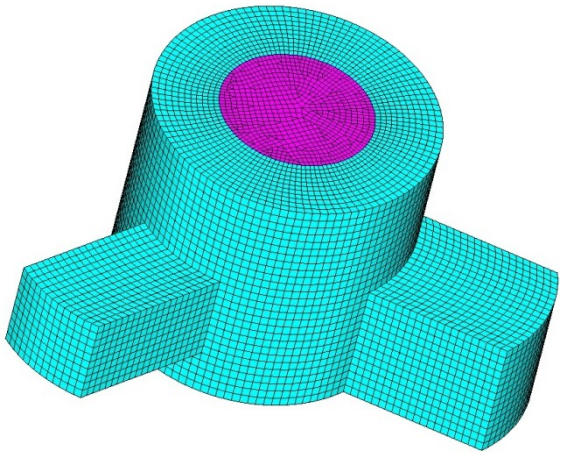

Figure 2.9: Reduction of fluid domain mesh by eliminating unnecessary elements surrounding the coronary arteries.

Since the coronary arteries are smaller geometries compared to the aortic valve, very few elements are generated in front of the coronary outlets and therefore the number of nodes that could be used for boundary condition application would be insufficient. A similar problem exists in the axial direction for these structures since a finer mesh is necessary along these arteries as

well. To add to these complications, it should be mentioned that having in/outlets in the fluid domain that perfectly match the geometry of the structure is an important requirement for the FSI simulations. This is particularly important in the implementation of boundary conditions such as pressure and velocity at the coronary outlets. This allows for a uniform boundary condition application without creating irregularities at the edges and uncertainty about interpreting the results related to structural dynamics or perhaps hemodynamic variables downstream.

Many attempts were made in order to address these issues simultaneously by meticulous 3D mesh refinements near the aforementioned local areas. Circular in/outlets were created in the fluid domain facing their corresponding structural in/outlets to account for proper boundary condition application. However, due to the "mapping" methodology – extrusion of a 2D mesh to create 3D mesh volumes- used by most commercial FE software to achieve hexahedron elements, these surfaces had to be divided into smaller parts for mesh creation purposes and merged back together to create one final assembly as shown in Figure 2.10.

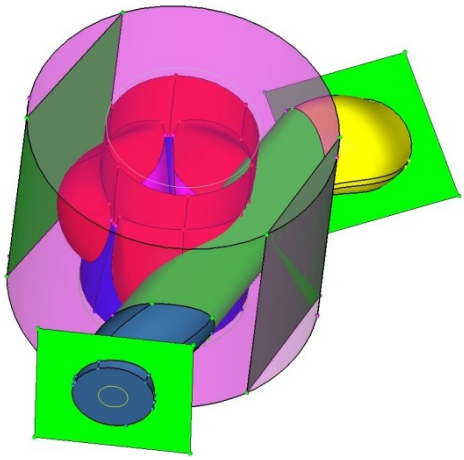

Figure 2.10: Separation of the fluid domain geometry in order to allow for mapping of 2D elements.

Despite the incapability of this method in creating the proper required mesh, there still remains a potential problem related to this approach concerning any future expansion or modification of this work. Having a "parametric design" as one of the objectives of this thesis and considering all the manual and unrepeatable effort needed to create the fluid mesh, it becomes apparent that an automatic mesh creation would not be readily available. Slight modifications in the geometry would require the user to re-generate the fluid mesh repeating exhaustingly tedious and labour intensive mesh creation procedures.

This led us to create a parametric mesh which is based on the structural geometry and can satisfy the following requirements simultaneously:

- be comprised of hexahedron elements
- have a parametric mesh that is based upon the structural geometry to allow repeatable mesh generation despite variations in geometry
- allow for circular in/outlets at different planes
- allow for manual mesh refinement near the coronary arteries and leaflets
- allow coronary artery mesh to follow the curvature of these structures to facilitate data extraction along them with constant accuracy
- maintain an overall element ratio between structural and fluid elements
- minimize the overall size of the fluid domain to reduce computational cost

To the best of our knowledge none of the commercial software available are capable of satisfying all of these requirements simultaneously using their automated features. TrueGrid by XYZ Scientific Applications, Inc. however, appeared as the only software capable of creating a high quality hexahedron mesh that satisfies all of the above requirements. The following section will explain in detail the basics of TrueGrid and its capabilities.

2.2.2.b.1 An overview of TrueGrid

TrueGrid software is suitable for creating a multiple-block-structured mesh. In many ways it is similar to sculpting. At first, the geometry of the object is either generated within TrueGrid or imported into it in the format of an IGES file. Afterwards block meshes comprised of hexahedron elements are created. Depending on the geometry of the object certain parts of these blocks are then removed (to create holes for example) so that their topology matches that of the object. These blocks are then moulded into the shape of the geometry by positioning their faces, vertices or edges along lines, curves or surfaces of the desired geometry. This mesh will then be optimized in terms of its quality using interpolation and smoothing algorithms. Depending on the complexity of the geometry multiple parts might be created which will then be merged together using “block boundary” interfaces (BB). There are several advantages to using TrueGrid which led us to use it as our meshing software: it can be run in either a batch

mode or an interactive environment, mesh refinement can easily be achieved and parametric meshes can be created. The biggest advantage however compared to automatic mesh generation of commercial software is that a session file is created which can be edited using any text editing software and be re-run in the batch mode to regenerate the mesh. This allows de/activating, adding or removing command lines in this session file which translates into quick mesh modifications without repeating the entire meshing procedure.

This capability of TrueGrid is achieved by taking advantage of two individual yet connected environments (representations of a mesh): the physical and the computational. The physical environment (PHE) is the physical space where the mesh formation (sculpting) occurs while the computational environment (CE) is a virtual space in which representation of the physical mesh exists by means of blocks created from integer valued points. Therefore the computational mesh is fixed in space and does not move. This mesh serves as a convenient way of controlling critical regions of the physical mesh that need to be positioned and moulded on the geometry. In order to achieve this, the two environments are correlated through two coordinate systems. Customary to any physical environment, nodes/elements in the physical space are identified using the three coordinates x, y, and z (location is space). Nodes in the computational space however, have three indices i, j, and k ("reduced indices"). This means every major point in the mesh has six coordinates: three indices in the computational environment and three coordinates in the physical space. This is basically how these two environments are linked to each other. Since only reduced indices can be referenced during the mesh creation procedure, the initial definition of these indices is very important so that they correspond with those features of the part which might need manipulation or attention.

Indices in the computational space represent a geometrically critical location in the physical space. If there are five locations in the Z direction which for example need to be considered for mesh refinement or include a hole, there should be five k indices each corresponding to every critical location. This does not mean that there are only five elements along the Z axis. The number of elements is defined using "full indices". This has been explained below using a simple block command:

block 1 10 15 30 ; 1 4 7 ; 1 2 ; 0 1 2 3 ; -7 -5 -2 ; -3 5

i j k x y z

The block command above represents a block in the computational space which has four indices in the i, three in the j and two in the k direction. These points correspond to critical locations of the physical mesh and are located in their corresponding x, y and z coordinates defined in the last three sections. The number of elements in the physical space between each adjacent index is defined by the actual numbers defined in the first three sections. For example, there are five (15 – 10 [i indices]) elements in the x direction between the second and third critical location in the physical space. Modifications are therefore a simple task once the session file is created. Mesh refinement can be performed by adjusting the values defined in any of the indices.

Once these initial blocks are created, a region of the mesh is selected by using "reduced indices" and is "projected" onto a specific surface. All the nodes of that region will be projected to the closest point on that surface. The remaining nodes will also be moved in order to maintain spacing and interpolation rules. These interior nodes are placed using linear interpolation methods unless specified otherwise. A detailed description of the methodologies used in this software can be found in TrueGrid User's Manual, A Guide and Reference Manual [98]. The following section is a step by step explanation of the Eulerian mesh creation for the aortic valve model.

2.2.2.b.2 Eulerian mesh creation using TrueGrid

The fluid mesh is based on the principle of creating interconnecting parts which would comprise the in/exterior regions of the cardiac tissue. These parts are created parametrically using a session file (text file) and depending on their location relative to the vasculature, they either expand to volumetrically fill the tissue or develop into a hollow mesh which encompasses the cardiac tissue to account for the surrounding fluid. As a first step a geometric representation of the fluid volume is created which acts as an external boundary limit to the fluid mesh. This geometry, shown in Figure 2.11, is imported into TrueGrid using an IGES import function. Certain curves/surfaces will be added to this geometry in subsequent steps which aid in mesh

creation by acting as a reference edge/surface for node/element positioning. These parts are created in the same order as they are numbered below in Figure 2.11.

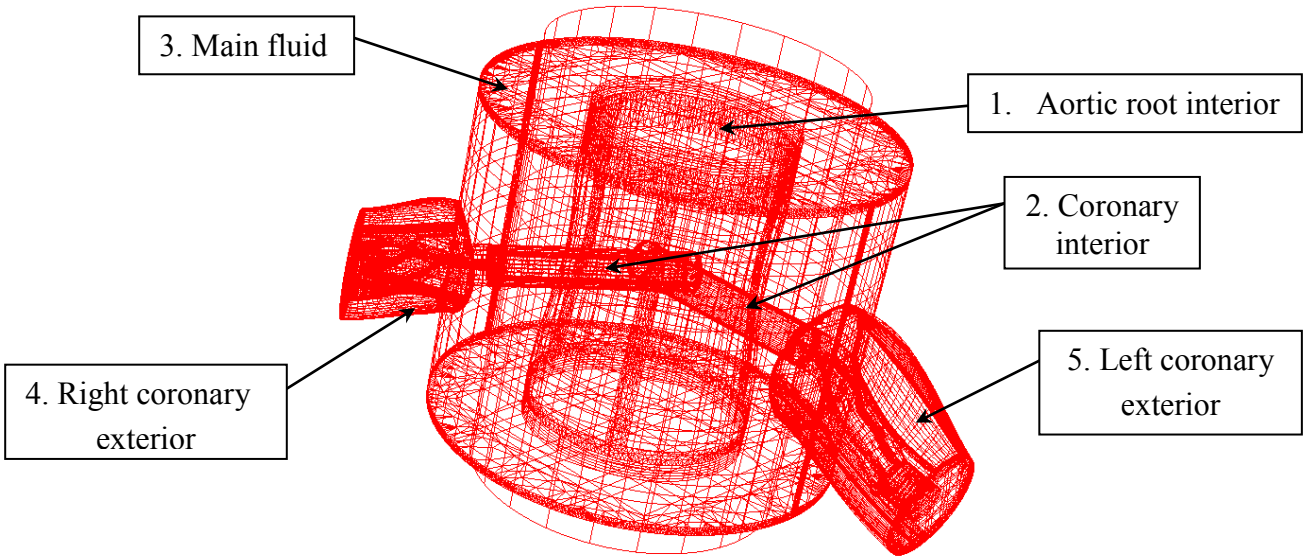

Figure 2.11: The geometry created to define boundaries for interior and exterior meshes of the fluid domain, relative to the structural mesh.

The first part which acts as the base mesh fills the interior portion of the aortic root using a block of elements in the PHE as shown in Figure 2.12(a). Certain sections need to be removed from this block in the CE to: 1. accommodate for the addition of the coronary arteries, and 2. allow for a "butterfly mesh" at the top and bottom surfaces. These surfaces will serve as the main inlet and outlet of the model and therefore require having a high quality mesh. Figure 2.12(b) shows the projection of this block in PHE onto the aortic wall interior surface resulting in two block shaped voids on the side of the mesh, which will later accept the coronary artery meshes. Figure 2.12(c) shows this same block represented in the CE.

An important modification however is crucial at this stage to warrant proper element size transition from the finer coronary structures to the more coarse mesh of the aortic root. The solution involves transferring the block shaped voids on the aortic root into spheres as shown in Figure 2.12(d) and (e) in "hide" and "wire" view respectively. The formation of spheres allows for a gradual increase in element size, from fine elements at the core of the spheres to more coarse elements at the external surface allowing for the required transition while maintaining mesh quality. The proper size for the radius of these spheres was decided by verifying element

quality index (aspect ratio, warpage, skew, jacobian, taper, …) through a trial and error process. Simultaneously, the block in the CE was divided further which provides more control over the course of mesh creation/refinement as shown in Figure 2.12(f).

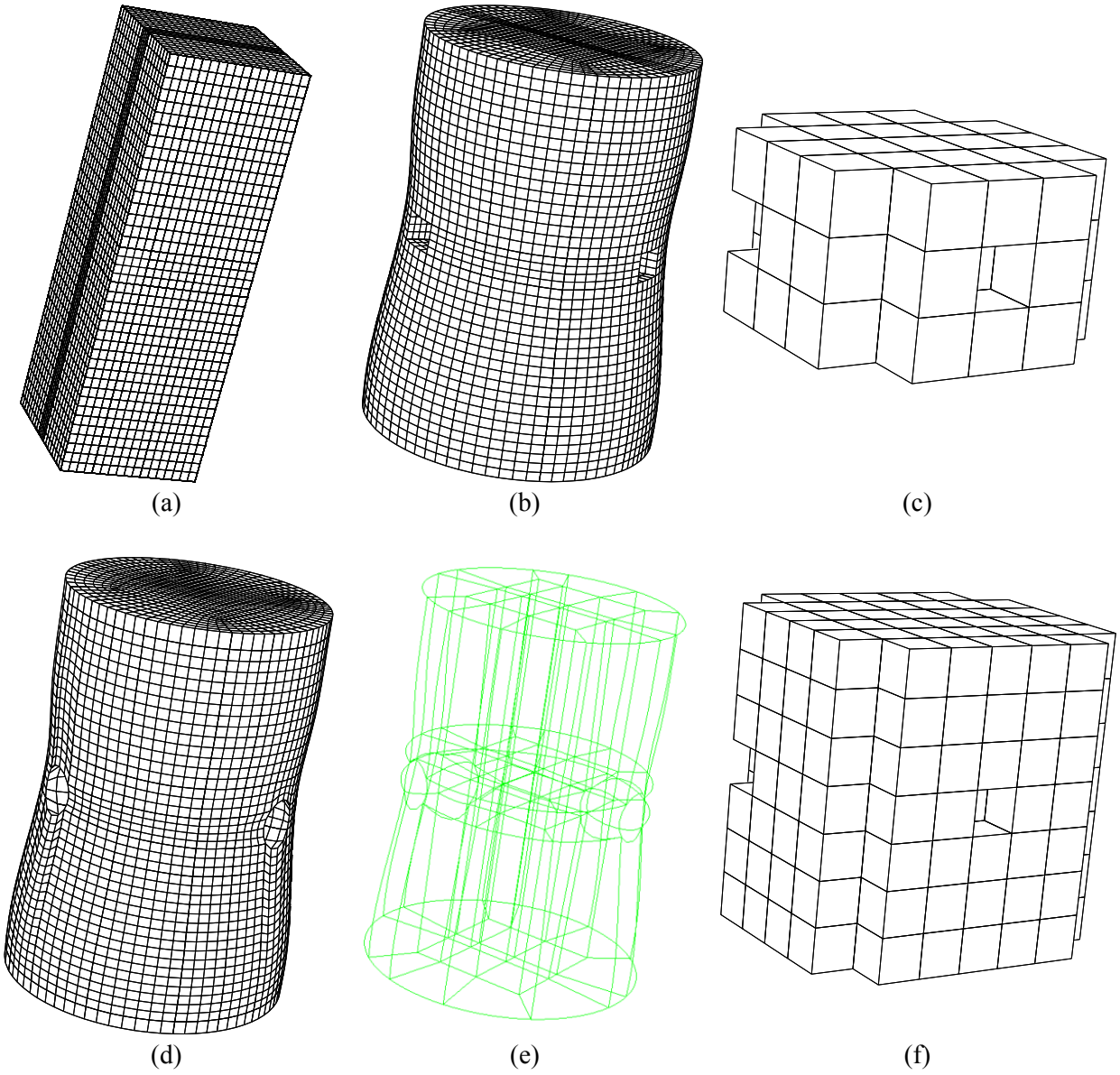

Figure 2.12: Images of (a) initial block creation, and (b) its projection to the aortic wall geometry and (c) the corresponding block in the computational domain. The mesh refinement required for spherical adaptors of coronary artery meshes is shown in (d) hide view and (e) wire view and (f) the refined block mesh in the computational environment.

Figure 2.13(a) shows the final fluid mesh of the aortic root interior including the *circular* inlet and outlet of the model that *match* the structural geometry of the cardiac tissue and *allow for mesh refinement* in the coronary structures as it will be seen in the following paragraphs. Figure 2.13(b) and (c) show the final fluid mesh of the aortic root interior in the PHE and CE respectively while having some of their features highlighted in different colors to aid the reader in better understanding how these two environments are related to one another.

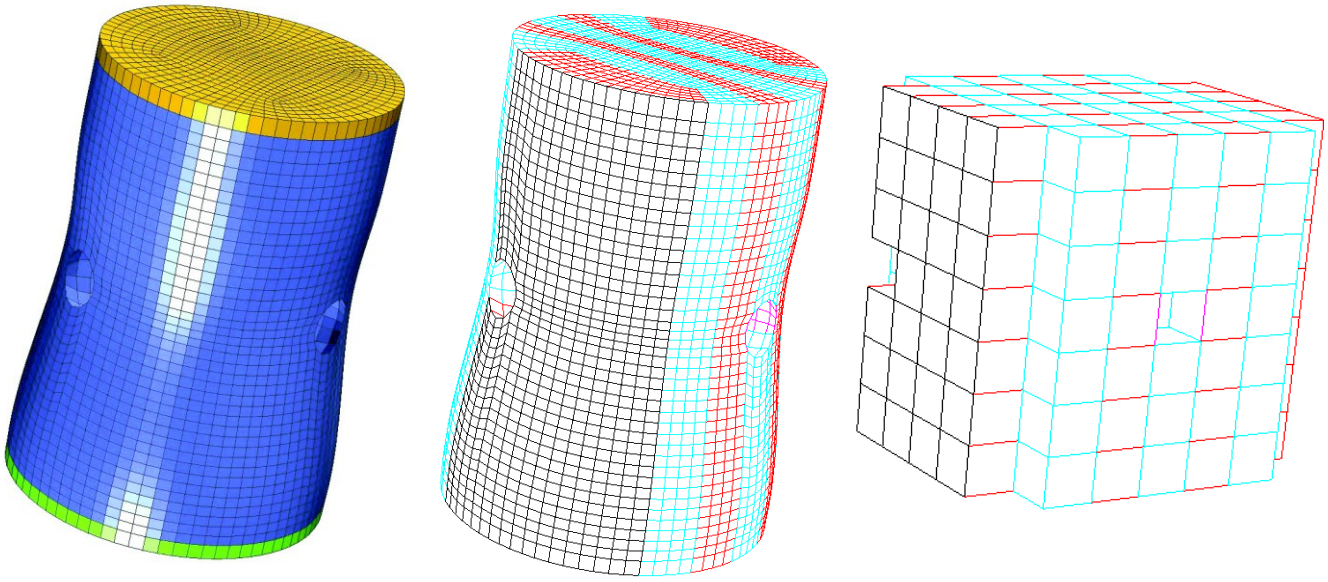

(a) (b) (c)

Figure 2.13: (a) Fill view, (b) wire view, and (c) computational block of the Interior mesh of the aortic root.

The next step involves the inclusion of the elements that will fill the interior portion of the two coronary arteries. These meshes need to follow the curvature of the vessels, have a high quality and relatively fine butterfly mesh at the outlet and also match the spherical voids created on the aortic root fluid mesh. Even though different in shape, these two meshes are created following a similar procedure. Therefore we suffice to explaining the steps involved in creating one of these meshes. A block is created in the PHE considering the required element concentration near the inlet of these arteries in addition to the curvatures to accommodate for upcoming spherical projections and proper node distribution on the inside and outside curvatures. Specific attention should be paid to the number of nodes chosen on the inlet portion of this block (which will later become spherical) to eliminate discontinuity between the male and

female portions of the coronary artery and aortic root respectively. Figure 2.14(a) and (b) show the PHE and CE representations of this block for the right coronary. After eliminating the side rows of the block in CE [for butterfly configuration in Figure 2.14(d)], the nodes and edges of this block are then projected onto the surface of the coronary structures using the predefined curves and lines as shown in Figure 2.14(c). The spherical portion of this mesh was created using a similar radius to that used in their corresponding female receptor on the aortic root. The locations of the surface nodes on these spheres were later matched to those of their female receptors. Several smoothing algorithms in conjunction with distribution algorithms were used to achieve a proper node distribution along the inside and outside three dimensional curvatures. Figure 2.14(e) and (f) show the final right and left interior portion of the coronary fluid mesh, respectively. These two arteries and the aortic root are then merged to eliminate duplicate nodes and create a continuous media as shown in Figure 2.14(g).

The next step involved creating the section of the fluid domain exterior to the aortic root. This is the portion which resembles the pericardial fluid and surrounds the aortic valve structure. Several points need to be considered prior to mesh creation including: 1. the number and position of the nodes and elements on the interior surface of this mesh should perfectly match that of the exterior surface of the aortic root mesh. 2. It should accommodate for receiving two remaining meshes which surround the coronary structures through two voids in its volume (similar to the aortic root fluid mesh). Figure 2.15(a) and (b) show the projected block of this mesh onto the exterior surface of the main fluid in the PHE and CE respectively. The central portion of this block in CE is removed as shown in Figure 2.15(b) and (d) to create a hollow cylinder in the middle of the fluid mesh to accommodate merging with the aortic root mesh. This merging process was achieved by first defining the faces of the elements situated at the exterior surface of the aortic root mesh as the “master face”. Next, faces of the elements situated at the internal surface of the main fluid mesh were considered as “slave face”. The full and reduced indices of the “slave faces” in the CE are chosen such that they would exactly match that of the “master face” from the aortic root mesh. “Block boundary” commands were used to attach these two surfaces. Figure 2.15(c) shows the projection of the two side voids onto the left/right exterior surfaces of the coronary structures. Figure 2.15(e) is a close up of the same mesh to better visualize the projection procedure. Figure 2.15(f) is a side view of the merging of the four parts created so far.

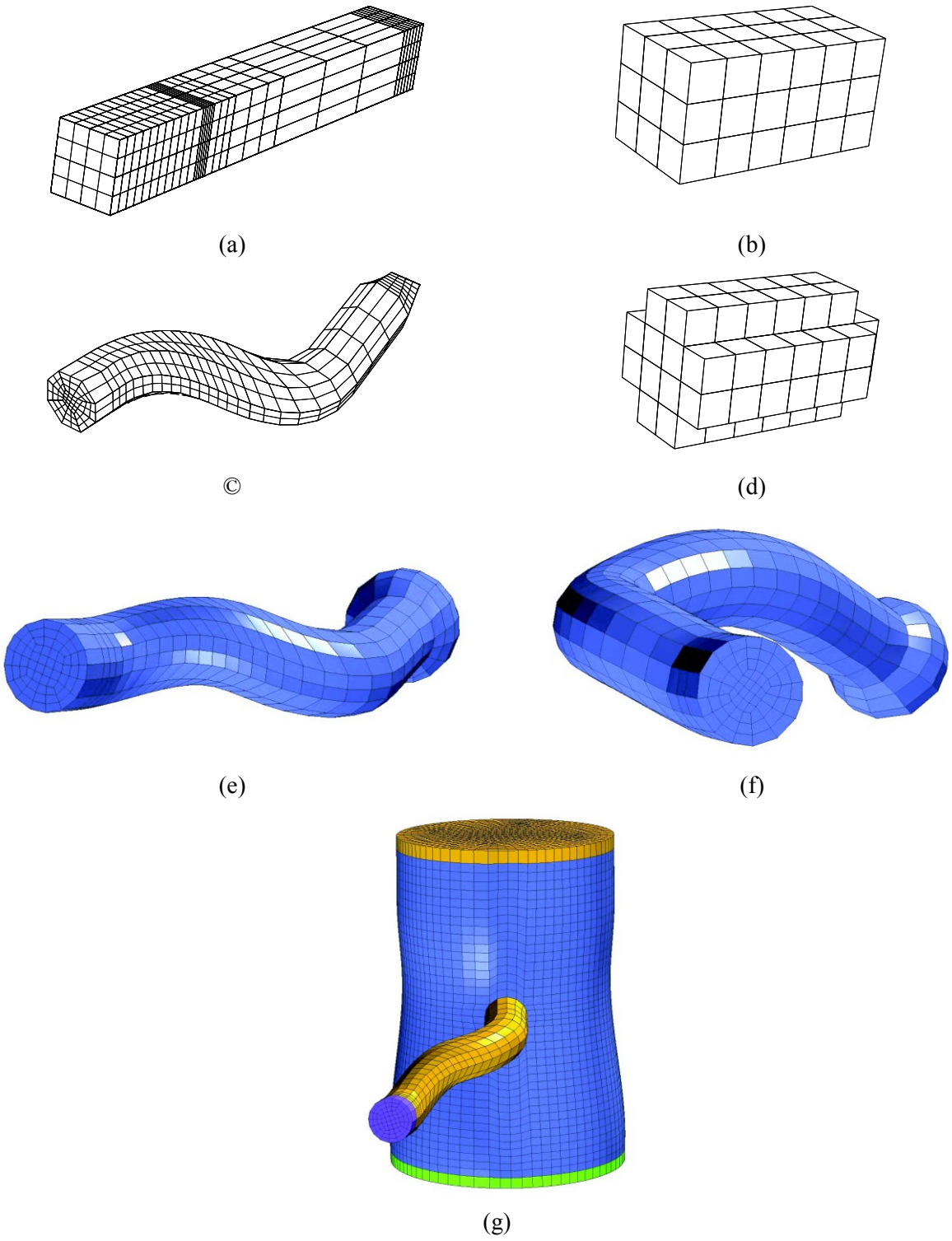

Figure 2.14: Initial block of the internal portion of the right coronary fluid mesh in (a) PHE and (b) CE and (c) its projection to the coronary artery structure after (d) block elimination in CE to accommodate for butterfly mesh. Final fluid mesh of the (e) right and (f) left coronary arteries and their male spherical projection that fits into the female receptor of the aortic root and (g) their merge to the aortic root.

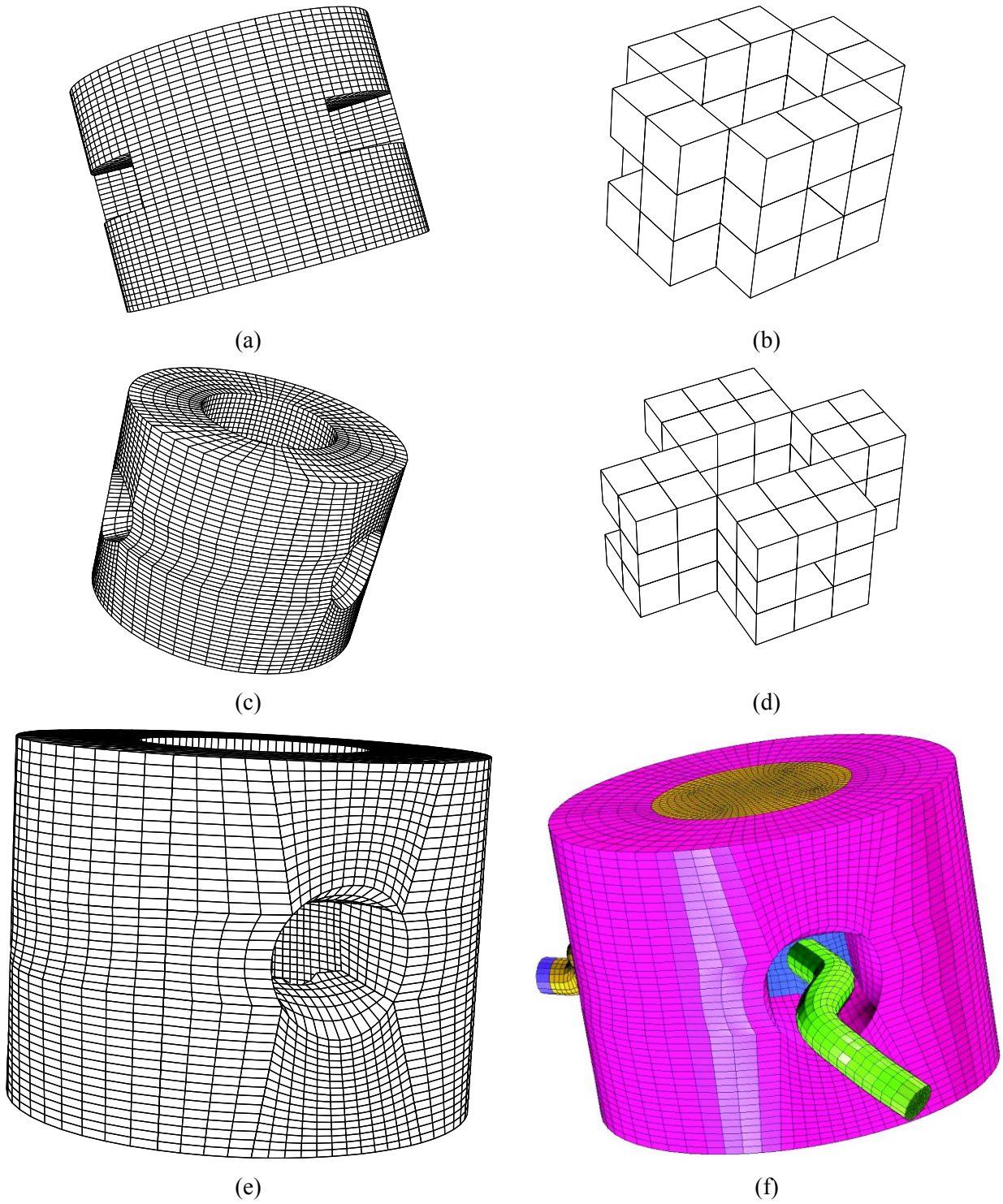

Figure 2.15: The initial projection of the main fluid block in the (a) PHE and (b) CE. This projection is followed by (c) the projection of the two side voids onto the coronary exterior surface and (d) necessary refinement of the indices in CE. (e) A close up of the fluid mesh better reveals the projection procedure while (f) shows the merging of the main fluid mesh and the previously defined parts.

Once the main fluid mesh is generated, the only parts needed to complete the Eulerian mesh are the two exterior coronary meshes. These are the elements surrounding the internal coronary meshes created in the second step to account for the surrounding tissue and fluid. The process is no different from what has been observed however; both of these parts come in contact with three neighbouring meshes (aortic root, main fluid and interior coronary) simultaneously. Therefore the indices in the CE to create the initial block need to be cautiously chosen. Figure 2.16(a) shows the block of the right exterior coronary mesh prior to projection. There are seven faces of this mesh that need to be either projected to a surface or bounded to a previously created mesh using "block boundaries". These faces include: the interior hollow faces (should match the interior coronary mesh), the back face (should match aortic root mesh); the four faces that come in contact with the main fluid; and finally the external face of the mesh which will be projected to the surface of the coronary exterior. Figure 2.16(b) shows this last step while Figure 2.16(c) and (d) represent the final mesh of the right and left coronary exterior, respectively.

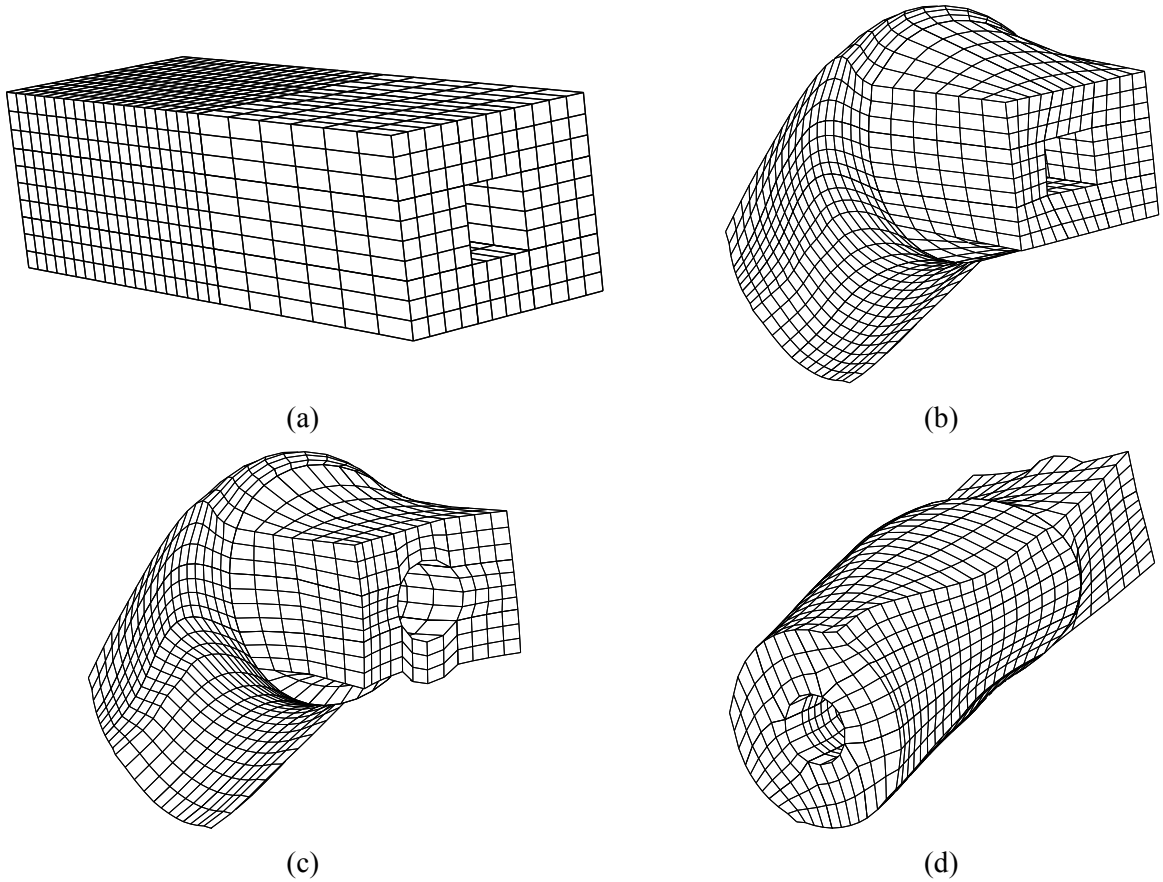

Figure 2.16: (a) the right coronary exterior block in PHE prior to (b) projection onto the surface of coronary exterior. The final mesh of the (c) right and (d) left coronary exterior.

Figure 2.17(a) shows the merge between the aortic root and the coronary exterior mesh while Figure 2.17(b) shows the same image with the addition of the main fluid. The left coronary interior mesh can be seen protruding from the main fluid. Figure 2.17(c) shows the final Eulerian mesh while the containing parts are coloured individually for better visualization. These six parts are merged together and have no discontinuity.

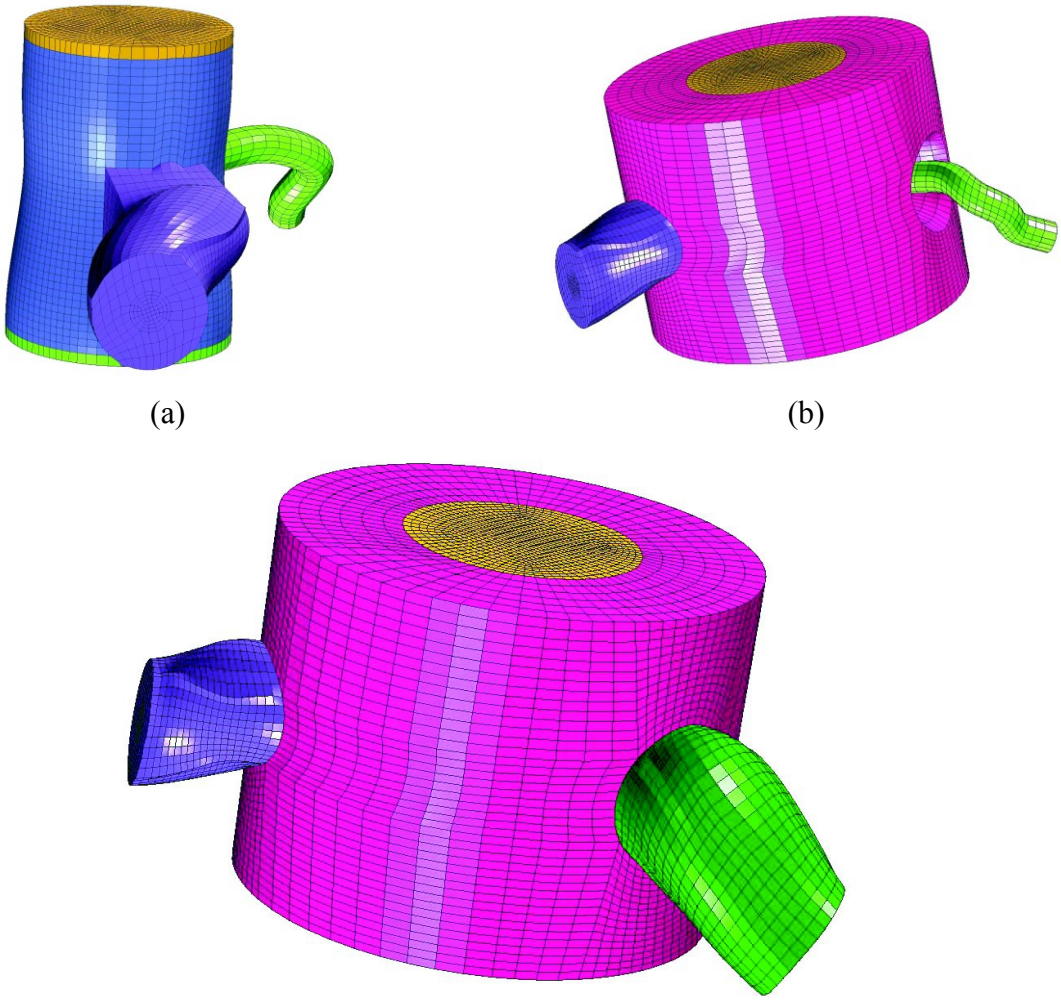

(a) (b)

(c)

Figure 2.17: (a) The addition of coronary exterior to the aortic root; and (b) main fluid mesh. (c)The final mesh of the Eulerian domain after merging its individual parts.

In reality, this final mesh is a session file which can easily be modified if necessary by making few editions in the command lines of this file. The parametric nature of this mesh allows for quick reconstruction of the fluid domain in case of a change in the structural domain. For

instance, a new structural geometry (in patient specific or pathological cases) can be studied by simply updating the link to the IGES file of this new geometry. The process of creating the fluid mesh is easily repeatable depending on the necessary modification. Modifications to the coronary structures however, would require more time consuming editions to the session file due to the need for recreating the necessary curves required for "projection" commands as well as updating values for mesh smoothing commands along the arteries due to their high curvatures. Despite the longer process required, an updated mesh can be created in a fraction of the time necessary for creating a new mesh whenever a slight variation occurs in the structural domain. An application of such versatility will be seen in the next section of this chapter where we include a stenosis in one of the coronary artery structures.

2.3 Pathological global model of the aortic valve: Inclusion of coronary stenosis

As explained in the clinical background, coronary stenosis is one of the major pathologies of the aortic root and coronary structures. To investigate our hypothesis where we suggest the possibility of a global disease of the aortic valve region, three different percentages of stenosis were included in the left coronary artery structure. To isolate the effect of coronary stenosis, the rest of the FSI model remained intact. The geometry of the stenosis was created using an eccentric blister type protrusion using symmetrical Gaussian curves along the longitudinal axis and different heights to account for the different degrees of stenosis [99]. Generic geometry of stenosis was used to represent an average shape of this pathology that would be clinically observed. Three percentages of stenosis including 75%, 83% and 91% stenosed lumen area were modeled by varying the height of the longitudinal Gaussian curve. These values of percent stenosis were chosen since occlusions above 75% are considered to be severe and are believed to be the starting point of myocardial infarction [100]. The geometry of the stenosis was created assuming a straight cylindrical coronary which was 20 mm long while the length of the stenosis was considered to be 15 mm. These geometries are shown below in Figure 2.18.

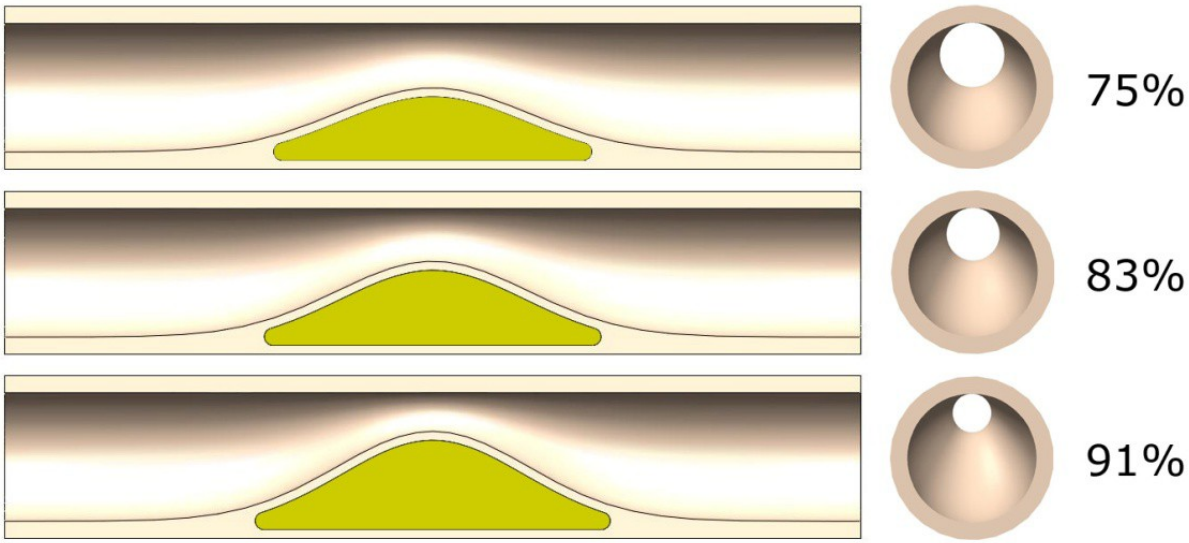

Figure 2.18: Side/front view representation of the geometric models of the coronary stenosis and their respective percentage of area stenosis (taken from [99])

Since these geometries are created in a straight cylindrical coronary, certain modifications are required to allow for merging them to the existing geometry of aortic root model. Due to the limited number of curves that are available on the stenotic geometries, connecting them to the previous CAD files of the root proved to be a challenging task. Therefore, the alternative solution was to mesh these structures and use their surface nodes as guiding points along some predefined curves. These curves were created using the nodes on the existing coronary arteries of the aortic root model. This procedure greatly aids in positioning these geometries along the curvature of the model. The three dimensional nature of these models causes complexity in positioning them at the exact same location. This was solved by using the top longitudinal line of these surfaces (shown in red in Figure 2.19) as a reference to assure that all three geometries are positioned and merged to the existing geometry in a similar fashion.

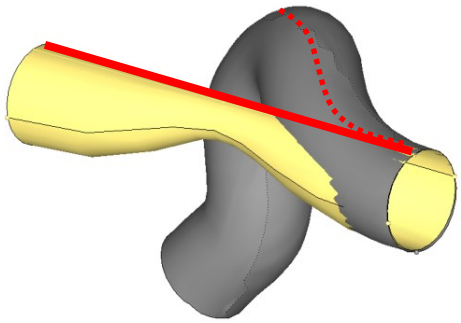

Figure 2.19: The longitudinal reference line used to position the geometric coronary stenosis.

The meshing of these structures had to be performed manually to guarantee having the same number of nodes and elements on either end for proper merging operation to the existing coronary elements. Hypermesh from Altair Hyperworks was used to perform the meshing procedure using the same element size used for the normal arteries in the aortic valve model. Figure 2.20 below shows the final structural mesh of the pathological aortic root model.

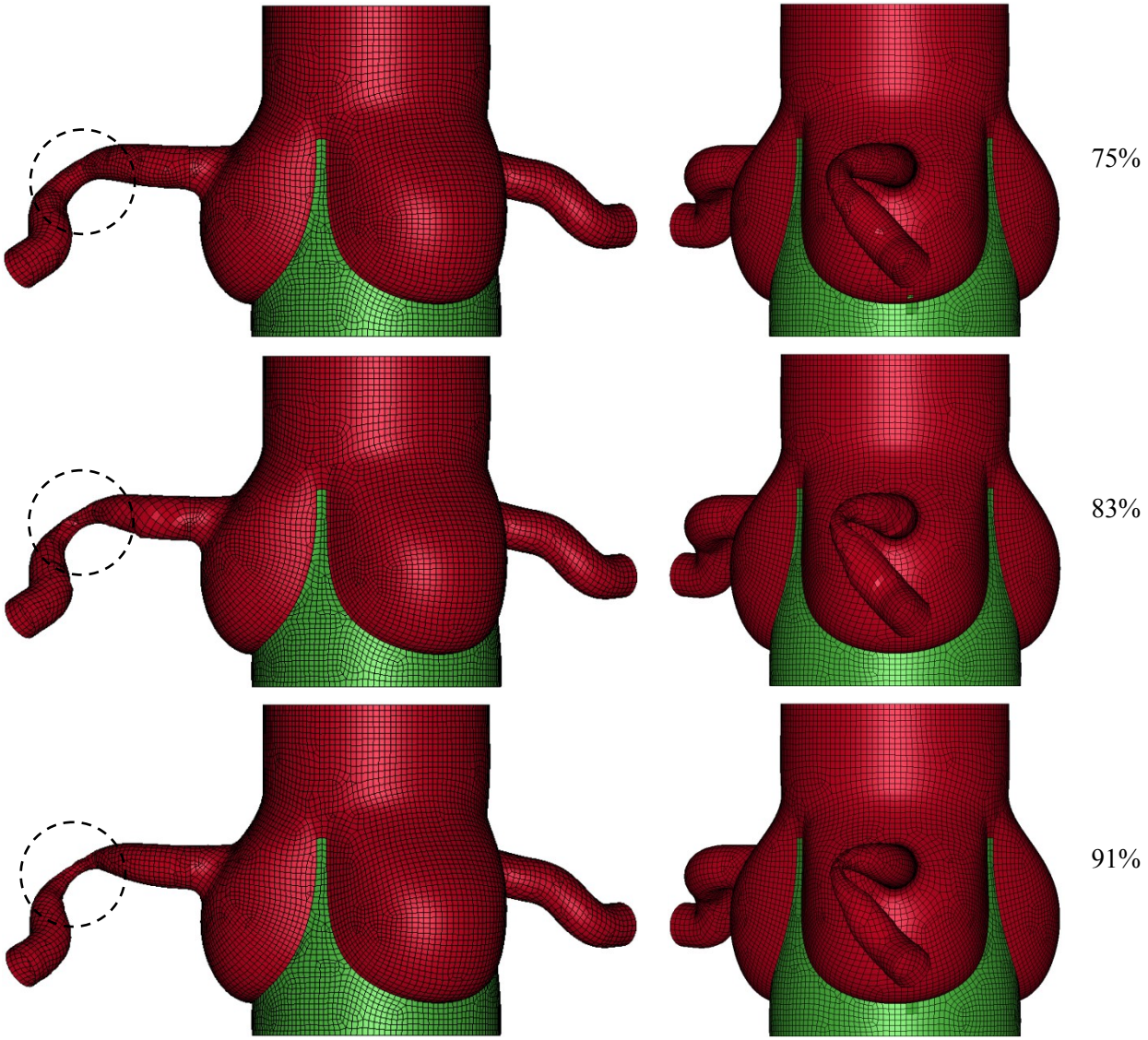

Figure 2.20: Finite element mesh of the aortic root with the inclusion of coronary stenosis and their respective percentages.

The fluid domain mesh is created automatically using the session file explained in the previous section and by using the new geometry of the aortic root.

2.4 Material property models

The following two sections will describe the material property definition used in this work. The cardiac tissue and the fluid will be discussed separately and the assumptions made will be discussed.

2.4.1 Vasculature material models

It is well established that cardiac tissue is a hyperelastic, orthotropic and heterogeneous material. Throughout the years there have been numerous experimental as well as numerical studies that have investigated and focused on cardiac tissue properties and in particular; the aortic root. As discussed in section 1.2.6, some of these studies have incorporated some or all of the aspects into their numerical models. However, it should be mentioned that as the complexity of the material used increases, the more instability is introduced into the simulations. Therefore, it is a common practice to use assumptions in order to simplify the problem. Many of these studies are performed in an Eulerian nature and have neglected the FSI behaviour of this region, while others have resorted to simpler geometries or smaller regions of the aortic valve. Large deformation of the aortic cusps adds to all these complications and introducing them into an FSI model is parallel to convergence issues and instabilities. Fluid-structure interaction analysis has been used in biomedical studies for only a few decades. Therefore there are still many limiting factors associated with this type of analysis compared, for instance, to CFD. As a consequence most of the FSI studies conveyed in the aortic valve area have either considered a small region with more complex material properties; or have a more developed geometry with simplified material properties. To the best of our knowledge the model in this thesis is the most global 3D FSI model of the aortic valve to date.

Under normal physiological conditions, the strain in the aortic root varies in the range of about 10% [101, 102]. A recent study has shown that even though the stress-strain curve of the cardiac tissue is nonlinear, it can be subdivided into two linear regions: one at low strain range (below 15%) and another at high strain rates [103]. At low strain rates, this linearity is even more pronounced and a study by our group has shown that at these physiological strains the stress-strain curve of aortic tissue can essentially be considered linear [104]. Given the related advantages of reducing computational times and increasing the stability, we implemented a

linear elastic material property to model the healthy cardiac tissue with a Young's modulus of 3.34 and 4.00MPa for the aortic root and leaflets, respectively, and a Poisson's ratio of 0.45. These values are in the physiological range and are similar to the values used in previous studies [53, 105-107]. In fact, it has been shown that with this assumption the stress levels are within acceptable ranges as compared to hyperelastic modeling [108, 109]. Solid viscous effects were also neglected to isolate the impact that pathologies, affecting the elastic component in the cardiac tissue like wall stiffening and valve thickening, could impose on the energy storing capabilities of the elastic component.

2.4.2 Blood material model

Blood is well known as a non-Newtonian, heterogeneous substance. These properties are linked to the fact that blood is a concentrated suspension of red blood cells (erythrocytes), white blood cells (leukocytes) and platelets (thrombocytes). These cells are suspended in a solution referred to as plasma which is considered to be a Newtonian fluid. Red blood cells are the most dominant in volumetric percentage (hematocrit) compared to the other cellular elements comprising about 45% of blood volume in any healthy individual. This means that red blood cells (RBC) have a considerable impact on the material properties of blood and are the primary source behind its non-Newtonian effects. Generally, three properties of the RBCs are known to lead to this behaviour: their capability to deform, their tendency to align with the flow field at high shear rates (to allow passage in narrow vasculature) and also their ability to stick to each other (due to their unique discoid shape) and form rouleaux which normally occurs in low shear rates. As a consequence, the viscosity of blood depends on how the RBCs are oriented and behave. These cells are basically made of an elastic membrane confining a fluid within; which can lead to viscoelastic behaviour which becomes less important at high shear rates [110, 111]. Also, at low shear rates (below 1 s^{-1}) the blood exhibits high values of viscosity, while at high shear rates there is an apparent reduction in its viscosity; a phenomenon known as the shear thinning effect of blood that was first reported Chien et al. [112]. However, studies have shown that regardless of this non-Newtonian, shear thinning, viscoelastic nature of blood, in investigations involving large vessels and high levels of shear rate (>50 s^{-1}) associated to the aortic valve region, a simple Newtonian material could be used for the blood [113, 114] with a dynamic viscosity ranging between 3 and 4mPa.s and a specific gravity of 1060 $kg.m^{-3}$.

The data related to the pericardial fluid covering the outside of the cardiac tissue however is not as accessible as blood. In fact to the best of our knowledge, human pericardial viscosity has not been reported in the literature. However, its consistency was reported to be similar to blood serum [115]. Given that normal values of blood serum are in the range of 1-3 mPa.s [116, 117] and for the associated simplification, it seems reasonable to use the same viscosity as blood for modeling the surrounding fluid. Therefore the material property of the fluid domain/blood was considered to be Newtonian with a dynamic viscosity of 3.5 mPa.s and a density of 1060 $kg.m^{-3}$.

2.4.3 Boundary conditions

Since in this thesis, different geometries of the aortic valve region have been investigated, the boundary condition section will be explained accordingly. Due to the FSI nature of the study, the Eulerian and the Lagrangian boundary conditions (BC) will be discussed separately to avoid confusion. It should be noted that the Lagrangian (structural) boundary conditions are very similar among the different models. On the contrary, the Eulerian (fluid) boundary conditions vary among different model/geometries which is due to the introduction of coronary structures into the model. Therefore, the Eulerian BCs have been described accordingly.

2.4.3.a The structural domain

The boundary conditions of the structural domain in this work generally serve three purposes: to define contact between two shell sections which come in contact with one another; to prevent rigid body motion; and to restrict displacement in certain directions to simulate physiological conditions. These boundary conditions constrain the rigid body motion (twisting, rotation, translation) but permit deformation of the structure. To achieve this end, the geometry of the model contains a significant portion of the ascending aorta to fully constrain the outlet ring without affecting valvular dynamics. This constraint restricts motion and rotation in any direction at the top edge of the ascending aorta. On the other hand, at the level of the inlet ring, a constraint was applied to prevent the model from deforming and movement in the axial direction only. Hence the radial motion, and thus root expansion, was not constrained at the inlet. Next, at the level of ostia and the coronary outlets (in the models which include the coronary structures) a

set of boundary conditions were defined which allowed expansion in the direction normal to their axis (accounting for expansion under pressure) but restrained them from moving randomly. This issue was more pronounced in the curvatures of coronary arteries where pressure could cause these structures to kink similar to a watering hose. The contact between leaflets is defined using "contact_automatic_general" in LS-DYNA environment which is a single surface contact and checks for penetration along the entire length of the unshared shell edges. Every two neighboring surfaces define a master and slave set. During the analysis, each slave node is verified for penetration through the master surface and, if penetration occurs, a penalty force proportional to the amount of penetration is applied in order to return the slave node to the surface on which the master node lies. This is a critical point in the modeling procedure since it prevents the shell elements from penetrating through each other, defining their significant role in valve dynamics. The contact is considered to be frictionless which is a common assumption used by many research groups [53].

2.4.3.b The fluid domain

There are four locations in the fluid domain that require boundary condition definitions. These are the inlets and outlets of the model and require either pressure or flow to be prescribed. These boundary conditions are imposed at the aortic root, the ascending aorta, and the two coronary outlets. In order to account for the pulsatility of the flow, the inlet condition at the aortic root is taken to be the difference between the ventricular pressure and the aortic pressure shown in Figure 2.21(a). Therefore, the outlet of the ascending aorta has a free boundary condition, meaning fluid can flow freely, an approach borrowed from previous studies [53, 63, 68, 77]. The result is that the entire system is under an overall smaller pressure and the shell elements of the solid medium are subjected to a reduced transvalvular load while maintaining the pressure gradient across the valves.

As for the two coronary arteries, it is known that the hydraulic resistance of the coronary vascular bed is largely time dependent and that much of this phenomenon is attributed to the vasocontraction effects [118]. This resistance is one of the controlling factors of how much flow will enter each of the coronaries. Coronary flow values are well known during a cardiac cycle,

unlike coronary pressures which are largely unknown at the level of ostia or a bit further downstream. Pressure values for healthy individuals at these locations are even more difficult to find since most of the clinical data available are related to pathological cases. Vasocontraction of the arterial bed is the major factor in defining coronary pressure especially during diastole. Therefore in order to incorporate the proper boundary condition into the model, two types of boundary conditions were imposed at the ostia/coronary outlets depending on the model. For the normal base model clinical values of average coronary flow [119] were imposed as boundary conditions as a first step as shown below in Figure 2.21(b).

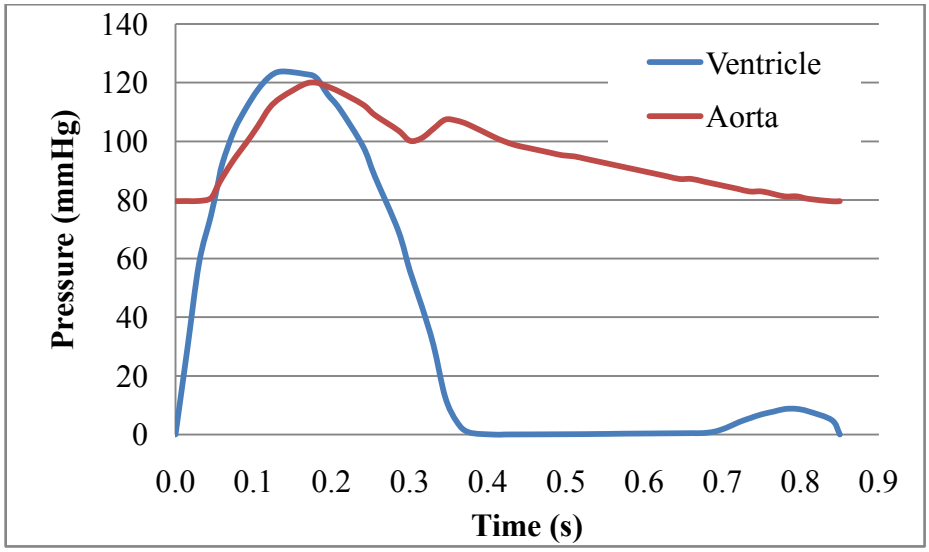

(a)

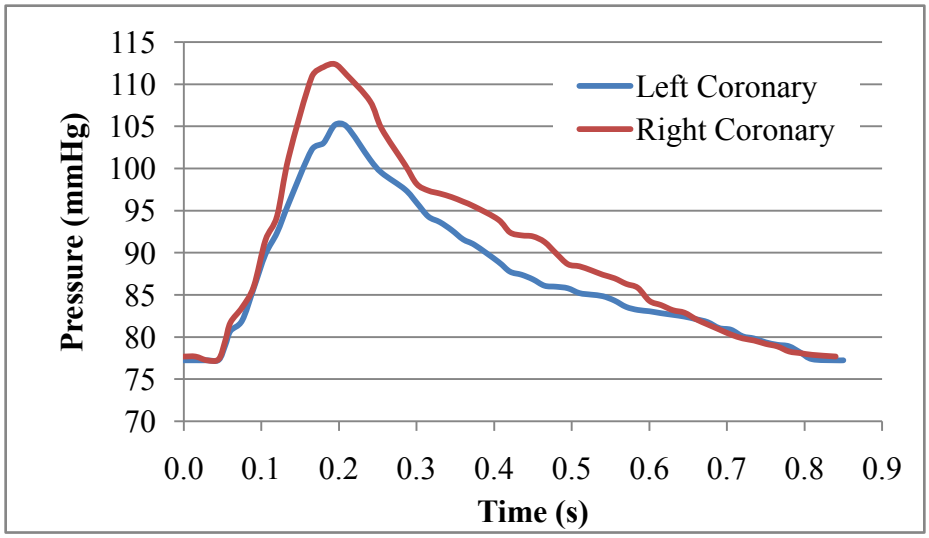

(b)

Figure 2.21: Physiological pressures at (a) the ventricular inlet and aortic outlet, and (b) left and right coronary outlets. The aortic pressure has been deducted from the ventricular and the two coronary pressure curves in our model.

This leaves the pressure and velocity profile unconstrained and allows them to self establish. Then, for pathological conditions, this same pressure obtained at the ostia of the normal case is used as the new boundary condition, which will allow the flow to self-establish. This enables us to study the effect of a single parameter on the coronary flow. The aortic pressure is deducted from the pressures calculated at the ostia in order to provide the proper pressure gradient in the model.

For the normal global model of the aortic valve, the same pressure curves shown in Figure 2.21 have been applied as boundary conditions but downstream of the ostia since the coronary arteries are included in this model. This is one of the advantages of including these structures in our FSI model. Applying BCs more downstream enables one to study not only the perfusion but the velocity profile and shear stress distributions along these arteries. One can also investigate the effect of geometrical factors such as curvature on coronary flow. Imposing boundary conditions away from the inlet eliminates one of the limitations of the normal base model and creates a more physiological model since the local hemodynamic is less affected by user inputs and can self establish. The "pressure reservoir" method is used to impose pressure as boundary condition which will is explained in the appendix section.

As for the pathological global model of the aortic valve coronary flow were imposed as boundary conditions. This allows the pressure field to self establish throughout the model and since the leaflets are passive structures driven by the transmural pressure, any variation in this pressure field could potentially impact valvular dynamics. However, data related to coronary flow in pathological conditions is quite limited in clinical literature compared for instance to, coronary flow reserve and fractional flow reserve measurements. These measurements are generally performed during vasodilation by injecting adenosine or receiving intracoronary nitroglycerin [120]. Since, the autoregulatory responses of coronary arteries were not in the scope of this thesis, normal coronary flows were modified using the values for fractional flow reserve reported by other studies. A thirty, fifty, and seventy percent reduction was imposed on the normal coronary flow for the 75, 83, and 91 percent lumen area stenosed arteries, respectively [121-123]. Moreover, one case in which coronary flows were completely blocked was investigated to study clinical cases where patients are completely dependant on collaterals. As an adaptive response to ischemia or acute angina, collateral anastomotic channels known as

collateral vessels, can develop in the heart [124, 125]. In the case of a chronic total coronary occlusion, these vessels provide an alternative source of blood supply to the myocardium by linking this section to another supplied by an epicardial coronary artery [126, 127]. This was achieved by imposing a “no coronary flow” condition in the arteries.

Chapter 3 : Results of the aortic valve simulations

In the previous chapter, creation of three aortic valve models that were used in this work was described. These models included: 1. the normal base model of the aortic valve which only included the ostia; 2. the global normal model of the aortic valve with the inclusion of coronary arteries; and 3. the global pathological model of the aortic valve region which introduces stenosis into the coronary arteries. Therefore the results of the simulations presented in this chapter have been divided into three sections each corresponding to a different model. The obtained results for each model have been further separated into structural and fluid sections.

3.1 The normal base model of the aortic valve

3.1.1 The solid medium

The engineering parameters of interest in the solid medium include the leaflet morphologies, leaflet velocities, and leaflet stresses. For the solid medium that contains the aortic root, sinuses, and ascending aorta, the most accurate clinical data available are related to the leaflets.

3.1.1.a Leaflet morphologies and dynamics

Looking from the ascending aorta back towards the left ventricle, known as the short-axis view, reveals some key features. An important aspect that can be quantified clinically is the cross-sectional valve opening during the cardiac cycle. The computed leaflet morphologies during the opening and closing phases are represented in Figure 3.1. Values were comparable with previous studies and the valve opens to 69% of the cross-sectional area of the aortic ring [64]. However, the commissural expansion is limited to 8% compared to the natural values of 12%. This is due to application of pressure gradient as boundary condition and will be discussed in the limitations section. Similar timelapse images presented by other authors have demonstrated a similar qualitative triangular orifice opening and leaflet billowing [49, 53, 64, 128].

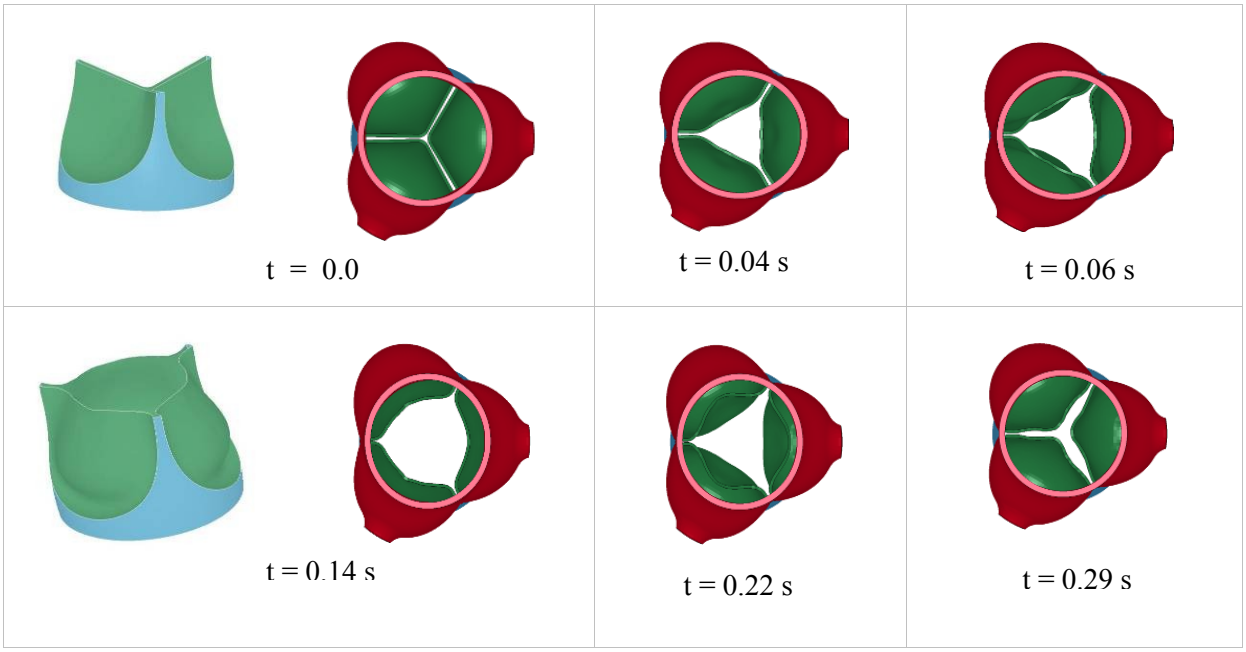

Figure 3.1: The computed opening and closing patterns of the leaflets, seen from the aorta.

The leaflets opening during the systolic phase includes some flickering and billowing of the leaflets which is similar to clinical and physiological observations. This is most obvious right before the maximum opening occurs at t = 0.14 s into the cardiac cycle. These large deformations are the main cause of complications related to FSI modeling of the aortic valve. The maximum opening of the leaflet tips is followed by the closing phase (beginning of diastole) during which the leaflet coaptation occurs and the valve becomes fully closed. The images related to the remaining of the cardiac cycle have been removed since there is not much variation observed in leaflet morphology after this point.

For a more quantitative assessment, leaflet tips dynamics have been tracked and values related to their velocities and accelerations have been calculated. Some common aspects of the leaflet dynamic histories that are also accessible to the clinician and surgeon through echocardiography data are the rapid valve opening time (RVOT), rapid valve opening velocity (RVOV), rapid valve closing time (RVCT), rapid valve closing velocity (RVCV), and ejection time (ET). A schematic representation of these parameters has been included in Figure 3.2.

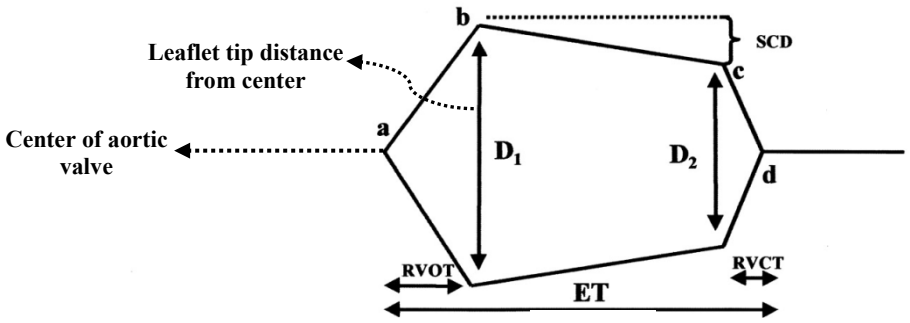

Figure 3.2: Schematic representation of clinical parameters of valvular dynamics: *ab* = rapid valve opening; *bc* = slow systolic closure; *cd* = rapid valve closing; *SCD* = slow closing displacement (edited from [129]).

For each of these five parameters, average healthy values have been determined [129-132]. These values are compared to those derived from the current model in healthy (120/80 mmHg: ΔP = 40 mmHg) and hypertensive (140/90 mmHg: ΔP = 50 mmHg) conditions and are presented in Table 3-1: Comparison between FSI and echocardiography leaflet dynamics. Our results matched the echocardiography data reasonably well. The only exception would be the RVCV, in which a larger percent difference was observed. We believe the reason for this occurring could be the smooth shape of the sinus structure that we synthetically generated with pathological data. Indeed, as it was demonstrated by Katayama et al. [73], the RVCV could be sensitive to the morphology of sinuses. We can also observe that the results from a hypertensive case (140/90 mmHg: Δp=50 mmHg) predict a more rapid opening and closing with a higher acceleration as expected.

Table 3-1: Comparison between FSI and echocardiography leaflet dynamics

Normal case (120/80 mmHg: Δp=40 mmHg) and Hypertensive case (140/90 mmHg: Δp=50 mmHg)

	Current model (Normal)	Current model (Hypertensive)	Echocardiography (Normal)	% difference between the normal case and echocardiography
RVOT ms	53	44.6	46.0	14.14
RVOV cm/s	25.7	34.3	29.2	12.75
RVCT ms	52.7	40.1	47.0	11.43
RVCV cm/s	16.3	20.7	23.6	36.59
ET ms	276.0	248.2	329.0	17.52

3.1.1.b Leaflet stresses

The stress patterns on the aortic leaflets are quite complex and vary during the course of the cardiac cycle. This is thought to be caused by the presence of the sinuses which absorb energy during systole and release it during the diastolic phase. However the location at which the maximum stress occurs during systole and diastole seems to be constant. In systole, the maximum stress point in located just below the commissures at the attachment line, while in diastole, it shifts to the commissures. In this section, both the principal and von-Mises stresses are reported and examined quantitatively and qualitatively. The principal stresses in the leaflets were observed at two instants of the cardiac cycle: one at the beginning of systole and the other at mid-systole (0.072 seconds into the cardiac cycle). In each of these moments, a preferential direction of these stresses was noticed in a circular arrangement around the attachment edge of the leaflet. Conversely, stress in the inner area, or belly, of the leaflet was more scattered as shown in Figure 3.3(a). This particular distribution is qualitatively similar to previous reports and known stress patterns on the leaflets [133, 134]. The stress levels were also assessed by comparing them to previously reported values under similar conditions and by selecting similar

point on the leaflets to match those in the previous study of the leaflet stresses during the dynamic actions of the valve by Gnyaneshwar et al. [67]. The locations of the elements sampled for comparison of their stress histories are given in Figure 3.3(b). These particular elements spatially match those from the reference study. The specific values computed for the stress magnitudes at these locations for both models and their percent differences are presented in Table 3-2. For both studies the results of stress values range between 0-1MPa. Additionally, the models are also in agreement as to the locations of the stress minima and maxima. Differences in values ranged from 0.06MPa to 0.15MPa with an average difference of 0.078MPa. The differences observed between the two models could be due to the fact that the model presented by Gnyaneshwar et al. does not incorporate the fluid domain and is strictly structural.

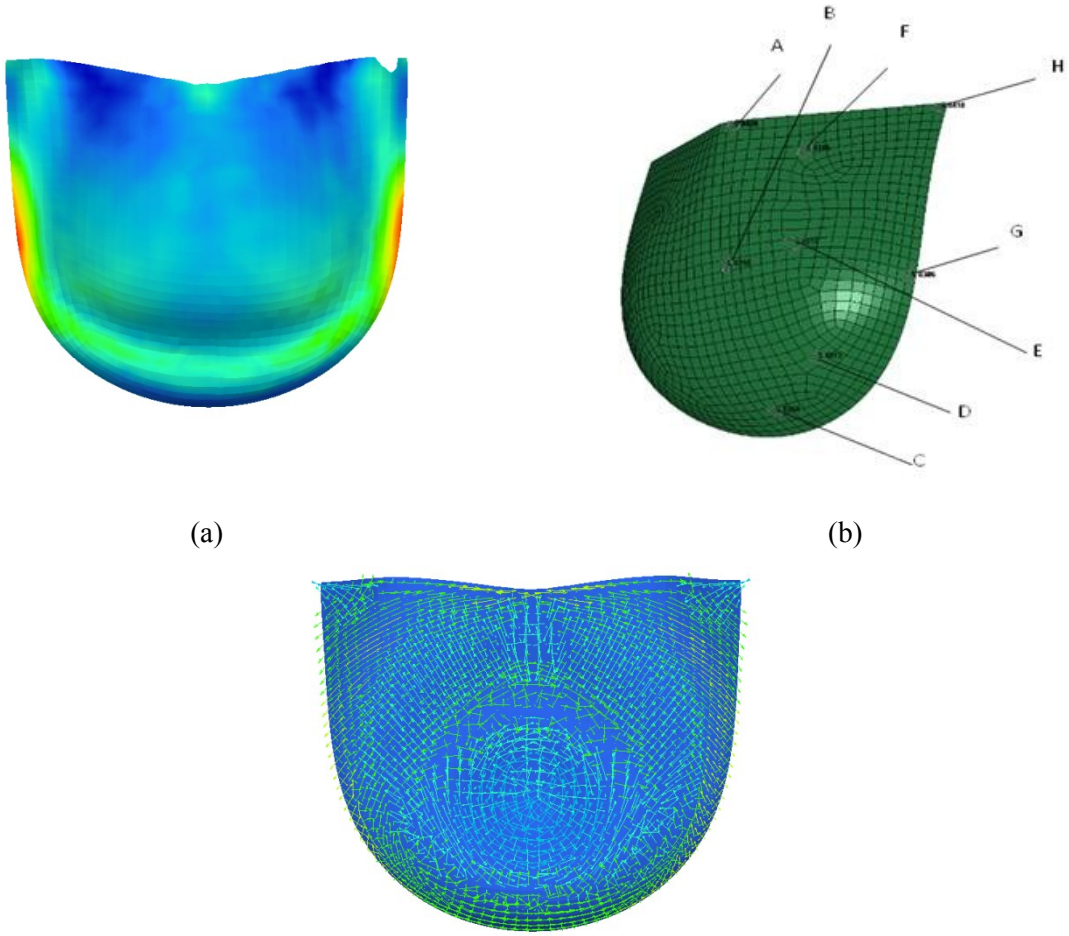

Figure 3.3: (a) Stress distribution on the aortic leaflet during systole and (b) illustration of the selected elements where the von Mises stresses are calculated. Image (c) represents the circular patterns observed in the stress distribution on the leaflets.

Table 3-2: Comparison of the maximum stress (MPa) during the cardiac cycle in selected locations represented in Figure 3.3 (b) between our model and the model by Gnyaneshwar et al.

Location	*Our model*	*Model by Gnyaneshwar et al.*	*% Difference*
A	0.492	0.15	106.54
B	0.311	0.20	43.44
C	0.480	0.42	13.33
D	0.390	0.24	47.61
E	0.380	0.28	30.30
F	0.158	0.13	19.44
G	0.914	0.90	1.54
H	0.478	0.40	17.76

3.1.2 The fluid medium

Verification of the fluid medium results can be accomplished to a certain degree by comparing bulk flow properties of the model to known physiological data and also by searching for known flow patterns such as diastolic recirculation regions, which are known to occur, but are more difficult to quantify. Simulated blood velocities were sampled in the model at three locations: the flow through the valve at the level of the commissures and the sinotubular junction as well as flow through the coronary ostia as shown in Figure 3.4:. For the first two locations, comparison to clinical data can be done over the entire cardiac cycle regarding both the total flow ejected and the temporal distribution of this flow. For the coronary flow, the shape of the waveform is less precisely known, although certain aspects, such as the total flow and the general shape, have been documented.

The computed velocities at the STJ, commissures, left, and right ostia are provided in Figure 3.5: with a peak velocity of 1.58 m/s occurring at 0.093 s, which is in agreement with previous studies that have reported peak velocities of 1.35 ± 0.35 m/s [108]. The fluid exhibits a rapid acceleration followed by a deceleration slightly smaller in magnitude, which is known to be the case physiologically.

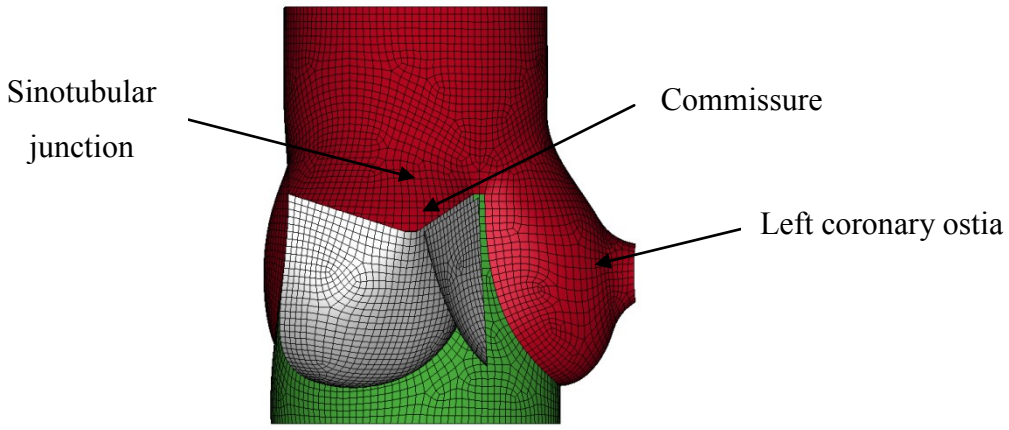

Figure 3.4: Locations at which velocity values were measured

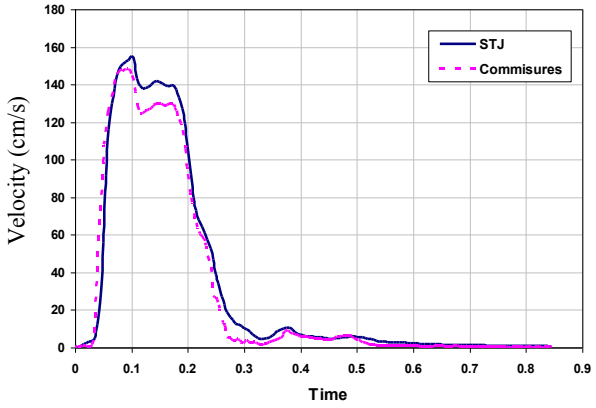

(a)

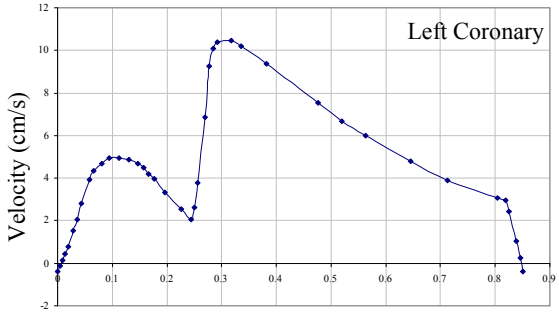

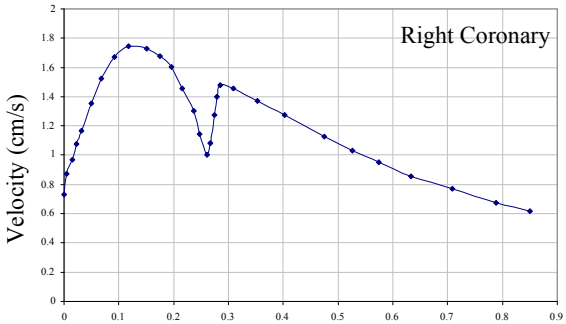

(b) (c)

Figure 3.5: Velocity curves during a cardiac cycle at (a) sinotubular junction and commissure and (b) left coronary ostium and (c) right coronary ostium

The velocities at the sinotubular junction and at the commissural level resemble each other quite closely and during the diastolic phase reach values close to zero as expected. The fact that these locations do not experience negative values of flow is an indication of proper valve closure and approves that backflow into the ventricular chamber does not exist. Coronary perfusion data are also close to the known physiological values with an overall coronary perfusion of 100 mL/min or approximately 4% of the cardiac output. An important hemodynamic factor that is thought to aid coronary perfusion is the formation of vortices in the bulbous sections of the aortic valve (sinus of Valsalva). These vortices are known to occur at the end of systole and become more pronounced by mid diastole and with the help of the elastic recoil from the sinuses push the blood into the coronary arteries. We were able to clearly capture these vortices around the tip of the leaflets in our model especially at the beginning of the diastolic phase.

In order to investigate the effects of aortic valve pathologies on coronary flow, the aortic wall elastic modulus was increased from 3.34MPa to 60MPa and the thickness of the aortic valve leaflets from 0.05 to 0.1 cm to simulate aortic stiffening and calcific aortic stenosis, respectively [135, 136]. Twenty-nine and eight different values were used for aortic wall stiffness and leaflet thickness, respectively. These results revealed an interesting phenomenon and connection between aortic pathologies and coronary perfusion. As shown in Figure 3.6:, elastic modulus of the aortic wall was increased to a higher value compared to their normal state, which caused a significant drop in coronary peak velocity after a threshold. This drop could be correlated to the decrease in coronary flow reserve (CFR) previously described in clinical studies [88, 137]. Aortic distensibility is a major determinant of left ventricular afterload [88]. Any deterioration of aortic distensibility (i.e., aortic stiffening) will result in ventricular-arterial mismatch and left ventricular dysfunction, which may prove critical in certain stages of the disease.

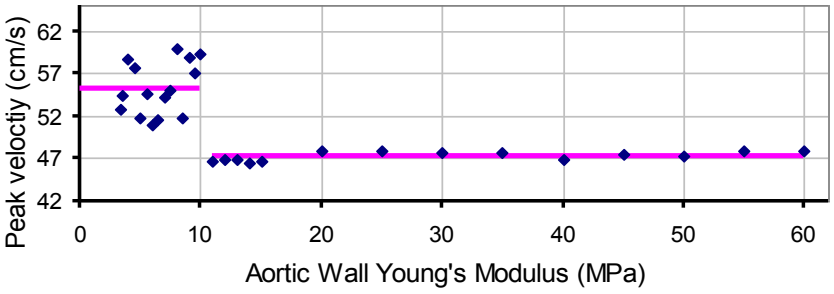

(a)

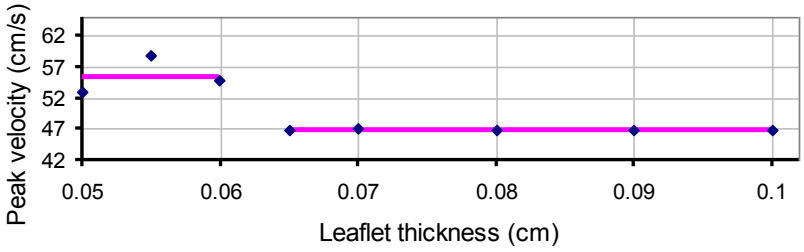

(b)

Figure 3.6: Behaviour of coronary peak velocity as a function of varying (a) aortic wall stiffness and (b) leaflet thickness

Aortic stiffening may lead to an early return of the reflected arterial pulse wave causing an increase of systolic blood pressure (SBP) and a decrease in diastolic blood pressure (DBP), thus increasing the pulse pressure. Greater SBP increases myocardial oxygen consumption, reduces left ventricular ejection fraction, and increases left ventricular afterload inducing left ventricular hypertrophy. Myocardial blood supply depends largely on pressure throughout diastole and the duration of diastole, so the decrease of DBP can compromise coronary perfusion resulting in subepicardial ischemia. Moreover, left ventricular hypertrophy also reduces coronary flow [88]. These results showed that below a value of aortic wall elastic modulus being equivalent to three times its normal value, the peak coronary velocity remained constant. This observation could be correlated to the beneficial effects of smoking cessation, exercise, and diet on arterial compliance. Oren et al. [138] revealed, in a clinical study in 2006, that smoking cessation for 6 months significantly improved arterial stiffness. Oscillatory compliance rose from 0.051 ± 0.023 to 0.063 ± 0.03 $mm^2/mmHg$, which corresponds to an increase of 23%. A short time of smoking cessation has a strong effect on the arterial compliance. Exercise also plays an important role on arterial compliance recovery too. Tanaka et al. [139] determined the role of

habitual exercise on age-related decrease in central arterial compliance. They demonstrated that arterial compliance fell from about 0.02mm^2/mmHg in sedentary healthy young subjects to values of about 0.012 to 0.013mm^2/mmHg in middle-aged and older sedentary humans. But in the highly trained middle-aged and older subjects (on a 3-month exercise period), exercise appeared to reduce the decline in compliance with aging by about 50%. Again a short time of regular exercise has a strong effect on the arterial compliance. Finally diet also has a strong effect on arterial compliance. Nestel et al. [140] studied the impact of eating fish and fish oil on systemic arterial compliance during 4 weeks in fifteen obese people. They showed that the systemic arterial compliance improved significantly by about 85%. Consequently, the combined results of Oren et al. [138], Tanaka et al. [139], and Nestel et al. [140] showed that a short period of smoking cessation, regular exercise, or diet may improve the peak coronary velocity and therefore re-establish a good coronary perfusion.

The increase of aortic valve leaflet thickness (modeling sclerosis and resulting in aortic stenosis) also led to a decrease in coronary peak velocity. Above a certain threshold, a marked drop in peak velocity also occurred. These results were again in agreement with previous studies [86, 141]. In patients with calcific aortic stenosis and a normal coronary angiogram, the CFR is significantly lower [136]. The CFR capacity of the coronary arteries depends on at least three main components: (1) micro- and macrovascular resistance, (2) myocardial resistance, and (3) the effect of solid viscosity [142]. In some pathologic conditions like aortic stiffening and calcific aortic stenosis, changes in one or more of these factors may lead to an impairment of the CFR capacity. It is known that aortic compliance is reduced as the cardiac tissue becomes aged and pathological [143]. Indeed, recently it has been shown that a stiff aorta is associated with a reduction in coronary blood flow [137, 141, 144]. However, there is little information relating coronary flow and aortic stiffness in humans [145]. An explanation for the drop in coronary flow observed in our simulation could be linked to the fact that 70 – 90% of the coronary perfusion occurs during diastole [146, 147] and also the fact that it is during this phase that blood is driven towards the coronary arteries by the elastic recoil of aorta (Windkessel model) [148]. This elastic recoil is the potential energy stored in the walls during systole and released during diastole to aid leaflet closure and blood perfusion through coronaries. Approximately 50% of the stroke volume is directly forwarded to the peripheral circulation [149]. Peripheral resistance and elastic extension of the aortic wall are responsible for storage of the remaining stroke volume, the

storage volume [150]. Reduction in aortic compliance will induce an increase on the impedance to the ventricular ejection which will lead to a decrease in coronary flow [151]. For a less compliant aortic wall, the impact of the reduction in elastic recoil would be direct as less energy is stored in the wall during systole. As for the case where the leaflets have thickened, this loss in the potential energy could be linked to the increase in blood velocity through the valves (due to reduction of effective orifice area) and the associated increased pressure drop. In that context, we believe that the hydraulic resistance and the vessel compliance could compound to produce the observed sudden drop in the perfusion. However it should be noted that since the inlet boundary condition at the ventricular level is considered to be the pressure difference between the ventricle and aorta, the aortic wall will experience a smaller pressure, specifically during mid-systole. As a result aortic root expansion will be reduced, which could affect the leaflet opening and closing pattern. The percentage difference observed for RVCV could also be due to this reduced expansion and loss of distensibility in the sinuses. This assumption might cause the drop observed in the coronary perfusion to have a minor shift across the range of wall stiffness and leaflet thickness studied.

Another interesting clinical aspect that was investigated was the location of the ostia on the sinuses and the possible impact that it might have on coronary flow. As explained in section 2.1.1, the height at which the ostia can be positioned on the sinuses can vary due to the existence of congenital pathologies or as a consequence of re-suturing procedures involved in surgical operations such as remodelling or re-implantation. Three different geometries of the aortic valve model shown in Figure 2.3 were used to investigate such geometrical variations. The material properties and boundary conditions used were the same as the normal model of the aortic valve explained in sections 2.4.2 and 2.4.3, respectively. The results were focused on the average flow variations in the coronary ostia due to the isolated variable (since all other parameters are kept constant) of their positioning on the sinus structures.

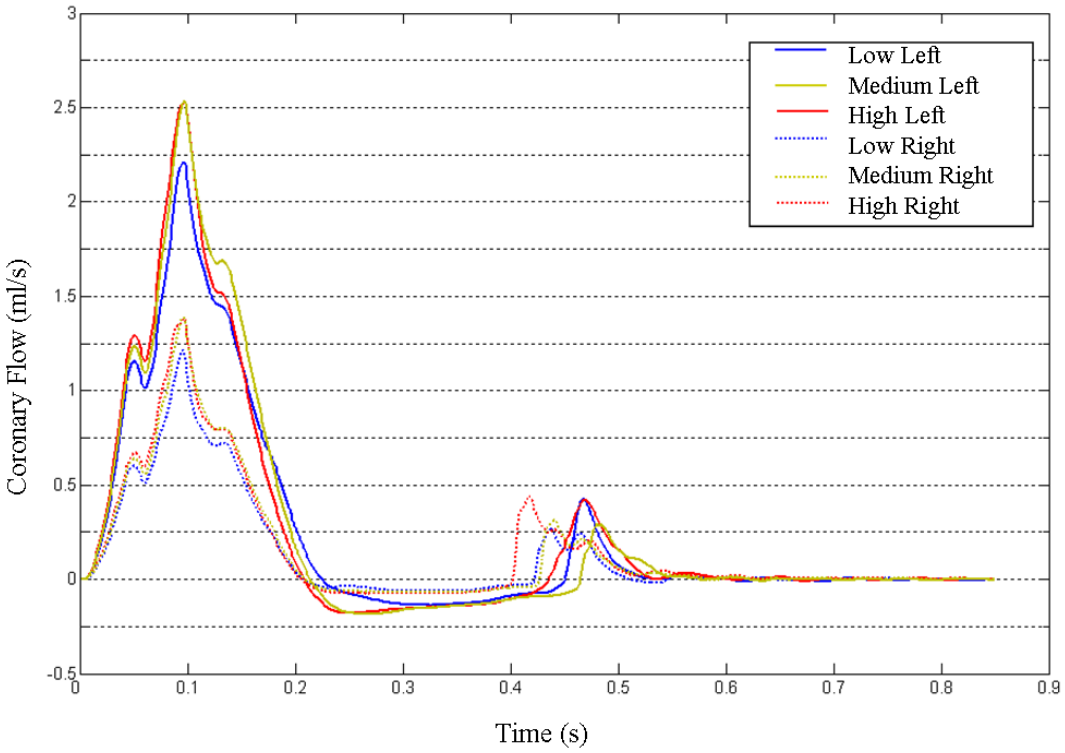

Figure 3.7: The impact of coronary ostia location on Coronary flow

The results revealed minor differences in the coronary flow among the three models. The model in which the location of ostia was at the highest (closest to normal physiological location) introduced the maximum amount of flow into the coronary ostia as shown in Figure 3.7. It should be noted that the model with the medium ostia location experiences very similar values of flow throughout the cardiac cycle as well as similar values for peak flow. However, the average flow during the entire heart beat is approximately two percent less than the high ostia model. On the other hand, the low ostia model seems to experience smaller values of peak as well as average flow compared to the other two models. Even though coronary autoregulation—the intrinsic ability to maintain a constant blood flow despite changes in perfusion pressure—might mitigate some of this interaction [87, 152, 153] in a first approach, in order to simplify the analysis, autoregulation was not incorporated into the model.

3.2 Global model of the aortic valve

Similar to the previous section, the results of the global model of the aortic valve have been divided into two sections. The first section represents results concerning the tissue via the solid medium and the other corresponds to the blood via the fluid domain. The addition of the coronary arteries allow extracting more hemodynamic data related to the coronaries such as velocity profiles and shear stress along these structures. Moreover, the results related to coronary perfusion can be re-evaluated using coronary flow measurements more downstream of the ostia outlets. However, simulation of such complex system can generate a significant amount of temporal and spatial data such as the stress and strain in the cardiac tissue as well as pressure and flow for the fluid within the three-dimensional domain. Since one of the main objectives of this work includes investigating the relation between aortic valve pathologies and hemodynamic of coronary arteries, most of the results presented in the following sections are in order to shed some light on this matter. Different degrees of aortic sclerosis were investigated using a variety of cardiac tissue thicknesses and stiffnesses for the aortic wall as well as for the leaflets. The results of the solid domain have been reported in the next section followed by the results from the fluid domain.

3.2.1 The solid domain

Clinical metrics representing the opening and closing pattern of the leaflets such as rapid valve opening time (RVOT), closing time (RVCT), and their corresponding velocities (RVOV and RVCV) are used on a routine basis in clinical practice using echocardiography to evaluate the outcome of different surgical procedures or different prosthetics [48, 113, 131, 154]. These parameters were calculated in section 3.1.1.a for the normal base model of the aortic valve and are represented in Table 3-3 below for comparison. Values for the normal global model of the aortic valve as well as for severe pathological models of aortic wall and leaflet stiffening and thickening are calculated. The values used to model tissue stiffening and thickening were four times greater than their corresponding normal values. Results from these simulations are compared to average reported echocardiography values and presented in Table 3-3.

Table 3-3: Rapid valve opening and closing velocities and times for the healthy model, pathological models and their corresponding average values from echocardiography

	Rapid Valve Opening Time (ms)	Rapid Valve Opening Velocity (cm/s)	Rapid Valve Closing Time (ms)	Rapid Valve Closing Velocity (cm/s)	Ejection Time (ms)
Base normal model	53	25.7	52.7	16.3	276.0
Global normal model	51	26.3	45	19.4	283
Echocardiography values	46.0 ± 11.3	29.2 ± 8.7	47.0 ± 11.1	23.6 ± 7	329 ± 49
Aortic wall stiffening	43	27.85	70	15.05	291
Aortic wall thickening	50	28.34	73	14.67	289
Leaflet stiffening	30	28.16	94	9.23	257
Leaflet thickning	28	19.2	81	9.11	234

The first obvious observation that can be drawn from the table above is the improvement of valvular dynamics in the global model compared to the normal base model of the aortic valve. Leaflet morphology values calculated for the global model compare better to the physiological values measured by echocardiography. This is an important message which shows that a more global model of aortic valve structure could potentially improve the obtained results compared to a more localized study. Applications of boundary conditions more downstream and further from the valvular structure allows for a more physiological establishment of hemodynamic variables.

Moreover, values were also calculated for severe pathological conditions of aortic sclerosis to better understand how each of these pathologies affect the leaflet dynamics and the global hemodynamic in the aortic root. Pathologies of the aortic leaflets seem to have a greater effect on valvular dynamics compared to pathologies of the aortic root while leaflet thickening seems to be the most drastic of all. Pathologies of the aortic wall affect the compliance of the

cardiac tissue in this region. The aortic wall has an intrinsic behavior during the cardiac cycle that is referred to as the "elastic recoil". During systole, this elastic recoil stores some of the bloods kinetic energy in the sinus walls and the aortic wall. This energy is then released during diastole to aid leaflet closure and blood perfusion through coronaries. Therefore any variation to the cardiac tissue compliance whether by an increase in stiffness or thickness will affect this elastic recoil. The advantage of using a global FSI model is that variations to the regional hemodynamic due to changes in elastic recoil (the tissue portion of the model) can be captured and assessed. The effect of the elastic recoil is more evident by following the rapid valve opening and closing times for the wall stiffening and thickening cases. These parameters have marginal impact on the opening characteristics of the leaflets but greatly affect the closing times and velocities compared to the normal state.

As for the leaflet pathologies, the same clarification can be used to explain the observed variations in the desired clinical metrics. However, there is a secondary factor that should be considered which involves the opening and closing patterns of the leaflets. The compounding effect of the elastic recoil and leaflet tissue stiffness/thickness is even more pronounced on these clinical indices. This factor can be better visualized with a side by side comparison of the leaflet opening and closing patterns of the normal and the pathological cases as presented in Figure 3.8 below. The opening and closing patterns of the normal aortic valve has been depicted on the left side while a severe wall thickening and leaflet stiffening have been shown in the middle and right column, respectively. The instances that depicted critical moments during a cardiac cycle were chosen to show the difference in leaflet morphology among these three models. Simulation results after 0.27 seconds into the cardiac cycle are not displayed because little variation is observed in leaflet dynamics.

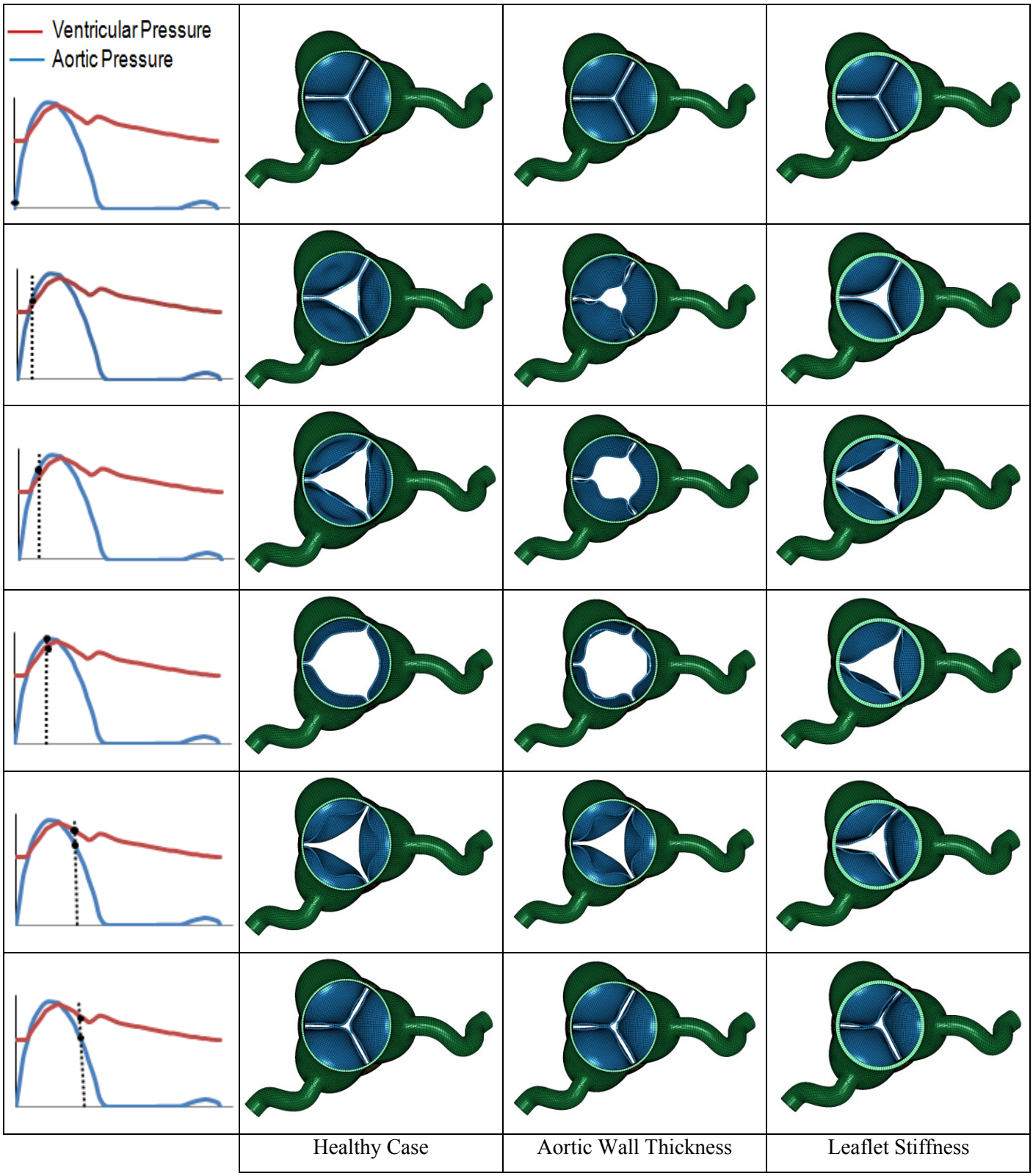

Figure 3.8: Leaflet dynamics comparison between normal, severe aortic wall thickening and leaflet stiffening

The results for the healthy case in terms of global leaflet tip movement, bulging of the leaflet belly and also the triangular valve orifice are similar to what has been observed in pulse duplicator and previous studies [53, 154-156]. Interestingly, the opening and closing patterns of the leaflets vary significantly according to the type of pathology studied. In the case where the aortic wall thickness has increased, an apparent fluttering effect can be observed especially during systole. This could be related to the fact that the extra thickness of wall tissue prohibits the sinus and commissural sections of the aortic root to expand to their normal range. As the valve opens during systole, the commissural expansion aids in maintaining the leaflet edges straight and stretched, as shown in Figure 3.9. If the aortic root loses its distensibility, each free margin is going to become redundant which is easily visible in the case of aortic wall thickening.

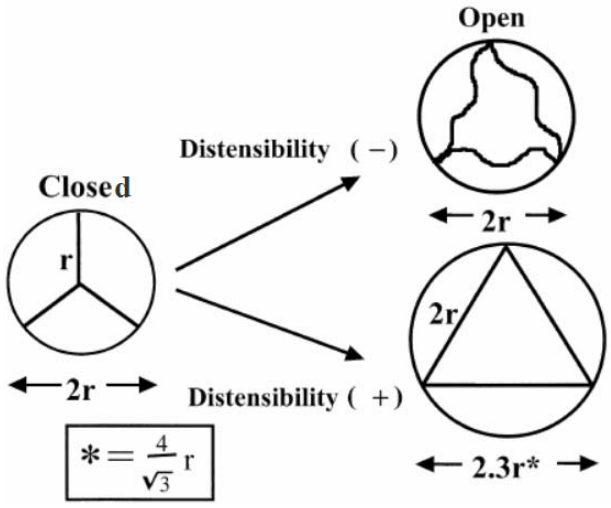

Figure 3.9: Schematic drawing of the impact of aortic root distensibility on leaflet free margins [157]

In the case of leaflet stiffening, the opening patterns during systole are, in a qualitative manner, marginally changed while the closing patterns during the diastolic phase are more affected in comparison to the normal case. Moreover, the geometric orifice area is significantly reduced (a maximum of 58% in mid diastole) during the entire cardiac cycle due to the stiffer leaflets resembling calcified leaflets restricting the blood flow into the ascending aorta. In order to quantitatively measure variations in the opening and closing patterns of the aortic valve leaflets, leaflet displacements were investigated for the four pathological models. A comparison of the circumferential displacement of leaflet tip for the healthy and pathological cases has been presented in Figure 3.10.

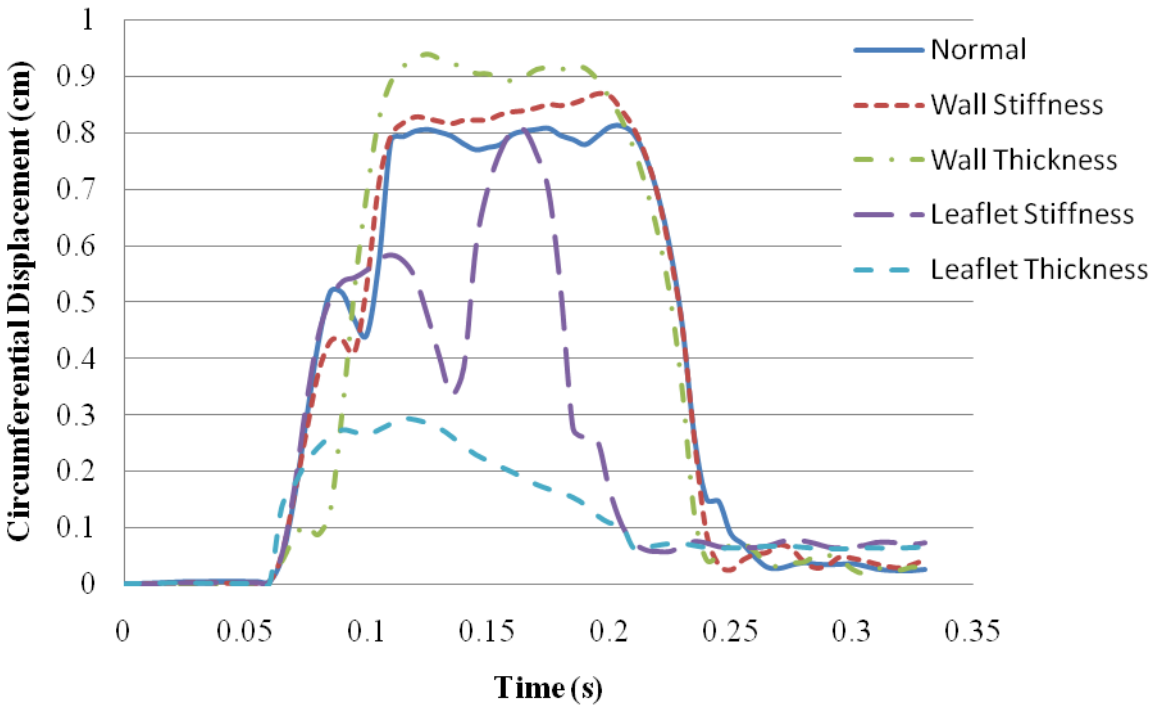

Figure 3.10: Comparison of leaflet tip circumferential displacement between the healthy and pathological cases.

Variations to aortic wall properties seem to have moderate impact on leaflet tip displacement. However it should be noted that due to the fluttering effect described earlier, the tip of the leaflet as well as its free edge undergo more complex bending patterns. This behavior can be seen in Figure 3.10 where the leaflet tips have an initial delay in the opening phase (0.08 s into the cycle) followed by a more rapid acceleration. In the pathological cases the leaflet tip undergoes more displacement compared to the normal case due to this acceleration and the placating free edges. However, leaflet tip displacement/location should not be confused with the maximum geometric orifice area. In pathological cases, as observed in Figure 3.10 and Figure 3.8, the leaflet belly becomes the cross sectional point at which the blood flow is restricted on these structures since the leaflet tips have been bent over towards the sinus cavities. Results revealed that leaflet thickening has the highest degree of impact on leaflet tip displacement and causes a significant reduction in the outlet surface area of the aortic valve. A reduction in GOA was observed in most pathological cases, with a maximum of 85% in the case of severe leaflet thickening. Such severe obstructions cause a significant reduction in blood flow into the

ascending aorta and the coronary arteries. The next section will show such impacts on the global and local hemodynamic of aortic valve region.

3.2.2 Fluid domain

As a first step, blood velocity was measured at three critical cross sections in the model. These are velocities at the level of sinotubular junction, downstream of the right and left coronary arteries. The STJ cross section was chosen to be just above the leaflets, similar to the location depicted in Figure 3.4 for the normal aortic valve model. However, due to the inclusion of the coronary arteries velocity measurements in these structures can be performed more downstream of the ostia and further from the location where the boundary conditions were previously applied. Therefore blood velocity in these arteries was calculated just before the initial curvature to eliminate the additional effect of curvature on velocity calculation. A peak velocity of 1.64 m/s occurred at 0.1s into the cardiac cycle, during systole at the STJ level which is in agreement with previous studies that have reported peak velocities of 1.35 ± .35 m/s [108, 158].

As for the coronaries, a maximum velocity of 36 cm/s and 21 cm/s were calculated during diastole in the left and right artery respectively [159, 160]. The temporal blood velocity graph at the sinotubular level as well as flow in the left and right coronary arteries have been shown in Figure 3.12. The measured values and their temporal trend during a cardiac cycle are in agreement with the average clinical observations. The maximum flow in the left coronary occurs during diastole as expected, however the blood flow during systole seems higher than normal physiological values. This is partially due to the assumptions made in the boundary conditions in our model. In addition, during the systolic phase of the cardiac cycle, coronary arteries are contracted due to myocardial contraction which has not been included in our model which causes impediment in the coronary arterial inflow. This will be discussed more in detail in the limitations section.

Similar to the normal base aortic valve model, formation of diastolic recirculation zones (vortices) was investigated and their presence was confirmed as shown in Figure 3.11.

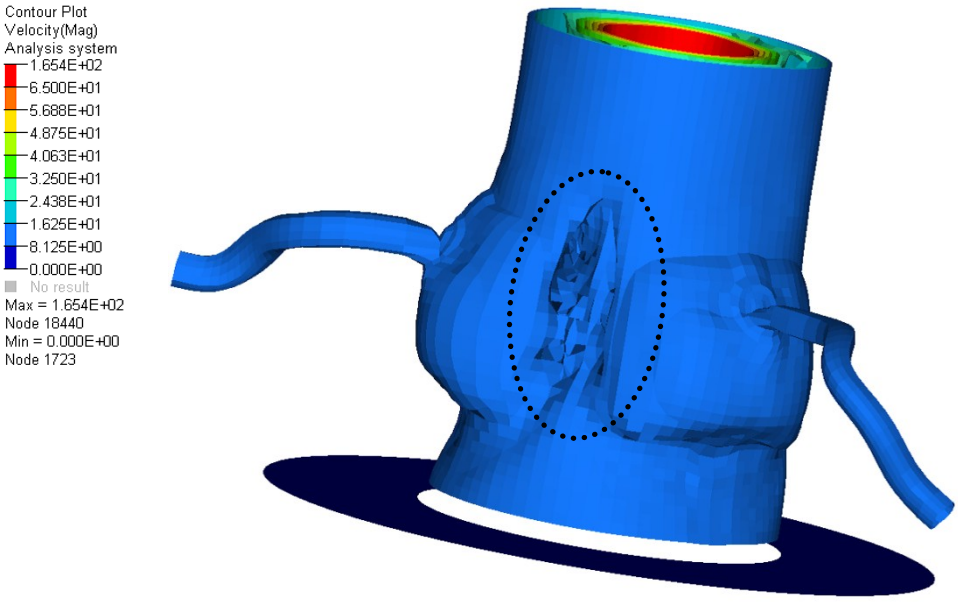

Figure 3.11: Diastolic recirculation zones (circled with dashed line) captured in the global model of the aortic valve

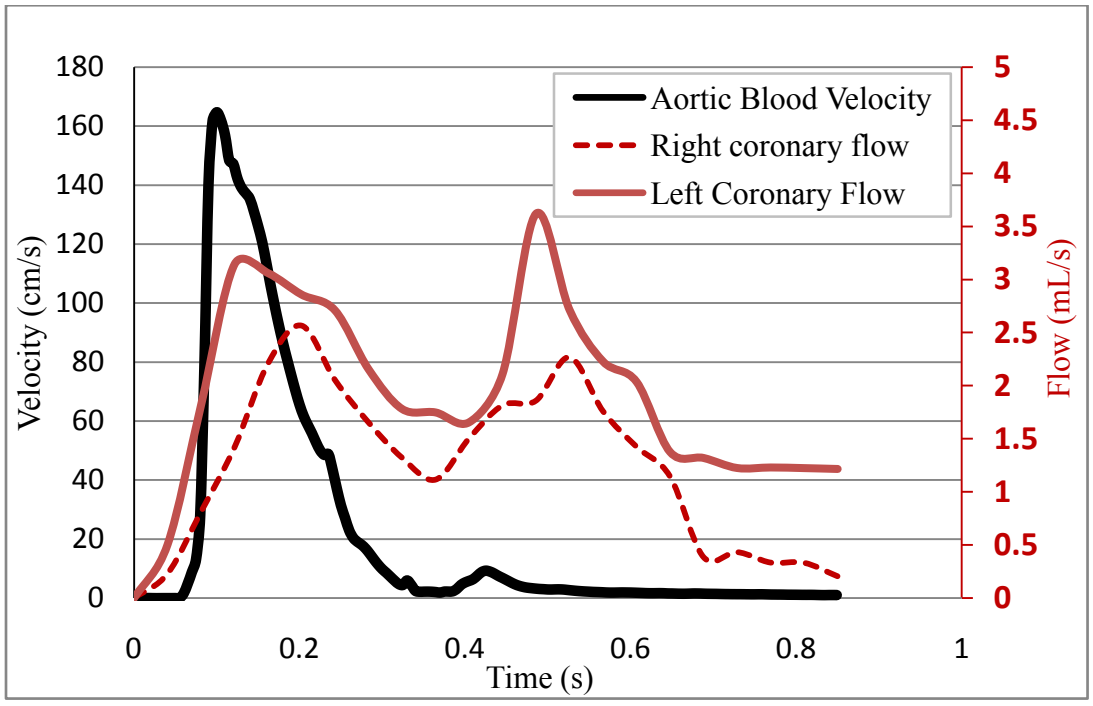

Figure 3.12: Aortic velocity and coronary flow measurements in the healthy model

The addition of the two coronary arteries allows investigating the inter-relation between the aortic root region and the hemodynamics of the coronary arteries. Coronary flow reserve and aortic stiffness/thickness have been recognized as individual clinical indices and risk factors in coronary artery disease and as prognostic tools for cardiovascular disease and can be measured simultaneously with transesophageal echocardiogram [137, 161]. There have been several recent clinical studies as well as numerical investigations that have looked into the possible relation between these parameters [75, 76, 162-164]. However, there is a lack of clear explanation of the biomechanical factors and the underlying mechanism that would lead to this interaction. Since, the main objective of this study is to investigate the effect of aortic pathologies on the velocity profile and shear stress in the coronary arteries as well as coronary flow, values of aortic wall and leaflet stiffness and thickness have been varied to values corresponding to normal and moderate/severe tissue sclerosis. In order to examine the impact of such pathologies, five cross sections along each coronary artery are selected creating a total of ten cross sections along both coronaries. These cross sections were chosen at similar intervals along these arteries and have been shown in Figure 3.13.

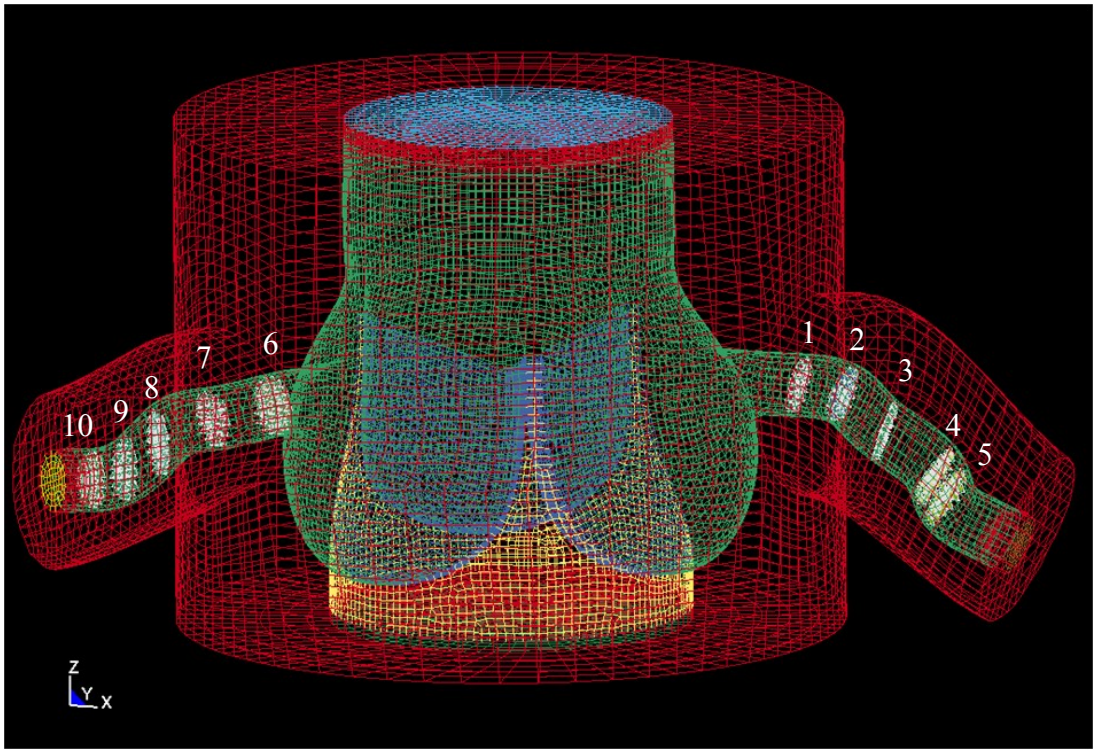

Figure 3.13: Cross sections at which velocity profile are calculated along the coronary arteries and the corresponding numbering system used for identification

Velocity profiles are obtained along these arteries at the specified cross sections (CS) in Figure 3.13 during the diastolic phase where coronary flow is maximal. Velocity profiles are calculated for three cases including the normal global model; and two pathological cases: aortic leaflet and aortic wall stiffening. In each of these pathologies, the aortic leaflet and aortic wall stiffnesses are increased by 50%, 100% and 160% to reach their thresholding critical values that resulted in the observed drop in the coronary flow and to study their impact on coronary velocity profiles. Figure 3.14 represents a comparison of the velocity profile between the normal case and the three pathological cases of aortic leaflet stiffening at 0.48s into the cardiac cycle. A similar comparison was performed for pathological cases of aortic wall stiffening as shown in Figure 3.15. The orientation of the 2D plane on which these velocity profiles have been calculated varies with the curvature of the coronary arteries. In other words, rotation of this plane around the axis of these structures is prohibited. This allows depicting the impact of geometrical variations such as curvature on the calculated velocity profiles since the points chosen on each cross section for velocity measurements remain constant along the arteries despite their curvature.

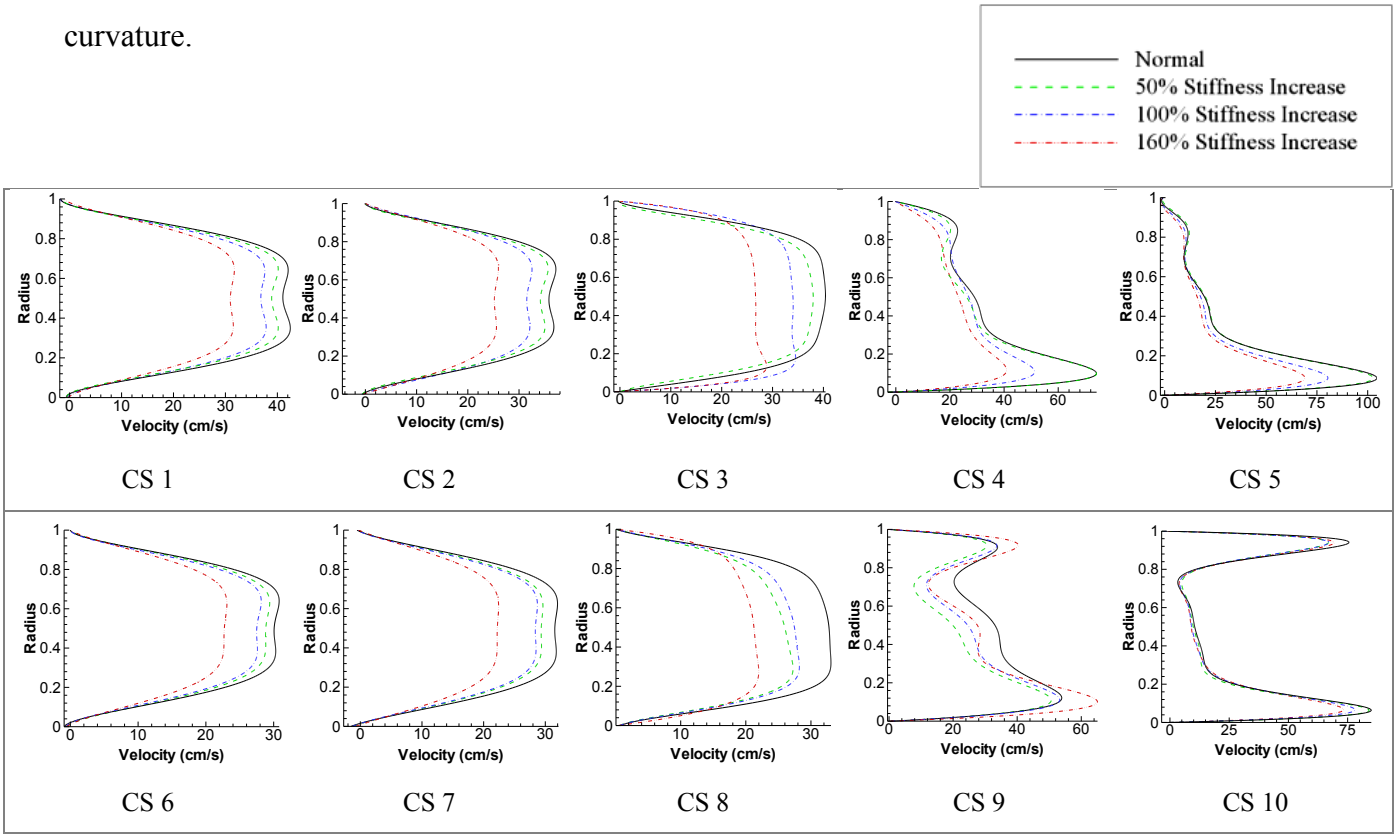

Figure 3.14: Comparison of velocity profiles along the left and right coronary arteries between normal and aortic leaflet stiffening at the corresponding cross section (CS).

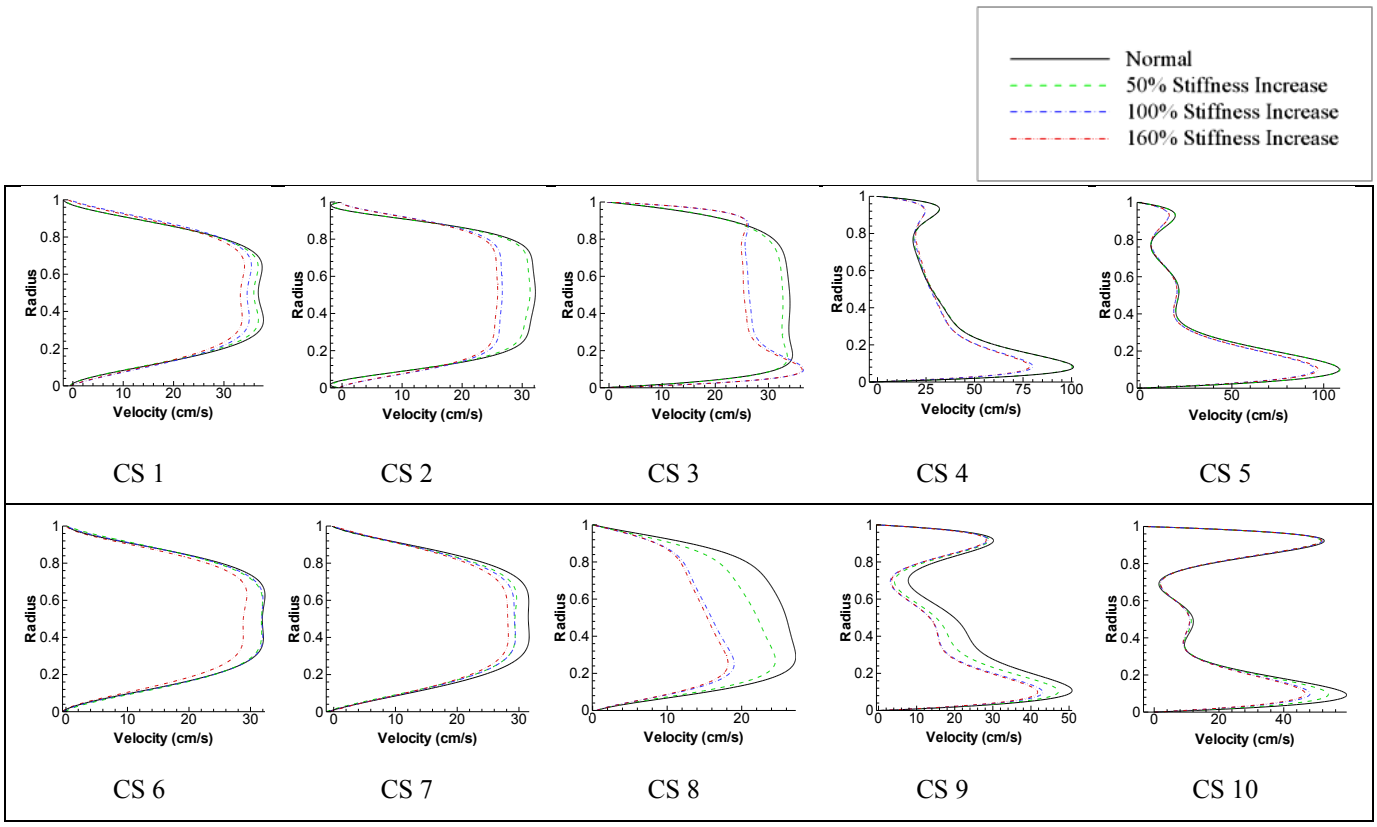

Figure 3.15: Comparison of velocity profiles along the left and right coronary arteries between normal and aortic wall stiffening at the corresponding cross section (CS).

Results revealed a continuous decrease in the maximum as well as average cross sectional velocity with the progression of the disease. These findings confirm the clinical observation made by other researchers [137, 161-167]. In the case of leaflet stiffening, velocity profile variations from the normal case seem to be minor except for the model with 160% increase in stiffness. At this stage, there is an apparent decrease in blood velocity measured across the arteries which is in agreement with the findings from the normal base model. If one recalls, an approximate thresholding value of about three times the initial leaflet stiffness caused a significant drop in coronary flow. On the other hand, increase in aortic wall stiffness seems to have a more pronounced impact on coronary velocity profiles. A substantial decrease in velocity is observed once the aortic wall tissue stiffness reaches twice its normal values. Variations in velocity profile are enhanced due to the combined effect of coronary curvature and the degree of pathological conditions. As can be seen from Figure 3.14 and Figure 3.15 at the initial cross sections (first and sixth) where there are no apparent curvatures, the velocity profiles are more uniform and similar in the right and left coronaries. The decrease in the maximum velocity is not

necessarily linear with the advancement in the degree of pathology. However, in the most downstream three cross sections in either artery (CS 3, 4, 5 and CS 8, 9, 10) due to the existing abrupt curvatures the observed patterns in the velocity profiles change. These curvatures seem to have a significant impact on the location and magnitude of the maximum variations from the normal model. As the radius of curvature decreases we observe that the maximum velocity shifts towards the outer curvature [168] while a secondary peak is created along the inner side of the curvature [169].The formation of secondary flows in coronary arteries is due to the fact that when blood flow enters a curvature, it is forced to follow the bend. This leads to development of radial pressure gradient between the inner and the outer walls of the curvature. The imbalance between radial velocity gradient and the centrifugal force results in a secondary flow creation. As a consequence the axial velocity profile becomes more skewed towards the outer wall. This is in agreement with clinically observed atherosclerosis-prone regions of coronary artery disease. It also brings us to another important finding which is variations in wall shear stress.

Wall shear stress is the frictional force exerted on the endothelial surface of the vessel wall by blood flow. Shear stress is a critical factor in maintaining normal physiological characteristics of the vasculature. It is proven that chronic exposure of endothelial cells to low or oscillatory shear stress promotes atherosclerotic lesion initiation, progression and could eventually lead to plaque build-up [170-172]. Therefore, it is of great importance to study the effect of valvular pathologies on coronary wall shear stress. Such investigations, in the context of a global model, were neither possible with the normal base aortic model nor with the previously developed models by other research groups due to the absence of coronary anatomy. Using the velocity measurements calculated above, shear stress experienced by the coronary arteries was calculated for the normal, aortic wall and leaflet stiffening models. Due to the difference in velocity measurements between the inner and outer side of a given curvature, the shear stress was calculated at the two points resulting from the intersection of the coronary artery cross section and the 2D plane used to plot the velocity profiles. These points represent the top and bottom locations of the velocity profile plots corresponding to the normalized diameter of 1 and 0, respectively. Figure 3.16 represents shear stress measurements along the coronary arteries at each cross section for the normal and pathological cases.

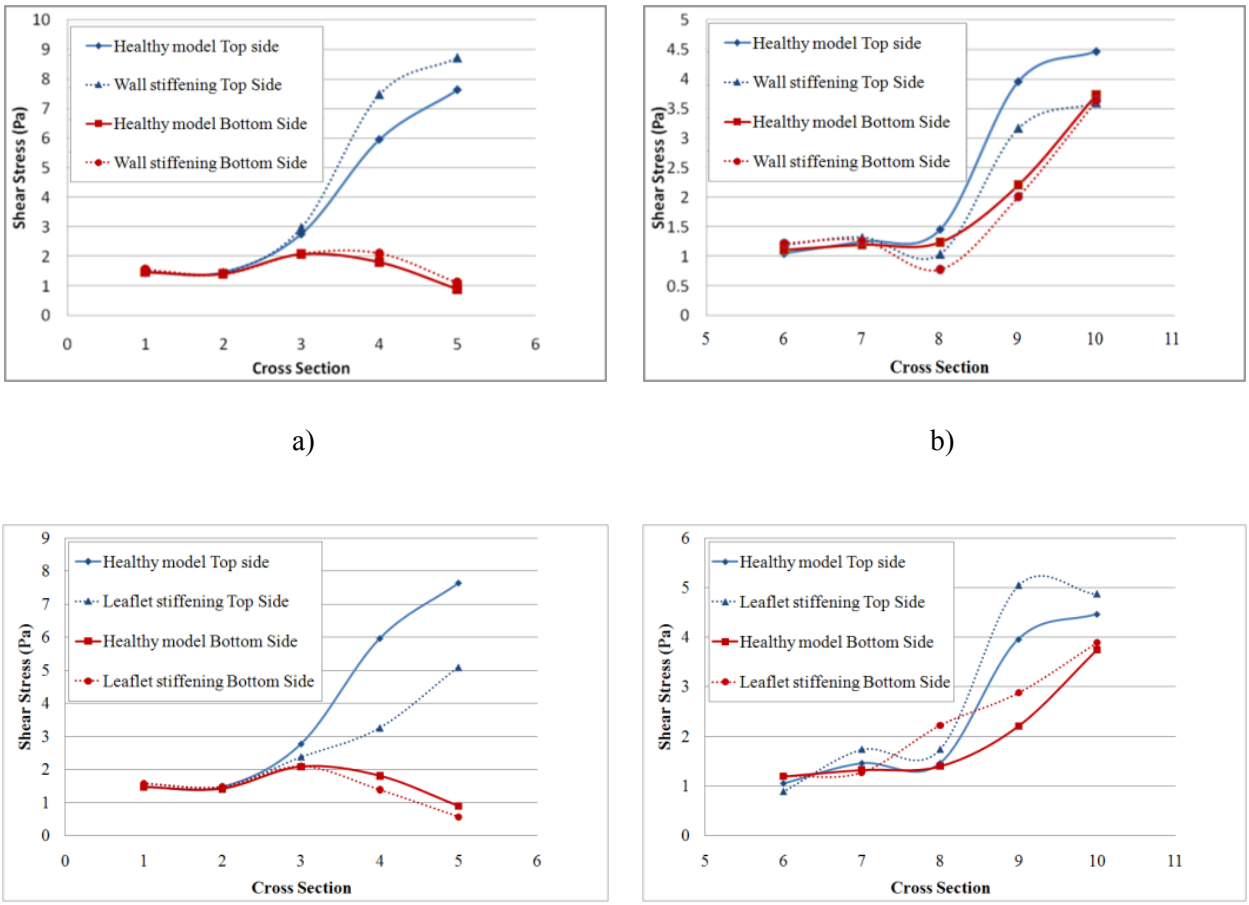

Figure 3.16: Shear stress variation at the selected cross sections for wall stiffness in a) left coronary, b) right coronary, and leaflet stiffness in c) left coronary, d) right coronary

As shown in Figure 3.16 aortic root pathologies have direct impact on the shear stress levels experienced by the vessel wall. This variation, either an increase or a decrease from the normal physiological values, represents approaching the vicinity of the atheroprotective levels for the endothelial cells. This phenomenon in long term could potentially lead to the initiation of coronary artery disease and if combined with an existing one, it could accelerate the progression of the disease. A more detailed analysis of shear stress is required for clinically relevant conclusions. This will be discussed in the limitations section of this work.

Coronary flow was also investigated to study its concurrent effects on the regional sclerotic pathologies of the aortic root. We explored a range of values for tissue thickness and stiffness varying from their normal physiological value up to three times for tissue stiffness and six times for tissue thickness. These percentages of increase were chosen according to the results obtained from the normal base model. The range of variation in tissue thickness and stiffness were chosen so that they would expand beyond the thresholding limit observed in the normal base model. Figure 3.17(a) and (b) represent the effect of tissue stiffness and thickness observed on the maximum flow in both coronary arteries during diastole.

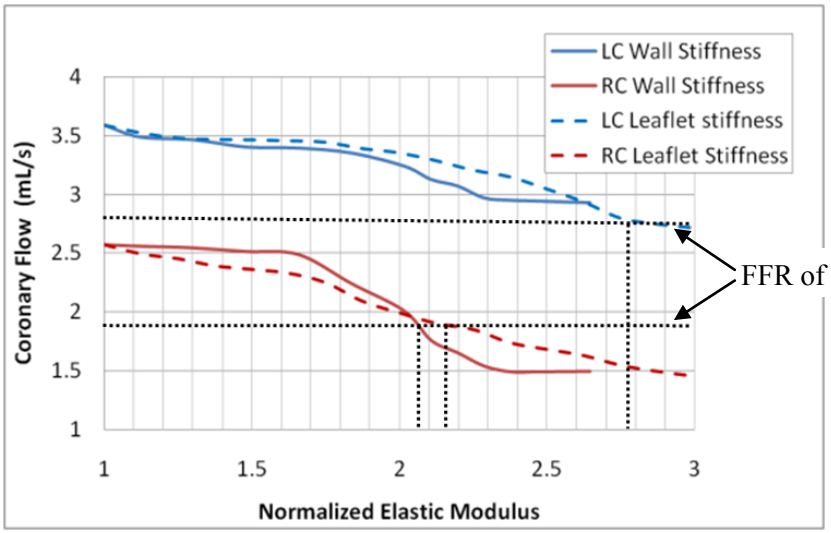

(a)

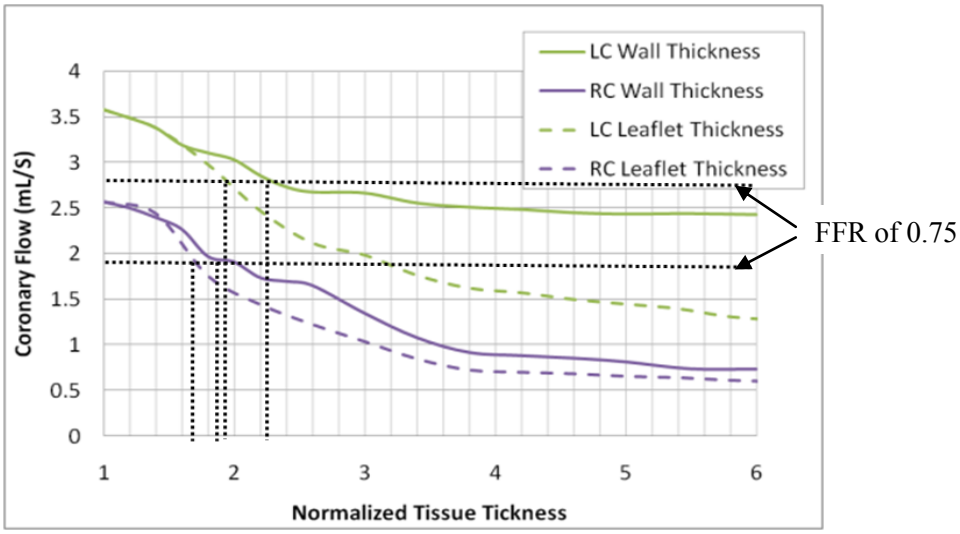

(b)

Figure 3.17: Coronary flow variations due to pathological cases of cardiac tissue a) thickening and b) stiffening

A more continuous drop in the flow in both arteries was observed as a function of the degree of obstruction compared to the perfusion levels in the normal base model in section 3.1.2. A fractional flow reserve (FFR) of 0.75 has been clinically used as a cutoff point for considering surgical revascularization versus drug therapy in patients [173]. The black dotted lines in Figure 3.17 correspond to a FFR of 0.75. This cutoff value corresponded to an approximate increase of 100 % and 200% in the initial values of cardiac tissue thickness and stiffness, respectively. Variations in tissue stiffness and its impact on coronary flow can be explained by the reduction in tissue compliance which eventually leads to alterations in the elastic recoil of the vasculature. Pathologies leading to tissue stiffening would have a significant impact on the energy storing capabilities of the cardiac tissue during diastole. The FSI nature of this study allows capturing this impact on leaflet closure and coronary perfusion. Variation in tissue thickness has a similar influence on the global hemodynamics while it was observed that leaflet thickening had the highest impact on the coronary flow compared to other pathologies. The decrease in the flow starts at an earlier stage of the disease and follows a more accelerated pace. An increase in blood velocity through the valves (due to reduction of geometric orifice area) and an associated pressure drop is observed in this kind of pathology. This is due to the fact that geometric orifice area is greatly affected by the increase in tissue thickness especially in the leaflet area since this impact is direct on the GOA. It is interesting to note that the drop in coronary flow is less sudden compared to the normal base model presented in Figure 3.6. However, the rate of reduction in coronary flow increases near the critical thresholding values of tissue thickness and stiffness (between 2 – 3 times their normal values).

3.3 Pathological global model

Results obtained from the pathological global model mainly focus on comparison of valvular dynamics and stresses imposed on the leaflets and aortic wall between different degrees of coronary occlusion. As a first step, commissural expansion in the course of the cardiac cycle was calculated and compared to previously measured values for the normal global model as shown in Figure 3.18.

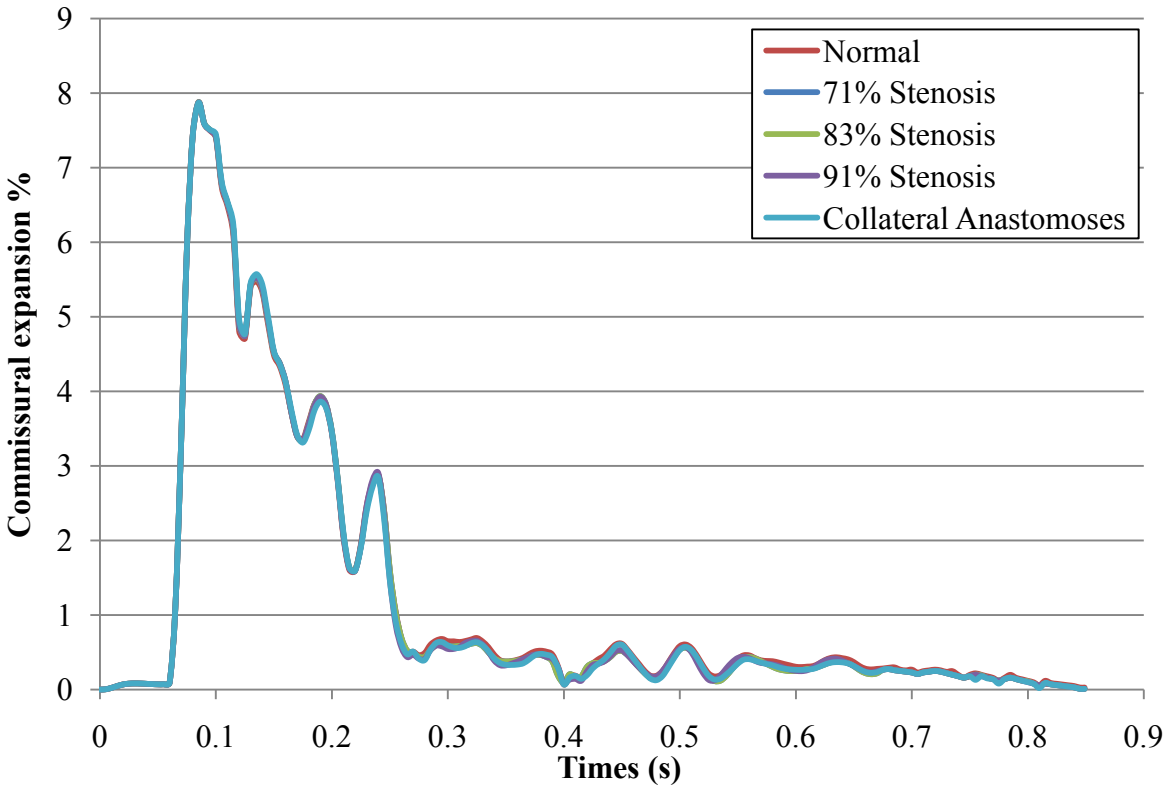

Figure 3.18: Comparison of commissural expansion measurements between different percentages of occluded coronary models and the normal global model.

In the course of the cardiac cycle there was no significant difference in commissural expansion observed in the different models. Even the model corresponding to the collateral anastomoses with no coronary flow reported similar values for the expansion of the aortic root. Alternatively, leaflet displacement was investigated to reveal any possible impact that coronary occlusion might have on valvular dynamics. Results for each of the three leaflets (non-coronary, occluded coronary and normal coronay) were calculated separately and compared to their corresponding measurements in the normal model. These results are presented below in Figure 3.19.

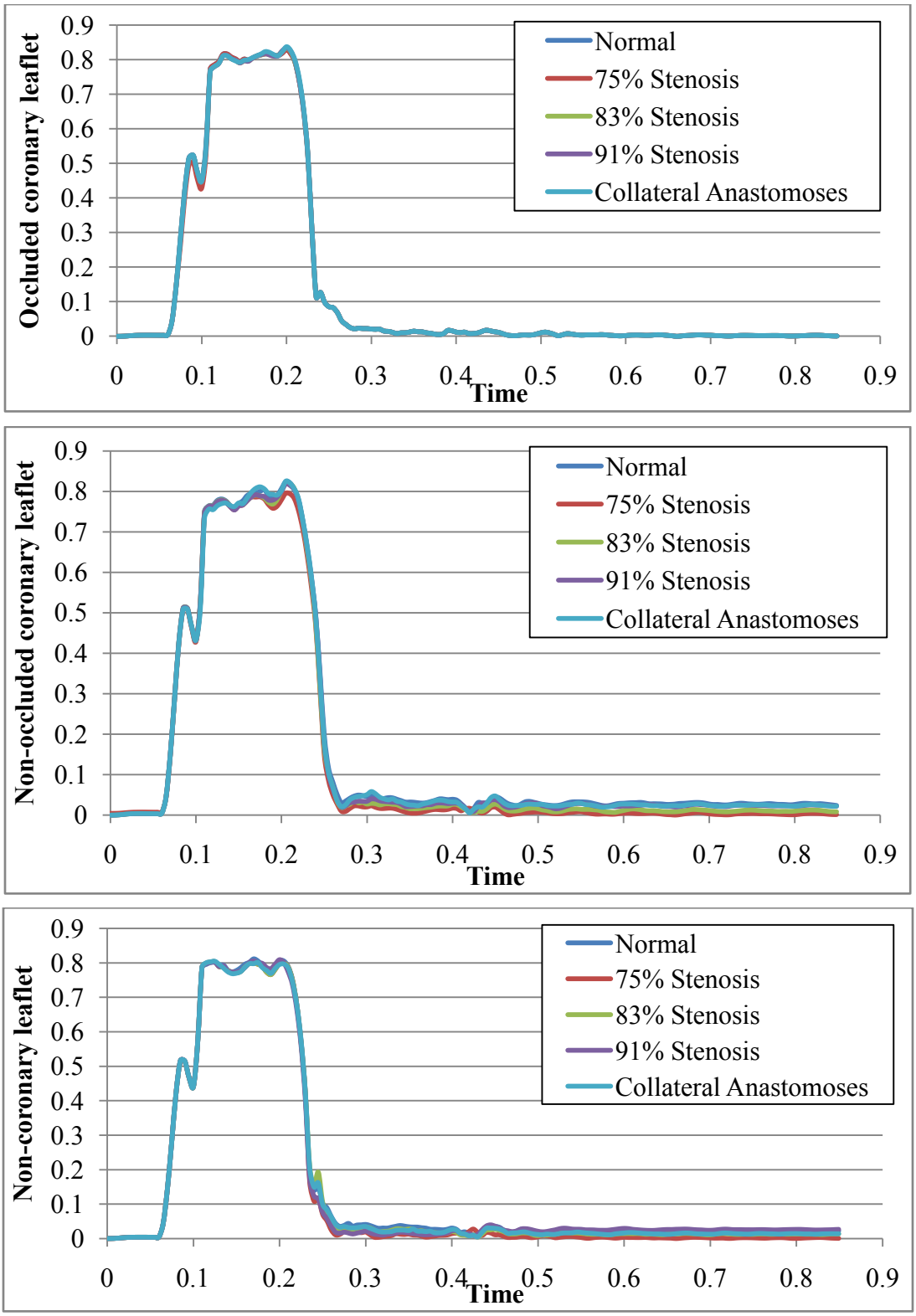

Figure 3.19: Comparison of individual leaflet tip displacement of the aortic valve in normal and pathological coronary arteries.

Similar to commissural expansion, there were no significant impacts observed on the standard indices of valvular dynamics either. Leaflet and aortic wall stresses were also calculated and it was shown that the location of maximum and minimum stresses as well as the overall stress distribution essentially remained unchanged. Moreover, blood velocity measurements above and below the leaflets showed similar values to the normal global model despite the severity of the coronary occlusion.

Since the morphology of the aortic valve was unchanged, measurement of the key clinical parameters presented in previous sections such as RVOT, RVOV, RVCT, RVCV and ET were very similar to those from the normal global model. This is of particular importance since in the case of individuals with normal valvular functions; a severely occluded coronary artery could go undetected. While this might be tolerated in patients with no apparent symptoms or with a stable coronary plaque, overlooking the existence of an unstable plaque could potentially lead to fatal consequences. Therefore care should be taken when dealing with patients who might have a normal functioning valve but might be at risk of coronary obstructive pathologies. The next chapter includes a discussion on the limitations involved in this research and points towards the suggested future work, summarizes the key observations and results from this thesis, and ultimately highlights the original outcomes of this research.

Chapter 4 : Discussion and conclusion

In this chapter, the original contributions of this work will be highlighted and a brief conclusion and discussion of the achieved results will be provided. We will acknowledge the limitations and assumptions of our research and point towards the possible future work.

4.1 Original outcomes

We were able to achieve the objectives and address the hypothesis of our work defined at the beginning of this thesis. The following, summarizes the original contributions achieved in the course of the work performed in this thesis:

- To the best of our knowledge, this is the first global, three dimensional, fluid-structure interaction model of the aortic valve which includes the natural leaflet structure and the two coronary arteries. Our model allows investigating the notion of a global pathology in the aortic valve area due to regional pathologies.
- The clinically observed inter-relation between valvular pathologies and coronary flow was investigated and confirmed. A critical threshold in coronary flow was reached due to aortic sclerosis once the values for tissue thickness and stiffness were increased by two and three times their normal values, respectively. Leaflet thickening had the highest impact on coronary flow compared to the other pathologies.
- The possible mutual impact that coronary pathologies might have on valvular dynamics were investigated. Results revealed no apparent variations in aortic root and aortic valve dynamics.
- Known clinical parameters which are accessible to the clinician (such as fractional flow reserve in addition to rapid valve opening and closing times and velocities) were correlated to engineering metrics (such as stiffness, thickness, flow and shear stress). This additional input provided by our model could serve as a possible planning tool and aid the cardiac surgeons in choosing the time and type of surgical intervention in the diseased aortic valve region.

4.2 Discussion

Due to the prevalence of aortic valve and coronary artery pathologies, these regions have been the main focus of many studies during the recent years. Certain pathologies such as aortic sclerosis alter the micro-structure of the aortic root and the aortic valve leaflets leading to variations in tissue thickness, stiffness or both; which ultimately are thought to affect coronary blood flow. Some clinical investigations have recently observed a simultaneous structural and hemodynamic variation in the coronaries and the aortic root regions due to localized pathologies. Complementary to clinical studies, which cannot explain these observed behaviours, biomechanical simulations have the potential to assist in understanding the underlying phenomenon that eventually leads to such global variations. The interaction between the cardiac tissue and the blood is critical in investigating aortic root region. However, the inherent complexity accustomed to fluid-structure interaction modeling of the aortic valve specifically in the leaflet area, has imposed significant limitations on the studies undertaken in this area. There is a clear lack of a global representation of the aortic valve region which would aid in a better understanding of the overall behaviour of this structure in response to regional pathologies.

Hence, the main objective of this thesis is to bring an understanding to this unexplained phenomenon where, a regional pathology could lead to global variations in the structure and hemodynamic of the aortic valve region and coronary arteries. Biomechanical representation of the aortic valve can assist in explaining the underlying interactions leading to such global variations. In order to achieve this goal, as a first step a three dimensional model of the aortic valve with the ostia outlet on the sinuses of Valsalva was developed and studied. Results were obtained for the structural and for the fluid domain separately. Using the general morphology of the leaflets and aortic root during the cardiac cycle, relevant clinical metrics such as ejection time, rapid valve opening and closing velocities/times were calculated. These key clinical parameters quantify the opening and closing patterns of the leaflets. Computed values were compared to echocardiography data and showed good agreements with clinical observations.

Leaflet stresses and their distribution patterns are other aspects that were calculated in the course of the cardiac cycle. Results revealed similar magnitudes during systole and diastole, however the location at which the maximum stress occurred shifted from the attachment edge to

the commissures, respectively. The measured values were compared to previous studies which revealed similar stress values as well as distribution patterns.

As for the fluid domain, parameters of interest included perfusion level into the coronary ostia and the blood velocity in the aortic root near the leaflet area. Velocity results for the normal case were similar to physiological values and showed no signs of back flow into the aortic root confirming leaflet contact definitions. Moreover, formation of vortices was observed at the beginning of the diastolic phase which is in agreement with clinical observations and is known to aid in leaflet closure.

In order to address the impact of pathologies leading to aortic sclerosis such as diabetes, hyperglycemia, hyperinsulinemia, and aging of the aortic valve on coronary perfusion, values of tissue stiffness and thickness were varied from normal to severe cases of aortic sclerosis. Results revealed a significant impact on the coronary perfusion due to a moderate increase in the aortic wall stiffness and leaflet thickness. A marked drop of coronary peak velocity was observed when the values of leaflet thickness and aortic wall stiffness reach above a certain threshold, corresponding to a threefold of their normal value. This lead us to the conclusion that mild and prophylactic treatments such as smoking cessation, exercise or diet, which have been proven to increase the aortic compliance, may significantly improve coronary perfusion.

Another interesting aspect that was investigated was the possible impact that the location of coronary ostia on the sinuses of Valsalva could have on coronary perfusion. Within the clinical practice, due to congenital disease or as a consequence of surgical procedures, such as remodeling or re-implantation, the normal anatomical location of these outlets could be altered. Coronary perfusion was calculated for three cases: normal height, medium and low height using our baseline model. Results showed minor variations in coronary perfusion among these three models. The values measure for the high ostia model in the course of a cardiac cycle closely follows the normal coronary flow curve in both ostia. However, in the low ostia model a maximum flow variation of 4 % was observed at the end of systole and beginning of diastole. Even though minor in value, the altered coronary perfusion, combined with variations in aortic root region due to valvular pathologies or as an outcome of surgical procedures, may lead to clinical manifestations in the long term. Considering the fact that the decision of the appropriate time and type of surgical intervention chosen for a given patient can vary among clinicians,

cardiac surgeons and interventional cardiologists could benefit from the additional input provided by this model. This model has the potential to serve as a possible diagnostic or surgical planning tool.

Therefore, to expand upon the baseline model of the aortic valve, coronary arteries were added to the baseline model to create a global model of the aortic valve. This global model better allows for extraction of hemodynamic variables along the coronary arteries and enables us to acquire velocity profile and shear stress measurements in addition to coronary perfusion. These measurements provide more valuable data for investigating the relation between valvular and coronary pathologies. Leaflet dynamics for the normal global model were investigated using the same key parameters (RVOT, RVOV, RVCT, RVCV and ET) and were compared to the base model and echocardiography data. Results showed an improvement in valvular dynamics compared to the normal base model in terms of similarity with clinical data. Leaflet morphology values calculated for the global model compare better to the physiological values measured by echocardiography. This is an important message which shows that a more global model of the aortic valve structure could potentially improve the obtained results compared to a more localized study. Application of boundary conditions more downstream and further from the valvular structure allows for a more physiological establishment of hemodynamic variables.

Moreover, values were also calculated for severe pathological conditions of aortic sclerosis to better understand how each of these pathologies affects leaflet dynamics and the global hemodynamic in the aortic root. To the best of our knowledge, this is the first global fluid-structure interaction model of the aortic valve which includes the coronary structures while comprising the natural aortic leaflets. This model can aid in exploring and confirming the underlying behavior of the interaction between aortic valve and coronary flow. Pathologies of the aortic leaflets seem to have a greater effect on the valvular dynamics compared to pathologies of the aortic root while leaflet thickening seems to be the most drastic of all. The increase in tissue stiffness and thickness do not create similar variations on leaflet dynamics since the global range of variation (normal to severely pathological) for these parameters is different. Consequently, similar values for pathological to normal ratios of these parameters could lead to significantly different outcomes on valvular dynamics. In the case of aortic wall pathologies the structural elastic recoil and its compliance was greatly affected leading to a decrease in its capabilities to store blood's kinetic energy during systole. Therefore the amount of energy released during diastole to aid leaflet closure

and blood perfusion through coronaries is reduces as well. Aortic wall thickening caused an apparent fluttering effect during systole which could be related to the fact that the extra thickness of wall tissue prohibits the sinus and commissural sections of the aortic root to expand to their normal range. The role of the elastic recoil becomes more evident by noticing the marginal variations in the opening characteristics of the leaflets compared to the substantial variations observed in closing dynamics from the normal state.

Results related to leaflet pathologies revealed great alterations in geometric orifice area due to variations in leaflet thickness and stiffness. Ultimately, the aortic wall elastic recoil was affected due to this geometrical variation and the compounding effect manifested itself through larger deviations from the normal state. Leaflet stiffening caused minor changes in the opening patterns during systole while the closing patterns during the diastolic phase were greatly affected in comparison to the normal case.

Results related to the fluid domain contained velocity profiles, shear stress and coronary flow measurements along the two arteries for three cases including the normal global model; and two pathological cases: aortic valve leaflet and aortic wall stiffening. Results revealed a continuous decrease in the maximum as well as average cross sectional velocity with the progression of the disease. These findings confirm the clinical observation made by other researchers. An increase in leaflet stiffness, equal to three times the normal value caused an apparent decrease in blood velocity measured across the arteries which is in agreement with the findings from the normal base model. Furthermore, aortic wall stiffness showed a more pronounced impact on coronary velocity profiles at a lower threshold of twice the normal values.

The overall impact that arterial curvature and pathological conditions have on velocity distribution along the coronary arteries can be seen from the obtained velocity profiles. Despite the continuous decrease in the maximum and average cross sectional velocity, at the initial cross sections where the arteries are almost straight, variations in velocity profile from the normal conditions due to pathologies are not as pronounced as they are downstream of the flow due to the existing abrupt curvatures. These curvatures seem to have significant effect on the location and magnitude of the maximum variations. As the radius of curvature decreases it was observed that the maximum velocity shifts towards the outer curvature while a secondary peak is created

along the inner side of the curvature. This is in agreement with clinically observed atherosclerosis-prone regions of coronary artery disease.

Shear stress experienced by the coronary arteries was also calculated for the normal, aortic wall and leaflet stiffening models. It was observed that aortic root pathologies have direct impact on the shear stress levels experienced at the vessel wall. This variation (either an increase or a decrease from the normal physiological values), in terms represents approaching the vicinity of the atheroprotective levels for the endothelial cells. This phenomenon in the long term could potentially lead to the initiation of coronary artery disease and if combined with an existing one, it could accelerate the progression of the disease. A more extensive analysis of shear stress is required for clinically relevant conclusions.

Coronary flow was also investigated to study its behavior with regional sclerotic pathologies of the aortic root. A continuous drop in the flow in both arteries was observed as the extent of pathology escaladed. Results revealed a considerable decrease in the coronary flow due to an increase in the cardiac tissue stiffness and thickness which concurs with clinical observations. This impact was most pronounced for the case of increased leaflet thickness (coronary artery stenosis). The cutoff value of 0.75 for fractional flow reserve was reached when the values of leaflet thickness and aortic wall stiffness were approximately twice and three times their normal value, respectively. Leaflet thickening had the highest impact on coronary flow compared to the other pathologies. The decrease in the flow starts at an earlier stage of the disease and follows a more accelerated pace. An increase in blood velocity through the valves (due to reduction of geometric orifice area) and an associated pressure drop is observed in this kind of pathology. Variations observed in coronary velocity profiles as well as wall shear stress suggest a possible link between valvular pathologies and the initiation of coronary artery disease.

Finally, coronary pathologies were investigated to study their possible impact on valvular dynamics. Results from the pathological global model suggest no significant impact from coronary occlusion on valvular dynamics. Commissural expansion, opening and closing patterns of the three leaflets, blood velocity above and below the cusps as well as leaflet and aortic wall stress distribution were investigated. No obvious variation from the normal conditions were observed despite the severity of coronary occlusion; even in the case of complete coronary blockage where collateral channels take over myocardial blood perfusion.

4.3 Conclusion

In summary, we met the main objective of this thesis which was to elucidate the observed but unexplained phenomenon where, a regional pathology could lead to global variations in the structure and hemodynamic of the aortic valve region and coronary arteries. Our hypothesis was addressed by investigating the impact of aortic pathologies on coronary flow, velocity and shear stress distribution. This was fulfilled using the global model of the aortic valve and varying values of tissue thickness and stiffness in the aortic wall, leaflets and root. To the best of our knowledge this is the first global 3D fluid-structure interaction model of the aortic valve which includes the natural leaflet structure and the two coronary arteries. By means of this model, the clinically observed inter-relation between valvular pathologies and coronary flow was verified. A marked drop was observed in coronary flow due to aortic sclerosis once the values for tissue thickness and stiffness reached a threshold of two and three times their normal values, respectively. Results obtained from the global model are coherent with clinical observations. These results support the initial hypothesis that mechanical properties of the aortic valve (i.e. elastic modulus, thickness) play an important role on coronary perfusion and are a main source in the inter-relation between valvular and coronary diseases in the context of a global pathology in the aortic valve.

4.4 Limitations and future work

When dealing with a complex model like the one presented in this thesis, assumptions and simplifications are inevitable. The assumptions in this work generally fall under two categories: those related to physiology of the model and the geometry construction; and those involving numerical analysis.

The geometry of the cardiac tissue is simplified to some extent since we are interested in the generic behavior and not patient specific cases. These simplifications are due to the variability and small sample sizes of available data related to aortic valve dimensions. Moreover, even with today's best imaging modalities, some structures remain hidden and need extra/interpolating to be numerically reconstructed. Therefore the aortic valve model presented in this thesis is based on an average value of key locations that have most commonly been reported in several studies. However, since the ultimate goal of such study is to aid in surgical planning, a parameterized geometry of the aortic valve would be useful. Increasing the number of parameters

defining the geometry would immensely aid in leading this research in a more patient specific direction.

Leaflets thickness variation is not taken into account in our model while naturally the leaflets are thinnest in the belly, their load-bearing part. They become thicker towards the line of attachment and the leaflet free edge. The thickest part is the nodule of Arrantius, just below the center of the free edge. Variable thickness across the leaflets might have an impact on valvular dynamics as well as on the stresses imposed on them in the course of a cardiac cycle. Additionally, the ascending aorta and the coronaries are extended somewhat beyond their physiological lengths to allow for boundary condition application.

Computational assumptions on the other hand are mostly due to the extensive computational cost in addition to stability/convergence issues associated with modeling aortic valve and in particular aortic leaflets. Calculation times for a single simulation would average to 2.5 days using a dual core processor, Windows 64 bit system at 3.6GHz with 8 Gb of memory. Aortic root and aortic valve leaflets are modeled using linear elastic material properties. Under normal physiological conditions, the strain in the aortic root varies in the range of about 10%. This strain rate is in the lower range of the nonlinear stress-strain curve of the cardiac tissue where it can essentially be considered linear. In fact, it has been shown that with this assumption the stress levels are within acceptable ranges as compared to hyperelastic modeling. However, in the context of aneurismal diseases, the linear elastic model used for its simplicity and ease of calculations would need to be expanded to nonlinear elastic in order to take into account for the large deformations. In addition, investigating aneurismal rupture process would require generalizing the assumption of an isotropic model, which is sufficient for global assessment, to anisotropic model to integrate the vascular microstructures. Viscoelasticity effects were also neglected to isolate the effect of pathologies that affect the elastic component in the cardiac tissue like wall stiffening and valve thickening on the energy stored in this elastic component. While introducing hyperelasticity and anisotropy into the model may modulate the results, the general assumptions should be similar.

Another simplification that was done is in the boundary conditions imposed at the main inlet and outlet of the model. The inlet condition at the aortic root is taken to be the difference between the ventricular pressure and the aortic pressure. This was due to severe instabilities

introduced in the model and unreasonable computation times of up to 2 months for a single simulation. This assumption however causes the entire system to be under an overall smaller pressure and the shell elements of the solid medium be subjected to a reduced transvalvular load while maintaining the pressure gradient across the valves. This leads to reduced commissural expansions compared to physiological values. The model could benefit from separate physiological application of boundary conditions at these locations.

Despite the care taken in generation of the fluid domain mesh, the model could further benefit from mesh refinement in the coronary artery zone. Even though this mesh is fine enough to calculate velocity profiles and flow in these structures, additional refinement is required for precise calculation of wall shear stress vorticity. This however would require a global mesh refinement to maintain element ratio between the fluid and the solid in the FSI formulation, which would eventually lead to extensive computational times with current resources. High performance computing platforms such as the McGill CLUMEQ or parallel processing is needed.

The amount of available/published data related to coronary pressure is quite limited especially in the case of healthy individuals. Moreover, pressure and flow measurements in coronary arteries are normally performed more downstream (after the first bifurcation) compared to our model and their values are strongly dependant on downstream resistance which is regulated by several factors such as myocardial oxygen demand and aortic pressure. Since we were interested in investigating the impact of valvular pathologies on coronary flow perturbations, maintaining outlet pressure was a reasonable approach since it allows isolating a single variable at a time. As a consequence, autoregulation and vasodilation/contraction of these arteries were not incorporated into the model and should be addressed in future work.

The results from our simulations have been corroborated/verified using clinical and previously published data from numerical simulations carried out by other research groups. However in this thesis, the model has not been explicitly validated in terms of the sensitivity of its behaviour to changes in boundary conditions, material properties, geometric simplifications or physiological state (stroke volume, heart rate). Validation of the findings of this work is needed using sensitivity analysis and experimental studies which would eventually lead to animal and human studies. These investigations require an extensive amount of time, effort and financial

support and therefore were considered to be out of the scope of this research but should be considered in future work.

References

1. Schoen, F.J., *Future Directions in Tissue Heart Valves: Impact of Recent Insights from Biology and Pathology.* Journal of Heart Valve Disease, 1999. **8**(4): p. 350-8.
2. Anderson, R.H., *Clinical Anatomy of the Aortic Root.* Heart, 2000. **84**(6): p. 670-3.
3. Vesely, I. and Noseworthy, R., *Micromechanics of the Fibrosa and the Ventricularis in Aortic Valve Leaflets.* Journal of Biomechanics, 1992. **25**(1): p. 101-13.
4. Scott, M. and Vesely, I., *Aortic Valve Cusp Microstructure: The Role of Elastin.* Annals of Thoracic Surgery, 1995. **60**(2 Suppl): p. S391-4.
5. Scott, M.J. and Vesely, I., *Morphology of Porcine Aortic Valve Cusp Elastin.* Journal of Heart Valve Disease, 1996. **5**(5): p. 464-71.
6. Thubrikar, M.J., Aouad, J., and Nolan, S.P., *Comparison of the in Vivo and in Vitro Mechanical Properties of Aortic Valve Leaflets.* Journal of Thoracic and Cardiovascular Surgery, 1986. **92**(1): p. 29-36.
7. Thubrikar, M.J., Nolan, S.P., Aouad, J., and Deck, J.D., *Stress Sharing between the Sinus and Leaflets of Canine Aortic Valve.* Annals of Thoracic Surgery, 1986. **42**(4): p. 434-40.
8. Sauren, A.A., Kuijpers, W., Van Steenhoven, A.A., and Veldpaus, F.E., *Aortic Valve Histology and Its Relation with Mechanics-Preliminary Report.* Journal of Biomechanics, 1980. **13**(2): p. 97-104.
9. Nerem, R.M. and Seed, W.A., *An in Vivo Study of Aortic Flow Disturbances.* Cardiovascular Research, 1972. **6**(1): p. 1-14.
10. Nishimura, R.A., *Cardiology Patient Pages. Aortic Valve Disease.* Circulation, 2002. **106**(7): p. 770-2.
11. Subramanian, R., Olson, L.J., and Edwards, W.D., *Surgical Pathology of Pure Aortic Stenosis: A Study of 374 Cases.* Mayo Clinic Proceedings, 1984. **59**(10): p. 683-90.
12. Olson, L.J., Subramanian, R., and Edwards, W.D., *Surgical Pathology of Pure Aortic Insufficiency: A Study of 225 Cases.* Mayo Clinic Proceedings, 1984. **59**(12): p. 835-41.
13. Thubrikar, M.J., Roskelley, S.K., and Eppink, R.T., *Study of Stress Concentration in the Walls of the Bovine Coronary Arterial Branch.* Journal of Biomechanics, 1990. **23**(1): p. 15-26.
14. Mitka, M., *Trials Planned for Testing Nonsurgical Approach to Replacing Heart Valves.* JAMA: The Journal of American Medical Association, 2003. **289**(11): p. 1366-7.
15. Schoen, F.J., *Surgical Pathology of Removed Natural and Prosthetic Heart Valves.* Human Pathology, 1987. **18**(6): p. 558-67.
16. Schoen, F.J., *Cardiac Valve Prostheses: Pathological and Bioengineering Considerations.* Journal of Cardiac Surgery, 1987. **2**(1): p. 65-108.
17. Canadas, V., Vilacosta, I., Bruna, I., and Fuster, V., *Marfan Syndrome. Part 2: Treatment and Management of Patients.* Nature Reviews Cardiology, 2010. **7**(5): p. 266-76.
18. Kallenbach, K., Karck, M., and Haverich, A., *Valve-Sparing Aortic Root Replacement: The Inclusion (David) Technique.* Multimedia Manual of Cardio-Thoracic Surgery, 2007(0507).
19. Demers, P. and Miller, D.C., *Simple Modification of "T. David-V" Valve-Sparing Aortic Root Replacement to Create Graft Pseudosinuses.* Annals of Thoracic Surgery, 2004. **78**(4): p. 1479-81.

20. Krams, R., Cuhlmann, S., Foin, N., and Evans, P., *Shear Stress, Inflammation and Atherosclerosis.* Artery Research, 2010. **4**(2): p. 41-46.
21. Weissberg, P.L., *Atherogenesis: Current Understanding of the Causes of Atheroma.* Heart, 2000. **83**(2): p. 247-52.
22. Davies, J.R., Rudd, J.H., and Weissberg, P.L., *Molecular and Metabolic Imaging of Atherosclerosis.* Journal of Nuclear Medicine, 2004. **45**(11): p. 1898-907.
23. Miller, A.B., *A Symposium: Coronary Atherosclerosis: Early Detection and Aggressive Management Strategies. Introduction.* American Journal of Cardiology, 2001. **88**(10A): p. 1M.
24. Gibson, C.M., Diaz, L., Kandarpa, K., Sacks, F.M., Pasternak, R.C., Sandor, T., Feldman, C., and Stone, P.H., *Relation of Vessel Wall Shear Stress to Atherosclerosis Progression in Human Coronary Arteries.* Arteriosclerosis and Thrombosis, 1993. **13**(2): p. 310-5.
25. Myers, J.G., Moore, J.A., Ojha, M., Johnston, K.W., and Ethier, C.R., *Factors Influencing Blood Flow Patterns in the Human Right Coronary Artery.* Annals of Biomedical Engineering, 2001. **29**(2): p. 109-20.
26. Libby, P., *Inflammation in Atherosclerosis.* Nature, 2002. **420**(6917): p. 868-74.
27. Wahle, A., Lopez, J.J., Olszewski, M.E., Vigmostad, S.C., Chandran, K.B., Rossen, J.D., and Sonka, M., *Plaque Development, Vessel Curvature, and Wall Shear Stress in Coronary Arteries Assessed by X-Ray Angiography and Intravascular Ultrasound.* Medical Image Analysis, 2006. **10**(4): p. 615-31.
28. Deshpande, V.S. and Li, D., *Coronary Mra*, in *Current Protocols in Magnetic Resonance Imaging*2001, John Wiley & Sons, Inc.
29. Pundziute, G., Schuijf, J.D., Jukema, J.W., Decramer, I., Sarno, G., Vanhoenacker, P.K., Boersma, E., Reiber, J.H., Schalij, M.J., Wijns, W., and Bax, J.J., *Evaluation of Plaque Characteristics in Acute Coronary Syndromes: Non-Invasive Assessment with Multi-Slice Computed Tomography and Invasive Evaluation with Intravascular Ultrasound Radiofrequency Data Analysis.* European Heart Journal, 2008. **29**(19): p. 2373-81.
30. Dimitrow, P.P., *Transthoracic Doppler Echocardiography - Noninvasive Diagnostic Window for Coronary Flow Reserve Assessment.* Cardiovascular Ultrasound, 2003. **1**: p. 4.
31. Pijls, N.H., De Bruyne, B., Peels, K., Van Der Voort, P.H., Bonnier, H.J., Bartunek, J.K.J.J., and Koolen, J.J., *Measurement of Fractional Flow Reserve to Assess the Functional Severity of Coronary-Artery Stenoses.* The New England Journal of Medicine, 1996. **334**(26): p. 1703-8.
32. Hau, W.K., *Fractional Flow Reserve and Complex Coronary Pathologic Conditions.* European Heart Journal, 2004. **25**(9): p. 723-7.
33. Mcneill, A., Flannery, D., Wilson, C., Dalzell, G., Campbell, N., Khan, M., Patterson, G., Webb, S., and Adgey, A., *Thrombolytic Therapy within One Hour of the Onset of Acute Myocardial Infarction.* QJM, 1991. **79**(3): p. 487-494.
34. Berne, R.M. and Levy, M.N., *Cardiovascular Physiology,*1997: Mosby.
35. Moon, J.Y., Chung, J.W., Kim, J.H., Ahn, Y.K., and Jeong, M.H., *Simultaneous Subacute Stent Thrombosis of Two Sirolimus-Eluting Stents in a Patient Treated by Reopro, Thrombus Aspiration and Triple Anti-Platelet Agents.* International Journal of Cardiology, 2008. **130**(1): p. e25-9.
36. Hibbitt, K., And Sorenson, *Abaqus Theory Manual*, 2003: Pawtucket, RI , USA.

37. Dokainish, M.A. and Subbaraj, K., *A Survey of Direct Time-Integration Methods in Computational Structural Dynamics—I. Explicit Methods.* Computers & Structures, 1989. **32**(6): p. 1371-1386.
38. Fisher, A.R., R. N.; Rodrigue, G. H.; White, D. A., *A Generalized Mass Lumping Technique for Vector Finite-Element Solutions of the Time-Dependent Maxwell Equations.* IEEE Transactions on Antennas and Propagation, 2004. **53**(9): p. 2900-2910.
39. Jeong, K., Sung-Jong, K., and Beom-Soo, K., *A Comparative Study of Implicit and Explicit Fem for the Wrinkling Prediction in the Hydroforming Process.* International Journal of Advanced Manufacturing Technology, 2003. **22**(7/8): p. 547-552.
40. Souli, M., *Ls-Dyna Advanced Course in Ale and Fluid/Structure Coupling,* 2004, CA: Livermore Scientific Technology Corp, Livermore.
41. Hughes, T.J.R., Liu, W.K., and Zimmermann, T.K., *Lagrangian-Eulerian Finite Element Formulation for Incompressible Viscous Flows.* Computer Methods in Applied Mechanics and Engineering, 1981. **29**(3): p. 329-349.
42. Donea, J., Giuliani, S., and Halleux, J.P., *An Arbitrary Lagrangian-Eulerian Finite Element Method for Transient Dynamic Fluid-Structure Interactions.* Computer Methods in Applied Mechanics and Engineering, 1982. **33**(1–3): p. 689-723.
43. Peskin, C.S., *The Immersed Boundary Method.* Acta Numer, 2002. **11**: p. 479–517.
44. Peskin, C.S., *Flow Patterns around Heart Valves: A Numerical Method.* Journal of Computational Physics, 1972. **10**(2): p. 252-271.
45. Makhijani, V.B., Yang, H.Q., Dionne, P.J., and Thubrikar, M.J., *Three-Dimensional Coupled Fluid-Structure Simulation of Pericardial Bioprosthetic Aortic Valve Function.* Journal of American Society for Artificial Internal Organs, 1997. **43**(5): p. M387-92.
46. Glowinski, R., Pan, T.-W., and Periaux, J., *A Lagrange Multiplier/Fictitious Domain Method for the Numerical Simulation of Incompressible Viscous Flow around Moving Rigid Bodies: (I) Case Where the Rigid Body Motions Are Known a Priori.* Comptes Rendus de l'Académie des Sciences - Series I - Mathematics, 1997. **324**(3): p. 361-369.
47. Baaijens, F.P.T., *A Fictitious Domain/Mortar Element Method for Fluid–Structure Interaction.* International Journal for Numerical Methods in Fluids, 2001. **35**(7): p. 743-761.
48. De Hart, J., Peters, G.W.M., Schreurs, P.J.G., and Baaijens, F.P.T., *A Two-Dimensional Fluid–Structure Interaction Model of the Aortic Value.* Journal of Biomechanics, 2000. **33**(9): p. 1079-1088.
49. De Hart, J., Peters, G.W.M., Schreurs, P.J.G., and Baaijens, F.P.T., *A Three-Dimensional Computational Analysis of Fluid–Structure Interaction in the Aortic Valve.* Journal of Biomechanics, 2003. **36**(1): p. 103-112.
50. Van Loon, R., Anderson, P.D., De Hart, J., and Baaijens, F.P.T., *A Combined Fictitious Domain/Adaptive Meshing Method for Fluid–Structure Interaction in Heart Valves.* International Journal for Numerical Methods in Fluids, 2004. **46**(5): p. 533-544.
51. Van Loon, R., Anderson, P.D., and Van De Vosse, F.N., *A Fluid–Structure Interaction Method with Solid-Rigid Contact for Heart Valve Dynamics.* Journal of Computational Physics, 2006. **217**(2): p. 806-823.
52. Nicosia, M.A., Cochran, R.P., Einstein, D.R., Rutland, C.J., and Kunzelman, K.S., *A Coupled Fluid-Structure Finite Element Model of the Aortic Valve and Root.* Journal of Heart Valve Disease, 2003. **12**(6): p. 781-9.

53. Carmody, C.J., Burriesci, G., Howard, I.C., and Patterson, E.A., *An Approach to the Simulation of Fluid-Structure Interaction in the Aortic Valve.* Journal of Biomechanics, 2006. **39**(1): p. 158-69.
54. Weinberg, E.J., Schoen, F.J., and Mofrad, M.R., *A Computational Model of Aging and Calcification in the Aortic Heart Valve.* PLoS One, 2009. **4**(6): p. e5960.
55. Weinberg, E.J. and Kaazempur Mofrad, M.R., *A Multiscale Computational Comparison of the Bicuspid and Tricuspid Aortic Valves in Relation to Calcific Aortic Stenosis.* Journal of Biomechanics, 2008. **41**(16): p. 3482-7.
56. Ranga, A., Mongrain, R., Mendes Galaz, R., Biadillah, Y., and Cartier, R., *Large-Displacement 3d Structural Analysis of an Aortic Valve Model with Nonlinear Material Properties.* Journal of Medical Engineering and Technology, 2004. **28**(3): p. 95-103; discussion 104.
57. Ranga, A., Bouchot, O., Mongrain, R., Ugolini, P., and Cartier, R., *Computational Simulations of the Aortic Valve Validated by Imaging Data: Evaluation of Valve-Sparing Techniques.* Interactive Cardiovascular and Thoracic Surgery, 2006. **5**(4): p. 373-8.
58. Souli, M. and Shahrour, I., *A Coupling Method for Soil Structure Interaction Problems.* International Journal for Numerical and Analytical Methods in Geomechanics, 2012.
59. Young, D., *Time-Dependent Multi-Material Flow with Large Fluid Distortion*, in *Numerical Methods for Fluid Dynamics*, K.W. Morton and M.J. Baines, Editors. 1982, Academic Press: New York. p. 273-285.
60. Aquelet, N., Souli, M., and Olovsson, L., *Euler-Lagrange Coupling with Damping Effects: Application to Slamming Problems.* Computer Methods in Applied Mechanics and Engineering, 2006. **195**(1-3): p. 110-132.
61. Kim, S.W., *Velocity-Pressure Integrated Versus Penalty Finite Element Methods for High Reynoldsnumber Flows.* International Journal for Numerical Methods in Fluids, 1989. **9**(1): p. 43.
62. Peskin, C.S. and Mcqueen, D.M., *A General Method for the Computer Simulation of Biological Systems Interacting with Fluids.* Symposia Society for Experimental Biology, 1995. **49**: p. 265-276.
63. Chew, G.G., Howard, I.C., and Patterson, E.A., *Simulation of Damage in a Porcine Prosthetic Heart Valve.* Journal of Medical Engineering and Technology, 1999. **23**(5): p. 178-89.
64. De Hart, J., Baaijens, F.P.T., Peters, G.W.M., and Schreurs, P.J.G., *A Computational Fluid-Structure Interaction Analysis of a Fiber-Reinforced Stentless Aortic Valve.* Journal of Biomechanics, 2003. **36**(5): p. 699-712.
65. De Hart, J., Peters, G.W.M., Schreurs, P.J.G., and Baaijens, F.P.T., *Collagen Fibers Reduce Stresses and Stabilize Motion of Aortic Valve Leaflets During Systole.* Journal of Biomechanics, 2004. **37**(3): p. 303-311.
66. Howard, I.C., Patterson, E.A., and Yoxall, A., *On the Opening Mechanism of the Aortic Valve: Some Observations from Simulations.* Journal of Medical Engineering and Technology, 2003. **27**(6): p. 259-66.
67. Gnyaneshwar, R., Kumar, R.K., and Balakrishnan, K.R., *Dynamic Analysis of the Aortic Valve Using a Finite Element Model.* Annals of Thoracic Surgery, 2002. **73**(4): p. 1122-9.

68. Sripathi, V.C., Kumar, R.K., and Balakrishnan, K.R., *Further Insights into Normal Aortic Valve Function: Role of a Compliant Aortic Root on Leaflet Opening and Valve Orifice Area.* Annals of Thoracic Surgery, 2004. **77**(3): p. 844-51.
69. Weinberg, E.J. and Kaazempur Mofrad, M.R., *Transient, Three-Dimensional, Multiscale Simulations of the Human Aortic Valve.* Cardiovascular Engineering, 2007. **7**(4): p. 140-55.
70. Thubrikar, M.J., Labrosse, M.R., Zehr, K.J., Robicsek, F., Gong, G.G., and Fowler, B.L., *Aortic Root Dilatation May Alter the Dimensions of the Valve Leaflets.* European Journal of Cardio-Thoracic Surgery, 2005. **28**(6): p. 850-5.
71. Labrosse, M.R., Beller, C.J., Robicsek, F., and Thubrikar, M.J., *Geometric Modeling of Functional Trileaflet Aortic Valves: Development and Clinical Applications.* Journal of Biomechanics, 2006. **39**(14): p. 2665-72.
72. Beller, C.J., Labrosse, M.R., Thubrikar, M.J., and Robicsek, F., *Role of Aortic Root Motion in the Pathogenesis of Aortic Dissection.* Circulation, 2004. **109**(6): p. 763-9.
73. Katayama, S., Umetani, N., Sugiura, S., and Hisada, T., *The Sinus of Valsalva Relieves Abnormal Stress on Aortic Valve Leaflets by Facilitating Smooth Closure.* Journal of Thoracic and Cardiovascular Surgery, 2008. **136**(6): p. 1528-35, 1535 e1.
74. Van Loon, R., *Towards Computational Modelling of Aortic Stenosis.* International Journal for Numerical Methods in Biomedical Engineering, 2010. **26**(3-4): p. 405-420.
75. Kim, H.J., Vignon-Clementel, I.E., Coogan, J.S., Figueroa, C.A., Jansen, K.E., and Taylor, C.A., *Patient-Specific Modeling of Blood Flow and Pressure in Human Coronary Arteries.* Annals of Biomedical Engineering, 2010. **38**(10): p. 3195-209.
76. Kim, H.J., Vignon-Clementel, I.E., Figueroa, C.A., Jansen, K.E., and Taylor, C.A., *Developing Computational Methods for Three-Dimensional Finite Element Simulations of Coronary Blood Flow.* Finite Elements in Analysis and Design, 2010. **46**(6): p. 514-525.
77. Campbel, I., Mongrain, R., and Cartier, R. *Coronary Flow in an Fsi Model of the Aortic Valve*. in *Proceedings of the 30th Canadian Medical and Biological Engineering Conference (CMBEC30)*. 2007.
78. Stella, A., Gessaroli, M., Cifiello, B.I., Salardi, S., Reggiani, A., Cacciari, E., and D'addato, M., *Elastic Modulus in Young Diabetic Patients (Ultrasound Measurements of Pulse Wave Velocity).* Angiology, 1984. **35**(11): p. 729-34.
79. Airaksinen, K.E., Salmela, P.I., Linnaluoto, M.K., Ikaheimo, M.J., Ahola, K., and Ryhanen, L.J., *Diminished Arterial Elasticity in Diabetes: Association with Fluorescent Advanced Glycosylation End Products in Collagen.* Cardiovascular Research, 1993. **27**(6): p. 942-5.
80. Toto-Moukouo, J.J., Achimastos, A., Asmar, R.G., Hugues, C.J., and Safar, M.E., *Pulse Wave Velocity in Patients with Obesity and Hypertension.* American Heart Journal, 1986. **112**(1): p. 136-40.
81. Kupari, M., Hekali, P., Keto, P., Poutanen, V.P., Tikkanen, M.J., and Standerstkjold-Nordenstam, C.G., *Relation of Aortic Stiffness to Factors Modifying the Risk of Atherosclerosis in Healthy People.* Arteriosclerosis and Thrombosis, 1994. **14**(3): p. 386-94.
82. El-Hamamsy, I., Chester, A.H., and Yacoub, M.H., *Cellular Regulation of the Structure and Function of Aortic Valves.* Journal of Advanced Research, 2010. **1**(1): p. 5-12.

83. Safar, M.E., *Arterial Stiffness: A Simplified Overview in Vascular Medicine.* Advances in Cardiology, 2007. **44**: p. 1-18.
84. Sahasakul, Y., Edwards, W.D., Naessens, J.M., and Tajik, A.J., *Age-Related Changes in Aortic and Mitral Valve Thickness: Implications for Two-Dimensional Echocardiography Based on an Autopsy Study of 200 Normal Human Hearts.* American Journal of Cardiology, 1988. **62**(7): p. 424-30.
85. Christie, G.W. and Barratt-Boyes, B.G., *Age-Dependent Changes in the Radial Stretch of Human Aortic Valve Leaflets Determined by Biaxial Testing.* Annals of Thoracic Surgery, 1995. **60**(2 Suppl): p. S156-8; discussion S159.
86. Garcia, D., Camici, P.G., Durand, L.G., Rajappan, K., Gaillard, E., Rimoldi, O.E., and Pibarot, P., *Impairment of Coronary Flow Reserve in Aortic Stenosis.* Journal of Applied Physiology, 2009. **106**(1): p. 113-21.
87. O'rourke, M.F., *How Stiffening of the Aorta and Elastic Arteries Leads to Compromised Coronary Flow.* Heart, 2008. **94**(6): p. 690-691.
88. Stefanadis, C., Stratos, C., Boudoulas, H., Vlachopoulos, C., Kallikazaros, I., and Toutouzas, P., *Distensibility of the Ascending Aorta in Coronary Artery Disease and Changes after Nifedipine Administration.* Chest, 1994. **105**(4): p. 1017-23.
89. Otto, C.M., *Why Is Aortic Sclerosis Associated with Adverse Clinical Outcomes?* Journal of the American College of Cardiology, 2004. **43**(2): p. 176-178.
90. Thubrikar, M., *The Aortic Valve*1990, Boca Raton: CRC Press Inc.
91. Diniz Dos Santos, N., Gerbeau, J.F., and Bourgat, J.F., *A Partitioned Fluid–Structure Algorithm for Elastic Thin Valves with Contact.* Computer Methods in Applied Mechanics and Engineering, 2008. **197**(19–20): p. 1750-1761.
92. De Tullio, M.D., Pascazio, G., Weltert, L., De Paulis, R., and Verzicco, R., *Evaluation of Prosthetic-Valved Devices by Means of Numerical Simulations.* Philosophical Transactions. Series A, Mathematical, Physical and Engineering Sciences, 2011. **369**(1945): p. 2502-9.
93. Verhey, J.F. and Bara, C., *Influence on Fluid Dynamics of Coronary Artery Outlet Angle Variation in Artificial Aortic Root Prosthesis.* Biomededical Engineering Online, 2008. **7**: p. 9.
94. De Tullio, M.D., Afferrante, L., Demelio, G., Pascazio, G., and Verzicco, R., *Fluid–Structure Interaction of Deformable Aortic Prostheses with a Bileaflet Mechanical Valve.* Journal of Biomechanics, 2011. **44**(9): p. 1684-1690.
95. De Tullio, M., Pedrizzetti, G., and Verzicco, R., *On the Effect of Aortic Root Geometry on the Coronary Entry-Flow after a Bileaflet Mechanical Heart Valve Implant: A Numerical Study.* Acta Mechanica, 2011. **216**(1): p. 147-163.
96. Garcia, D., Camici, P.G., Durand, L.-G., Rajappan, K., Gaillard, E., Rimoldi, O.E., and Pibarot, P., *Impairment of Coronary Flow Reserve in Aortic Stenosis.* Journal of Applied Physiology, 2009. **106**(1): p. 113-121.
97. Gaillard, E., Garcia, D., Kadem, L., Pibarot, P., and Durand, L.G., *In Vitro Investigation of the Impact of Aortic Valve Stenosis Severity on Left Coronary Artery Flow.* Journal of Biomechanical Engineering, 2010. **132**(4): p. 044502.
98. Rainsberger, R., *Truegrid® User's Manual, a Guide and a Reference, Xyz Scientific Applications, Inc.* 2006.

99. Galaz Mendez, R., *A Computational Study to Assess the Effect of the Coronary Hemodynamics on the Mechanical Stresses of Stenotic Atherosclerotic Plaques*, in *Biomedical Engineering Department,* 2008, McGill University.
100. Gottsauner-Wolf, M., Sochor, H., Moertl, D., Gwechenberger, M., Stochenhuber, F., and Probst, P., *Assessing Coronary Stenosis. Quantitative Coronary Angiography Versus Visual Estimation from Cine-Film or Pharmacological Stress Perfusion Images.* European Heart Journal, 1996. **17**(8): p. 1167-1174.
101. Gur, M., Yilmaz, R., Demirbag, R., Yildiz, A., Menduh Bas, M., and Polat, M., *Relationship between Impaired Elastic Properties of Aorta with Left Ventricle Geometric Patterns and Left Ventricle Diastolic Functions in Patients with Newly Diagnosed Essential Hypertension.* International Journal of Clinical Practice, 2006. **60**(11): p. 1357-1363.
102. Oishi, Y., Mizuguchi, Y., Miyoshi, H., Iuchi, A., Nagase, N., and Oki, T., *A Novel Approach to Assess Aortic Stiffness Related to Changes in Aging Using a Two-Dimensional Strain Imaging.* Echocardiography, 2008. **25**(9): p. 941-5.
103. Tremblay, D., Zigras, T., Cartier, R., Leduc, L., Butany, J., Mongrain, R., and Leask, R., *A Comparison of Mechanical Properties of Materials Used in Aortic Arch Reconstruction.* Annals of Thoracic Surgery, 2009. **88**(5): p. 1484-1491.
104. Choudhury, N., Bouchot, O., Rouleau, L., Tremblay, D., Cartier, R., Butany, J., Mongrain, R., and Leask, R.L., *Local Mechanical and Structural Properties of Healthy and Diseased Human Ascending Aorta Tissue.* Cardiovascular Pathology, 2009. **18**(2): p. 83-91.
105. Grande-Allen, K.J., Cochran, R.P., Reinhall, P.G., and Kunzelman, K.S., *Re-Creation of Sinuses Is Important for Sparing the Aortic Valve: A Finite Element Study.* Journal of Thoracic and Cardiovascular Surgery, 2000. **119**(4): p. 753-762.
106. Beck, A., Thubrikar, M.J., and Robicsek, F., *Stress Analysis of the Aortic Valve with and without the Sinuses of Valsalva.* Journal of Heart Valve Disease, 2001. **10**(1): p. 1-11.
107. Di Martino, E.S., Guadagni, G., Fumero, A., Ballerini, G., Spirito, R., Biglioli, P., and Redaelli, A., *Fluid–Structure Interaction within Realistic Three-Dimensional Models of the Aneurysmatic Aorta as a Guidance to Assess the Risk of Rupture of the Aneurysm.* Medical Engineering & Physics, 2001. **23**(9): p. 647-655.
108. Cataloglu, A., Gould, P.L., and Clark, R.E., *Validation of a Simplified Mathematical Model for the Stress Analysis of Human Aortic Heart Valves.* Journal of Biomechanics, 1975. **8**(5): p. 347-8.
109. Hashim, S. and Richens, D., *Finite Element Method in Cardiac Surgery.* Interactive Cardiovascular and Thoracic Surgery, 2006. **5**(1): p. 5-8.
110. Thurston, G.B., *Viscoelasticity of Human Blood.* Biophysical Journal, 1972. **12**(9): p. 1205-17.
111. Thurston, G.B., *Frequency and Shear Rate Dependence of Viscoelasticity of Human Blood.* Biorheology, 1973. **10**(3): p. 375-81.
112. Chien, S., Usami, S., Dellenback, R.J., Gregersen, M.I., Nanninga, L.B., and Guest, M.M., *Blood Viscosity: Influence of Erythrocyte Aggregation.* Science, 1967. **157**(3790): p. 829-31.
113. Berger, S.A., Goldsmith, W., and Lewis, E.R., *Introduction to Bioengineering*2000, Oxford: Oxford University Press. xiv, 526 p.

114. Fung, Y.C. and Chien, S., *Introduction to Bioengineering*2001, Singapore ; River Edge, NJ: World Scientific. xvii, 293 p.
115. Vito, R.P., *The Role of the Pericardium in Cardiac Mechanics.* Journal of Biomechanics, 1979. **12**(8): p. 587-92.
116. Honda, A., Ohashi, Y., and Mori, Y., *Effect of High-Molecular-Weight Hyaluronic Acid on the Viscosity of Rabbit Pericardial Fluid Measured with a Cone and Plate Viscometer.* Chemical and Pharmaceutical Bulletin, 1986. **34**(11): p. 4844-7.
117. D'sa, S., *Hyperviscosity Syndrome*, in *Doctor on call,* 2012. p. 4.
118. Sipkema, P., Yamada, H., and Yin, F.C.P., *Coronary Artery Resistance Changes Depend on How Surrounding Myocardial Tissue Is Stretched.* American Journal of Physiology-Heart and Circulatory Physiology, 1996. **270**(3): p. H924-H934.
119. Levy, M.N.P., A. J., *Cardiovascular Physiology*. 9th edition. Mosby Physiology Monograph Series, 2007.
120. Siebes, M., Verhoeff, B.J., Meuwissen, M., De Winter, R.J., Spaan, J.A., and Piek, J.J., *Single-Wire Pressure and Flow Velocity Measurement to Quantify Coronary Stenosis Hemodynamics and Effects of Percutaneous Interventions.* Circulation, 2004. **109**(6): p. 756-62.
121. Klocke, F.J., *Measurements of Coronary Blood Flow and Degree of Stenosis: Current Clinical Implications and Continuing Uncertainties.* Journal of the American College of Cardiology, 1983. **1**(1): p. 31-41.
122. Shalman, E., Rosenfeld, M., Dgany, E., and Einav, S., *Numerical Modeling of the Flow in Stenosed Coronary Artery. The Relationship between Main Hemodynamic Parameters.* Computers in Biology and Medicine, 2002. **32**(5): p. 329-44.
123. Uren, N.G., Melin, J.A., De Bruyne, B., Wijns, W., Baudhuin, T., and Camici, P.G., *Relation between Myocardial Blood Flow and the Severity of Coronary-Artery Stenosis.* New England Journal of Medicine, 1994. **330**(25): p. 1782-1788.
124. Fujita, M., Sasayama, S., Ohno, A., Nakajima, H., and Asanoi, H., *Importance of Angina for Development of Collateral Circulation.* British Heart Journal, 1987. **57**(2): p. 139-43.
125. Tayebjee, M.H., Lip, G.Y., and Macfadyen, R.J., *Collateralization and the Response to Obstruction of Epicardial Coronary Arteries.* QJM, 2004. **97**(5): p. 259-72.
126. Levin, D.C., *Pathways and Functional Significance of the Coronary Collateral Circulation.* Circulation, 1974. **50**(4): p. 831-7.
127. Metzger, J.P., Le Pailleur, C., Hui Bon Hoa, F., Lafont, H., and Di Matteo, J., *[Coronary Collateral Circulation. Anatomic Pathways and Functional Significance]*. Nouvelle Presse Medicale, 1975. **4**(38): p. 2719-22.
128. Perktold, K. and Rappitsch, G., *Computer Simulation of Local Blood Flow and Vessel Mechanics in a Compliant Carotid Artery Bifurcation Model.* Journal of Biomechanics, 1995. **28**(7): p. 845-56.
129. De Paulis, R., De Matteis, G.M., Nardi, P., Scaffa, R., Buratta, M.M., and Chiariello, L., *Opening and Closing Characteristics of the Aortic Valve after Valve-Sparing Procedures Using a New Aortic Root Conduit.* Annals of Thoracic Surgery, 2001. **72**(2): p. 487-494.
130. Aybek, T., Sotiriou, M., Wohleke, T., Miskovic, A., Simon, A., Doss, M., Dogan, S., Wimmer-Greinecker, G., and Moritz, A., *Valve Opening and Closing Dynamics after Different Aortic Valve-Sparing Operations.* Journal of Heart Valve Disease, 2005. **14**(1): p. 114-20.

131. Handke, M., Heinrichs, G., Beyersdorf, F., Olschewski, M., Bode, C., and Geibel, A., *In Vivo Analysis of Aortic Valve Dynamics by Transesophageal 3-Dimensional Echocardiography with High Temporal Resolution.* Journal of Thoracic and Cardiovascular Surgery, 2003. **125**(6): p. 1412-9.
132. Leyh, R.G., Schmidtke, C., Sievers, H.H., and Yacoub, M.H., *Opening and Closing Characteristics of the Aortic Valve after Different Types of Valve-Preserving Surgery.* Circulation, 1999. **100**(21): p. 2153-60.
133. Zou, Y. and Zhang, Y., *The Orthotropic Viscoelastic Behavior of Aortic Elastin.* Biomechanics and Modeling in Mechanobiology, 2011. **10**(5): p. 613-25.
134. Boerboom, R.A., Driessen, N.J., Bouten, C.V., Huyghe, J.M., and Baaijens, F.P., *Finite Element Model of Mechanically Induced Collagen Fiber Synthesis and Degradation in the Aortic Valve.* Annals of Biomedical Engineering, 2003. **31**(9): p. 1040-53.
135. Rabkin, S.W., *The Association of Hypertension and Aortic Valve Sclerosis.* Blood Pressure, 2005. **14**(5): p. 264-72.
136. Branch, K.O.B., Kd; Otto, Cm;, *Aortic Valve Sclerosis as a Marker of Active Atherosclerosis.* Current Cardiology Reports, 2002. **2**(4): p. 7.
137. Nemes, A., Forster, T., and Csanady, M., *Reduction of Coronary Flow Reserve in Patients with Increased Aortic Stiffness.* Canadian Journal of Physiology and Pharmacology, 2007. **85**(8): p. 818-22.
138. Oren, S., Isakov, I., Golzman, B., Kogan, J., Turkot, S., Peled, R., and Yosefy, C., *The Influence of Smoking Cessation on Hemodynamics and Arterial Compliance.* Angiology, 2006. **57**(5): p. 564-8.
139. Tanaka, H., Dinenno, F.A., Monahan, K.D., Clevenger, C.M., Desouza, C.A., and Seals, D.R., *Aging, Habitual Exercise, and Dynamic Arterial Compliance.* Circulation, 2000. **102**(11): p. 1270-5.
140. Nestel, P.J., Pomeroy, S.E., Sasahara, T., Yamashita, T., Liang, Y.L., Dart, A.M., Jennings, G.L., Abbey, M., and Cameron, J.D., *Arterial Compliance in Obese Subjects Is Improved with Dietary Plant N-3 Fatty Acid from Flaxseed Oil Despite Increased Ldl Oxidizability.* Arteriosclerosis, Thrombosis, and Vascular Biology, 1997. **17**(6): p. 1163-70.
141. Nemes, A., Forster, T., Varga, A., Vass, A., Borthaiser, A., Pálinkás, A., and Csanády, M., *How Can Coronary Flow Reserve Be Altered by Severe Aortic Stenosis?* Echocardiography, 2002. **19**(8): p. 655-659.
142. Baumgart, D., Haude, M., Liu, F., Ge, J., Goerge, G., and Erbel, R., *Current Concepts of Coronary Flow Reserve for Clinical Decision Making During Cardiac Catheterization.* American Heart Journal, 1998. **136**(1): p. 136-49.
143. Mohiaddin, R.H., Underwood, S.R., Bogren, H.G., Firmin, D.N., Klipstein, R.H., Rees, R.S., and Longmore, D.B., *Regional Aortic Compliance Studied by Magnetic Resonance Imaging: The Effects of Age, Training, and Coronary Artery Disease.* British Heart Journal, 1989. **62**(2): p. 90-6.
144. Leung, M.C., Meredith, I.T., and Cameron, J.D., *Aortic Stiffness Affects the Coronary Blood Flow Response to Percutaneous Coronary Intervention.* American Journal of Physiology, Heart and Circulatory Physiology, 2006. **290**(2): p. H624-30.
145. Saito, M., Okayama, H., Nishimura, K., Ogimoto, A., Ohtsuka, T., Inoue, K., Hiasa, G., Sumimoto, T., and Higaki, J., *Possible Link between Large Artery Stiffness and Coronary Flow Velocity Reserve.* Heart, 2008. **94**(6): p. e20.

146. Bogren, H.G., Mohiaddin, R.H., Klipstein, R.K., Firmin, D.N., Underwood, R.S., Rees, S.R., and Longmore, D.B., *The Function of the Aorta in Ischemic Heart Disease: A Magnetic Resonance and Angiographic Study of Aortic Compliance and Blood Flow Patterns.* American Heart Journal, 1989. **118**(2): p. 234-47.
147. Gunderman, R.B., *Essential Radiology: Clinical Presentation Pathophysiology Imaging,* 2006: Thieme Medical Publishers.
148. Mohiaddin, R.H., Firmin, D.N., and Longmore, D.B., *Age-Related Changes of Human Aortic Flow Wave Velocity Measured Noninvasively by Magnetic Resonance Imaging.* Journal of Applied Physiology, 1993. **74**(1): p. 492-7.
149. Belz, G.G., *Elastic Properties and Windkessel Function of the Human Aorta.* Cardiovascular Drugs and Therapy, 1995. **9**(1): p. 73-83.
150. Bader, H., *Importance of the Gerontology of Elastic Arteries in the Development of Essential Hypertension.* Clinical Physiology and Biochemistry, 1983. **1**(1): p. 36-56.
151. Wilcken, D.E., Charlier, A.A., Hoffman, J.I., and Guz, A., *Effects of Alterations in Aortic Impedance on the Performance of the Ventricles.* Circulation Research, 1964. **14**: p. 283-93.
152. Verhoeff, B.J., Siebes, M., Meuwissen, M., Atasever, B., Voskuil, M., De Winter, R.J., Koch, K.T., Tijssen, J.G., Spaan, J.A., and Piek, J.J., *Influence of Percutaneous Coronary Intervention on Coronary Microvascular Resistance Index.* Circulation, 2005. **111**(1): p. 76-82.
153. Rajappan, K., Rimoldi, O.E., Camici, P.G., Bellenger, N.G., Pennell, D.J., and Sheridan, D.J., *Functional Changes in Coronary Microcirculation after Valve Replacement in Patients with Aortic Stenosis.* Circulation, 2003. **107**(25): p. 3170-5.
154. Thubrikar, M., Carabello, B.A., Aouad, J., and Nolan, S.P., *Interpretation of Aortic Root Angiography in Dogs and in Humans.* Cardiovascular Research, 1982. **16**(1): p. 16-21.
155. Higashidate, M., Tamiya, K., Beppu, T., and Imai, Y., *Regulation of the Aortic-Valve Opening - in-Vivo Dynamic Measurement of Aortic-Valve Orifice Area.* Journal of Thoracic and Cardiovascular Surgery, 1995. **110**(2): p. 496-503.
156. Robicsek, F., Thubrikar, M.J., Cook, J.W., and Fowler, B., *The Congenitally Bicuspid Aortic Valve: How Does It Function? Why Does It Fail?* Annals of Thoracic Surgery, 2004. **77**(1): p. 177-184.
157. Brewer, R.J., Deck, J.D., Capati, B., and Nolan, S.P., *The Dynamic Aortic Root. Its Role in Aortic Valve Function.* Journal of Thoracic and Cardiovascular Surgery, 1976. **72**(3): p. 413-7.
158. Mowat, D.H.R., Haites, N.E., and Rawles, J.M., *Aortic Blood Velocity-Measurement in Healthy-Adults Using a Simple Ultrasound Technique.* Cardiovascular Research, 1983. **17**(2): p. 75-80.
159. Siebes, M., Verhoeff, B.J., Meuwissen, M., De Winter, R.J., Spaan, J.a.E., and Piek, J.J., *Single-Wire Pressure and Flow Velocity Measurement to Quantify Coronary Stenosis Hemodynamics and Effects of Percutaneous Interventions.* Circulation, 2004. **109**(6): p. 756-762.
160. Zhang, Z.D., Svendsen, M., Choy, J.S., Sinha, A.K., Huo, Y., Yoshida, K., Molloi, S., and Kassab, G.S., *New Method to Measure Coronary Velocity and Coronary Flow Reserve.* American Journal of Physiology-Heart and Circulatory Physiology, 2011. **301**(1): p. H21-H28.

161. Nemes, A., Forster, T., Lengyel, C., and Csanady, M., *Elastic Modulus Characterising the Aortic Distensibility and Coronary Flow Reserve in Diabetes Mellitus Patients with a Negative Coronary Angiogram.* European Heart Journal, 2005. **26**: p. 692-692.
162. Balazs, E., Pinter, K.S., Egyed, A., Csanady, M., Forster, T., and Nemes, A., *The Independent Long-Term Prognostic Value of Coronary Flow Velocity Reserve in Female Patients with Chest Pain and Negative Coronary Angiograms (Results from the Szeged Study).* International Journal of Cardiology, 2011. **146**(2): p. 259-61.
163. Nemes, A., Balazs, E., Pinter, S., Csanady, M., and Forster, T., *Long-Term Prognostic Significance of Coronary Flow Velocity Reserve in Patients with Significant Coronary Artery Disease Not Involving the Left Anterior Descending Coronary Artery (Results from the Szeged Study).* Echocardiography, 2010. **27**(3): p. 306-10.
164. Nemes, A., Forster, T., and Csanady, M., *Relationship between Coronary Flow Velocity Reserve and Aortic Stiffness.* American Journal of Physiology, Heart and Circulatory Physiology, 2006. **290**(3): p. H1311.
165. O'rourke, M.F., *How Stiffening of the Aorta and Elastic Arteries Leads to Compromised Coronary Flow.* Heart, 2008. **94**(6): p. 690-1.
166. Nemes, A., Forster, T., Thury, A., Kovacs, Z., Boda, K., and Csanady, M., *The Comparative Value of the Aortic Atherosclerosis and the Coronary Flow Velocity Reserve Evaluated by Stress Transesophageal Echocardiography in the Prediction of Patients with Aortic Stenosis with Coronary Artery Disease.* International Journal of Cardiovascular Imaging, 2003. **19**(5): p. 371-6.
167. Nemes, A., Forster, T., Ungi, I., Nagy, V., Vass, A., Palinkas, A., Varga, A., and Csanady, M., *The Coronary Flow Velocity Reserve Measured by Stress Transoesophageal Echocardiography Evaluates the Success of Coronary Interventions--Results of a 5-Year Follow-Up.* Scandinavian Cardiovascular Journal, 2005. **39**(5): p. 286-92.
168. Williams, G.S., Hubbell, C.W., Fenkell, G.H., and American Society of Civil, E., *Experiments at Detroit, Mich., on the Effect of Curvature Upon the Flow of Water in Pipes,* 1902, New York.
169. Berger, S.A., Talbot, L., and Yao, L.S., *Flow in Curved Pipes.* Annual Review of Fluid Mechanics, 1983. **15**(1): p. 461-512.
170. Cunningham, K.S. and Gotlieb, A.I., *The Role of Shear Stress in the Pathogenesis of Atherosclerosis (Vol 85, Pg 9, 2005).* Laboratory Investigation, 2005. **85**(7): p. 942-942.
171. Gibson, C.M., Diaz, L., Kandarpa, K., Sacks, F.M., Pasternak, R.C., Sandor, T., Feldman, C., and Stone, P.H., *Relation of Vessel Wall Shear-Stress to Atherosclerosis Progression in Human Coronary-Arteries.* Arteriosclerosis and Thrombosis, 1993. **13**(2): p. 310-315.
172. Halcox, J.P.J., Schenke, W.H., Zalos, G., Mincemoyer, R., Prasad, A., Waclawiw, M.A., Nour, K.R.A., and Quyyumi, A.A., *Prognostic Value of Coronary Vascular Endothelial Dysfunction.* Circulation, 2002. **106**(6): p. 653-658.
173. Bech, G.J.W., Droste, H., Pijls, N.H.J., De Bruyne, B., Bonnier, J.J.R.M., Michels, H.R., Peels, K.H., and Koolen, J.J., *Value of Fractional Flow Reserve in Making Decisions About Bypass Surgery for Equivocal Left Main Coronary Artery Disease.* Heart, 2001. **86**(5): p. 547-552.
174. Souli, M., *Course Notes from "LS-Dyna Advance Course in Ale and Fluid/Structure Coupling"*, 2004, Livermore Scientific Technology Corp.: Livermore, CA.

Appendix I: Implementing the pressure reservoir approach

The flow domain in all of the models is generally comprised of a control volume and individual in/outlets created as reservoirs. These reservoirs are made of ambient elements capable of supplying and removing fluid to and from the control volume. Therefore, it is analogous to assuming that the inlet reservoir delivers fluid at a prescribed velocity (normal to its surface), and that the aortic and coronary outlets receive fluid at a specified pressure. These boundary conditions are time dependant and vary during a cardiac cycle. LS-DYNA uses an equation of state to relate pressure to specific volume in fluid-like materials. A linear polynomial equation of state (linear in terms of internal energy) has been used to define such relation for blood in our model. The general form of this equation is given in Equation (1) below:

$$P = C_0 + C_1\mu + C_2\mu^2 + C_3\mu^3 + (C_4 + C_5 + C_6\mu^2)\,E \tag{1}$$

where, P is the pressure, C_n are material constants, E is the internal energy and μ is related to relative volume (V_r) as below:

$$\mu = {}^{1}/_{V_r} - 1 \tag{2}$$

$$V_r = {}^{\vartheta}/_{\vartheta_0} = {}^{\rho_0}/_{\rho} = {}^{1}/_{\eta} \tag{3}$$

$$\mu = \frac{\vartheta_0 - \vartheta}{\vartheta_0} = 1 - \eta \tag{4}$$

where, the subscript "o" represents the initial state, υ is the specific volume and ρ is the density of the material, and η is just another volumetric parameter. Therefore pressure curves can be defined by varying the relative volume and assuming the internal energy to be zero. Coefficients C_2 and C_3 should be set to zero for fluid like materials [174]. Therefore Equation (1) can be re-written as:

$$P = C_0 + C_1\,\mu \tag{5}$$

where, C_0 represents the initial pressure and C_1 is referred to as the bulk modulus (K) and is defined as:

$$C_1 = K = -V \frac{\Delta P}{\Delta V} = \rho_0 c^2 \quad (6)$$

where, ρ_0 is the initial density and c is the speed of sound through the fluid elements. Assuming the initial pressure to be zero the pressure and the relative volume of the fluid can be related through the following equation:

$$P = \frac{\rho c^2 (1 - V)}{V} \quad (7)$$

Considering Equation (5), the only variable required by LS-DYNA to relate relative volume and pressure is C_1. As suggested by Equation (6) this constant is dependant on the speed of sound through the material. It has been shown that a speed of sound equal to 1500 cm/s produces accurate results in terms of shear and pressure for a fluid traveling at a maximum velocity of 150 cm/s [52]. Considering the fact that bloods peak velocity in the aortic valve is similar to the reported values, the value for speed of sound in our simulations was chosen to be 1500 cm/s which leads to C_1 = 238500 Pa (assuming a viscosity of 1060kg.m^{-3}).